2015

FINDING MARS PALEOPOLES FROM MAGNETIZATION EDGE EFFECTS TO DETERMINE THE HISTORY OF MARS' CORE DYNAMO

Melissa Lynn Ditty
University of Kentucky, mditty25@gmail.com

STUDENT AGREEMENT:

I represent that my thesis or dissertation and abstract are my original work. Proper attribution has been given to all outside sources. I understand that I am solely responsible for obtaining any needed copyright permissions. I have obtained needed written permission statement(s) from the owner(s) of each third-party copyrighted matter to be included in my work, allowing electronic distribution (if such use is not permitted by the fair use doctrine) which will be submitted to UKnowledge as Additional File.

I hereby grant to The University of Kentucky and its agents the irrevocable, non-exclusive, and royalty-free license to archive and make accessible my work in whole or in part in all forms of media, now or hereafter known. I agree that the document mentioned above may be made available immediately for worldwide access unless an embargo applies.

I retain all other ownership rights to the copyright of my work. I also retain the right to use in future works (such as articles or books) all or part of my work. I understand that I am free to register the copyright to my work.

REVIEW, APPROVAL AND ACCEPTANCE

The document mentioned above has been reviewed and accepted by the student's advisor, on behalf of the advisory committee, and by the Director of Graduate Studies (DGS), on behalf of the program; we verify that this is the final, approved version of the student's thesis including all changes required by the advisory committee. The undersigned agree to abide by the statements above.

Melissa Lynn Ditty, Student

Dr. Dhananjay Ravat, Major Professor

Dr. Edward W. Woolery, Director of Graduate Studies

FINDING MARS PALEOPOLES FROM MAGNETIZATION EDGE EFFECTS TO DETERMINE THE HISTORY OF MARS' CORE DYNAMO

THESIS

A Thesis
submitted in partial fulfillment of the requirements for
the degree of Master of Science in Earth and Environmental Science
in the College of Arts and Sciences
at the University of Kentucky

By

Melissa Lynn Ditty

Lexington, KY

Director: Dr. Dhananjay Ravat, Professor of Geophysics

Lexington, KY

2015

ABSTRACT OF THESIS

FINDING MARS PALEOPOLES FROM MAGNETIZATION EDGE EFFECTS TO DETERMINE THE HISTORY OF MARS' CORE DYNAMO

This is a new method of determining magnetization strength, direction, and paleopole location from magnetic anomalies across edges of the equatorial band of magnetic sources on Mars. Different assumed locations of paleopoles result in different inducing field directions in the vicinity of an edge. Thus, with different paleopoles, the resulting magnetic fields from the edges of magnetic sources are different, and correlate differently with the observed fields. Best correlating observed and computed magnetic edge effect fields yield the potential paleopoles. The total gradient (TG) of the z-component magnetic field was used to identify the edges of magnetization boundaries. Three edge segments yielded meaningful paleopoles. They are: (15°S, 285°E)/(0°, 292.5°E) across the northeast trending edge east of Tharsis; (15°N, 195°E) across the southern boundary located in the Terra Cimmeria and Terra Sirenum area; and (15°S, 165°E)/(45°S, 180°E) across the northeast edge of Hellas Planitia. The effective magnetization in these regions (assuming 40km magnetic layer thickness) is 7.02, 42.13-94.79, and 2.63-3.51 A/m, respectively. Evidence from the overlap of regions of TG and chronostratigraphy suggests that the dynamo was active during the Noachian and may have been active in the early Hesperian.

KEYWORDS: Mars Paleopoles, Magnetic Sources, Magnetization Strength, Edge Effects, Dynamo

Melissa Lynn Ditty

July 21, 2015

FINDING MARS PALEOPOLES FROM MAGNETIZATION EDGE EFFECTS TO DETERMINE THE HISTORY OF MARS' CORE DYNAMO

By

Melissa Lynn Ditty

Dhananjay Ravat

Director of Thesis

Edward W. Woolery

Director of Graduate Students

July 21, 2015

Date

TABLE OF CONTENTS

List of Tables ……..iv

List of Figures ……v

Chapter One: Introduction ……...1

Chapter Two: Background
Formation and Evolution of the Dynamo ……9
Timing of the Dynamo Shutdown ……11

Chapter Three: Methodology: TG Field to Source Regions and Association with Chronostratigraphic Ages
Total Gradient ……16
Chronostratigraphic Ages and Geologic Boundaries ……20
Comparison of the Total Gradient Fields with the Age Units ……...23

Chapter Four: Methodology: Paleopoles and Magnetization
Magnetic Edge Effects and Determination of Paleopoles ……52
Effective Magnetization ……56

Chapter Five: Discussion ……..83

Chapter Six: Conclusion and Future Research ……105

Appendices
Appendix 1: ArcGIS Calculations ……...109
Appendix 2: Boundaries Tested ……..118

References……119

Vita ……..126

LIST OF TABLES

Table 2.1, List of Paleopoles by Researcher ……..14
Table 3.1, Overlap of Chronostratigraphic Units with TG by Cutoffs ……..29
Table 4.1, Summary Results for Edge Segments ……...62
Table 4.2, Summary Results of Effective Magnetization ……..63
Table 5.1, Supplemental Magnetization and Pole Locations by Author……93
Table 5.2, Window 1 Magnetization and Pole Comparison to Other Studies……94
Table 5.3, Window 2 Magnetization and Pole Comparison to Other Studies……95
Table 5.4, Window 9 Magnetization and Pole Comparison to Other Studies……96
Table 5.5, Window 11 Magnetization and Pole Comparison to Other Studies……..97
Table 5.6, Window 13 Magnetization and Pole Comparison to Other Studies……..98
Table A1.1, Overlap of Chronostratigraphic Units with TG cutoffs of 10, 15, 25, 50, 100, and 200 nT/km Excluding the Units Api and Apl ……...111
Table A1.2, Overlap of TG Cutoffs with Chronostratigraphic Units as a Percentage of Total Planet Surface Area ……..114

LIST OF FIGURES

Figure 1.1, Mars Topography ……7
Figure 1.2, Mars Radial Magnetic Field ……..8
Figure 2.1, Paleopoles from Other Researchers ……..15
Figure 3.1a, Z-Component Field Profiles for Different Inclinations ……32
Figure 3.1b, TG Field Profiles for Different Inclinations ……..32
Figure 3.2a, Z-Component Field Profiles for Different Depths……32
Figure 3.2b, TG Field Profiles for Different Depths ……32
Figure 3.3, Total Gradient Field at 10 km……33
Figure 3.4, Geologic Map of Mars……34
Figure 3.5, Epoch Divisions for Mars……36
Figure 3.6, Chronostratigraphic Map of Mars ……37
Figure 3.7, Amazonian Polar Regions on Map of Total Gradient ……38
Figure 3.8, Percent Area by TG Cutoff ……39
Figure 3.9, Number of Cells of Overlap by TG cutoff ……39
Figure 3.10 A, TG Contour for 5 nT/km on Chronostratigraphic Map of Mars……40
Figure 3.10 B, TG Contour for 15 nT/km on Chronostratigraphic Map of Mars ……40
Figure 3.10 C, TG Contour for 25 nT/km on Chronostratigraphic Map of Mars……..41
Figure 3.11, Hesperian/Noachian Source with Weak Fields in Amazonian Terrain……..42
Figure 3.12, High Amplitude Olympus Mons Anomaly with Amazonian Surface Age…43
Figure 3.13, Profile High Amplitude Olympus Mons Anomaly on
2006 Map of Geology ……44
Figure 3.14, Profile High Amplitude Olympus Mons Anomaly on
2014 Map of Geology ……45
Figure 3.15, High Amplitude Tharsis Montes Anomaly with Amazonian Surface Age…46
Figure 3.16, Profile High Amplitude Tharsis Montes Anomaly on
2006 Map of Geology ……...47
Figure 3.17, Profile High Amplitude Tharsis Montes Anomaly on
2014 Map of Geology ……48
Figure 3.18, High Amplitude Anomaly with Noachian Surface Age ……49
Figure 3.19, Profile High Amplitude Anomaly with Noachian Surface Age on
2006 Map of Geology ……50
Figure 3.20, Profile High Amplitude Anomaly with Noachian Surface Age on
2014 Map of Geology ……51
Figure 4.1, Map of TG at 10 km with Boundaries and Windows……..64
Figure 4.2, Magnetization and Resultant Field at 150km for a
Test Magnetic North at 60°N, 210°E ……65
Figure 4.3, Magnetization and Resultant Field at 150km for a
Test Magnetic North at 90°N, 0°E ……66
Figure 4.4, Magnetic Fields and Profiles across Segment/Window 13 ……67
Figure 4.5, Profiles from Segment/Window 13 on 2006 Map of Chronostratigraphy ….68
Figure 4.6, Profiles from Segment/Window 13 on 2014 Map of Geology 69
Figure 4.7, Magnetic Fields and Profiles across Segment/Window 1 ……...70
Figure 4.8, Profiles from Segment/Window 1 on 2006 Map of Chronostratigraphy ……71
Figure 4.9, Profiles from Segment/Window 1 on 2014 Map of Geology……..72

Figure 4.10, Magnetic Fields and Profiles across Segment/Window 2 ……73
Figure 4.11, Profiles from Segment/Window 2 on 2006 Map of Chronostratigraphy …..74
Figure 4.12, Profiles from Segment/Window 2 on 2014 Map of Geology……75
Figure 4.13, Magnetic Fields and Profiles across Segment/Window 9 ……76
Figure 4.14, Profiles from Segment/Window 9 on 2006 Map of Chronostratigraphy …..77
Figure 4.15, Profiles from Segment/Window 9 on 2014 Map of Geology……78
Figure 4.16, Magnetic Fields and Profiles across Segment/Window 11 ……...79
Figure 4.17, Profiles from Segment/Window 11 on 2006 Map of Chronostratigraphy …80
Figure 4.18, Profiles from Segment/Window 11 on 2014 Map of Geology……..81
Figure 4.19 A, Map of High Quality Poles on Chronostratigraphy ……...82
Figure 4.19 B, Map of High Quality Poles on Z-Component……82
Figure 5.1, Dichotomy Boundary (Milbury and Schubert, 2010)……100
Figure 5.2, Map of Chronostratigraphic Units with Windows and Boundaries ……..101
Figure 5.3, Comparison of 2014 Map of Mars with 2006 Map of Mars ……102
Figure 5.4, Best-fit Paleopoles from Magnetic Anomalies near Syrtis Major
(Milbury et al., 2012) ……...103
Figure 5.5, Best-fit Paleopoles from Magnetic Anomalies near Tyrrhenus Mons
(Milbury et al., 2012) ……...103
Figure 5.6, Map of Magnetic Anomalies on Geology
(Milbury et al., 2012) ……...104
Figure A1.1, Output Number of Cells for Overlap Calculations ……116
Figure A1.2, Polygon Area Calculations……..116
Figure A1.3, Error Associated with Calculating Area by Cells ……...117
Figure A2.1, Additional Test Boundaries show on TG Map……118

Chapter 1. Introduction

Mariner 4 provided the first magnetic data in a fly-by mission of Mars in July 1965; its magnetometer recorded a magnetic field equivalent to 0.03% (<50 nT) of the strength of the Earth's core field dipole (Acuña et al., 2001). Because the strength of the dipole was so weak, none of the later orbital missions carried magnetometers for measuring the internal magnetic field of the planet. Mars Global Surveyor (MGS), with magnetometers intended primarily for ionospheric and magnetospheric studies, was the first spacecraft to observe magnetic field below Mars' ionosphere. The goals of the magnetic field investigation conducted by MGS were to establish the nature of Mars magnetic field and map any remanent field (Acuña et al., 2001). The magnetic data collected by MGS are classified according to the different phases of data acquisition: the aero-braking (AB), science-phasing orbits (SPO), and mapping orbits (MO). The AB and SPO data were collected through 1284 elliptical orbits with periapses between 85 to 170 km altitude (Esposito et al., 1997; Acuña et al., 2001). Final mapping orbit (MO) had an average mapping altitude of 400 km and data were collected for over 6,000 orbits (Acuña et al., 2001). MGS confirmed the lack of an ambient, internally generated, main magnetic field, but demonstrated the existence of large amplitude remanent magnetic anomalies in the southern highlands (Acuña et al., 1999, 2001). The lack of a current internally generated main field, combined with the evidence for localized large amplitude magnetic anomalies, indicates that Mars must have had an internal active dynamo in the past (Acuña et al., 1999). The magnetization must have been acquired during a time when the dynamo was active.

The distribution of Martian crustal magnetic anomalies reveals several interesting

characteristics. The strongest anomalies occur in the oldest chronostratigraphic unit (Noachian) which implies the dynamo must have been active at least during some periods of the Noachian (Hood et al., 2003). The magnitude of magnetic anomalies on Mars is also much larger than those on Earth. The intensity of crustal magnetization in many regions of Mars is roughly 10 times greater than on Earth (Connerney et al., 1999). The largest magnitude anomalies on Mars are over 20 times larger than those on Earth and are oriented east-west in the southern hemisphere between 10º to 90º S and 120º to 240º E (Connerney et al., 1999). Of note are the linear alternating positive and negative anomalies in Terra Cimmeria and Terra Sirenum. Many possible tectonic explanations for the formation of the strong east-west trending anomalies have been proposed. These include: seafloor spreading (Connerney et al., 1999, 2001); non-seafloor spreading intrusive bodies (Nimmo, 2000; Arkani-Hamed, 2001a; Hood and Richmond, 2002; Ravat, 2011); and juxtaposition of continental blocks with different magnetization like those found in continental suture zones on Earth (Fairen et al., 2002; Miller et al., 2001). Seafloor spreading is generally associated with shallow thin magnetic sources leading to little signature at satellite altitudes (Arkani-Hamed, 2005; Ravat, 2003; Ravat, 2011) and it is unclear if large and thick intrusive bodies could produce such strong, extensive, linearly continuous magnetic anomalies because they may acquire thermal remanent magnetization over differently polarized periods of the core magnetic field and thus, their effective magnetization would be reduced (Arkani-Hamed, 2005). Some authors have questioned interpretations of long, linear magnetic anomalies because at satellite attitude these features could reflect some degree of coalescence of small adjacent anomaly features (Ravat, 2003). Biswas (2005) noted, due to coalescence, it would also be

difficult to determine magnetization direction of sources from anomalies at high altitudes if they were formed from multiple differently magnetized sources (i.e., multiple sources with different directions of magnetizations). In addition to magnetization and tectonic differences, any comparison between Martian anomalies and those on Earth must be considered with respect to resolution based on the different altitudes of observation because magnetic fields attenuate with increased distance from the source (e.g., Blakely, 1995; Langel and Hinze, 1998).

The observed magnetic field of Mars is also certainly a reflection of numerous impact craters. Figure 1.1 shows the topography of Mars with a scale by kilometers above and below the reference areoid (geoid). Some of largest and most well defined impact craters include Argyre (A), Hellas (H), Isidis (I) and Utopia (U). Figure 1.2 shows the altitude normalized global radial magnetic field (Br) calculated at 200 km as mapped by Purucker et al. (2000). Major craters such as Hellas and Argyre show few magnetic features. The features that are present may be an artifact of modeling because the data from which they were modeled do not have these features. The lack of magnetic features is striking in the case of Isidis as it forms a semi-circular region devoid of anomalies. It has been proposed that shock demagnetization, in the absence of a core field, could explain the reduction in magnetism within these large impact craters (Acuña et al., 1999; Mohit and Arkani-Hamed, 2004).

Since the discovery of magnetic fields from remanently magnetized crust on Mars, there has been little consensus on the duration of the magnetic field dynamo (Acuña et al., 1999; Schubert et al., 2000). The absence of crustal magnetic field features under the sites of giant impact basins led early investigators to conclude that the dynamo

vanished prior to the impacts in early Noachian (Acuña et al., 1999; Frey, 2006; Arkani-Hamed, 2001a). Schubert et al. (2000), however, suggested that the dynamo could have started after the first of the giant impacts (e.g., impacts creating the northern lowlands) and continued into the Hesperian. Absence of magnetic features in impact craters combined with adjacent remanently magnetized features across different age regions can help constrain the timing of Martian dynamo activity. Recent modeling has suggested that giant impacts can cause sufficient heating and conditions suitable for stopping and then restarting the core dynamo (Arkani-Hamed and Olson, 2010; Arkani-Hamed and Ghods, 2011; Arkani-Hamed, 2012).

A number of researchers have determined the magnetization direction of isolated magnetic anomalies from different locations on the planet. Paleopoles derived from these anomalies show some clustering of poles and evidence for polar reversals (Arkani-Hamed, 2001b). However, the scatter in the determined paleopoles covers almost a fourth of the planet, so if these poles are meaningful then they imply a number of paleopole clusters. Because the geomagnetic poles tend to lie close to the geographic poles (due to the influence of planetary rotation on the core dynamo), different paleopole clusters could be interpreted as true polar wander (TPW) where the planet has undergone episodes of tilting, i.e., either shifts in entire planet's orientation or differential shifts of the core and the crust-mantle.

Interpretation of the geometry of magnetic sources from anomalies depends partly on the orientation of their magnetization direction (Blakely, 1995; Langel and Hinze, 1998). The magnetization direction of crustal sources is generally not known *a priori*. The total gradient of the magnetic anomaly field, however, is analytic for two-

dimensional magnetic sources, i.e., invariant to magnetization direction, and nearly so for three-dimensional ones (Nabighian, 1972, 1974, 1984; Roest et al., 1992; Ravat, 2011). One of the purposes of this study is to use total gradient (TG) of the z-component (negative of radial component shown in Figure 1.2 and more customary in Earth-based geologic analysis than the radial component) magnetic anomaly field to constrain better which periods on Mars (Noachian, Hesperian or Amazonian) show magnetized regions. Since TG is magnetization direction invariant, the interpretation of TG allows for fewer assumptions than other methods. One of the other enhancements used in this study is that TG fields computed from a recent high resolution magnetic field model are utilized (Langlais et al., 2010). The TG fields computed from this model are stable at low altitude (e.g., 10 km). Because the magnetic field attenuates and spreads out away from the source, a stable field at low altitude affords a higher resolution comparison between the mapped chronostratigraphic units (Noachian, Hesperian and Amazonian) and the TG features.

Figure 1.2 shows a contrast between magnetized and non-magnetized regions on Mars. This contrast creates natural magnetization boundaries in some cases especially on the edges of the latitudinal band of anomalies and some of these edges are also two-dimensional. Because these two-dimensional features are magnetization direction invariant in the TG field perpendicular to the anomaly features, it is possible to deduce edges of the sources. Milbury and Schubert (2010) assumed that Mars' crustal dichotomy boundary is a magnetization boundary. They used the best fit of the low spherical harmonic degree field computed from the boundary with the corresponding global observed fields to determine an average paleopole. In this study, edge effects were used

differently in that they were examined to ascertain: 1) whether the anomaly features created from different segments of major magnetization boundaries on Mars could lead to the determination of the orientations of the core field that magnetized them and 2) whether forward modeling of the magnetization contrast could aid in determining the amplitude and direction of magnetization of regions adjacent to the magnetization boundaries.

To constrain the timing of the dynamo, Milbury and Schubert (2010) also examined the correspondence of magnetic field with chronostratigraphic age units (Scott and Tanaka, 1986). Their logic was that if a particular age region had a magnetic field on it, then the core field dynamo could be considered extant at that time. Milbury and Schubert qualify these assumptions (discussed in a later chapter). However, the skewness of magnetization direction can spread magnetic anomaly fields over much larger areas than the magnetized region producing them. Since the TG fields at low altitude have less skewness and, as a result of being gradient fields, are more concentrated above their sources, it is worthwhile examining the timing of the dynamo utilizing TG. Also, since the geologic/chronostratigraphic mapping of Scott and Tanaka in 1986, Skinner et al. (2006) have converted their maps into a GIS database and this affords a digital comparison between the chronostratigraphic units and the TG fields at higher resolution. In this study, dynamo timing results of Milbury and Schubert (2010) done with radial fields were compared to results determined using TG fields. In addition, any systematic progression of age versus paleopole location (i.e., the TPW path) was examined using the chronostratigraphic age of the magnetized regions.

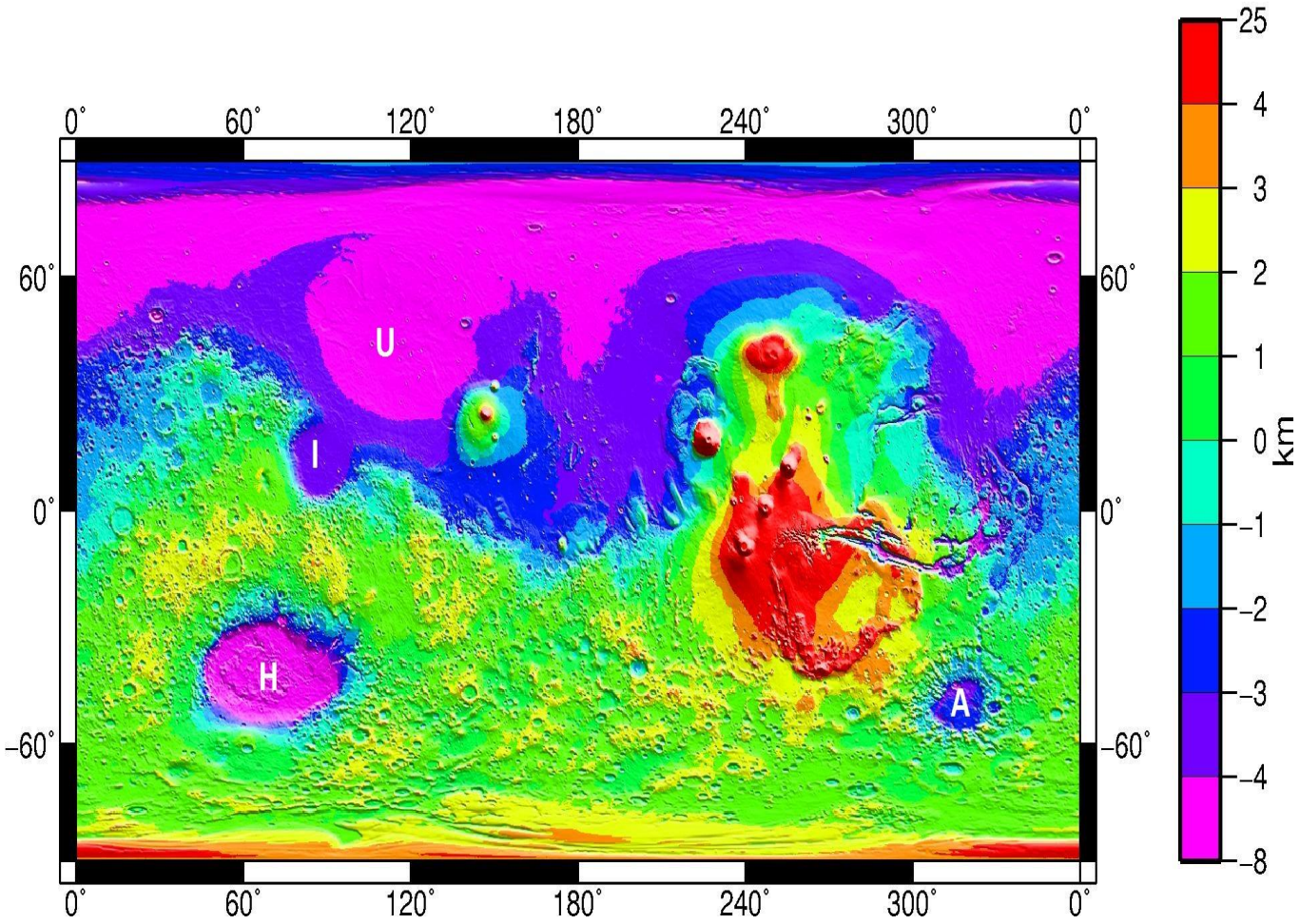

Figure 1.1. Mars topography (equidistant cylindrical projection). Letters denote major impact craters: U-Utopia, I - Isidis, H - Hellas, and A - Argyre.

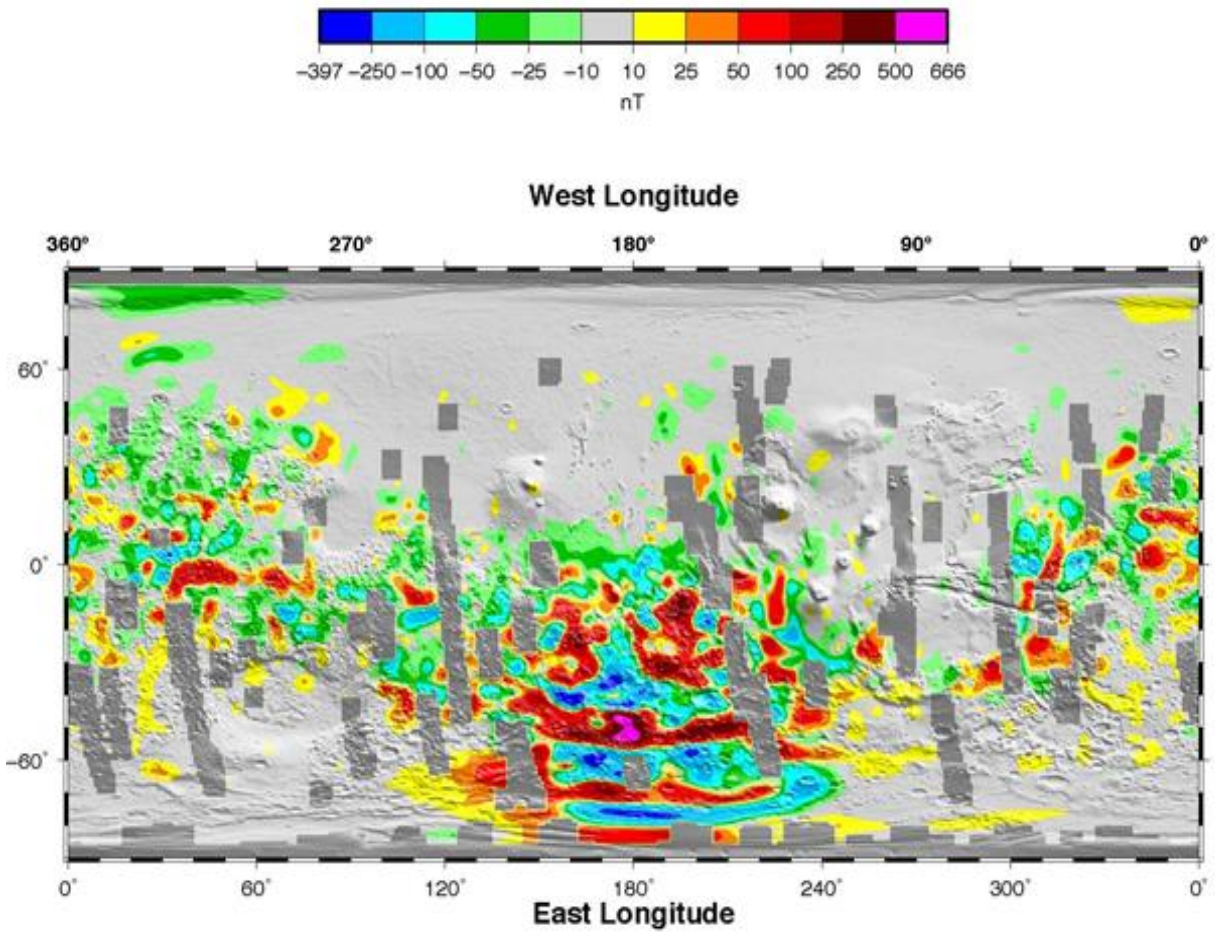

Figure 1.2. Mars radial magnetic field. Altitude normalized radial magnetic field computed at 200km from aerobraking and science phasing orbit low altitude data superimposed on a topography gradient intensity map. N-S dark gray bands are areas removed due to inadequate low altitude data coverage. Plot is taken from Purucker et al. (2000).

Chapter 2. Background

Formation and Evolution of the Dynamo

Accretionary processes dominate planet formation (Wetherill, 1994). Boss (1990) developed the first comprehensive thermal model of planet formation and determined Mars formed hot, differentiated, and cooled with time. Sources of heat for planets are kinetic energy converted to heat during accretion, radioactive elements that generate heat during decay and kinetic energy from isolated large impacts (Arkani-Hamed and Olson, 2010; Arkani-Hamed and Ghods, 2011; Arkani-Hamed, 2012).

Complete melting of a planetary body like Mars would require $2x10^{30}$ J of energy (Barlow, 2008). Wetherill (1990) showed that accretionary processes in terrestrial planet formation could produce in excess of 4×10^{30} J of energy and Elkins-Tanton et al. (2005) showed that the radioactive decay of ^{26}Al alone could contribute 2×10^{30} J of energy (Barlow, 2008). These two sources of heat alone are sufficient to cause total melting of Mars (Elkins-Tanton et al.; 2005; Barlow, 2008). A molten planet differentiates by elemental density and chemical affinity (Barlow, 2008). Denser metallic phases sink to the center to form the core while less dense materials such as oxidized silicates rise to the surface. Highly siderophile elements and chalcophile elements that have affinities for Fe and S (Mo, W, Co, Ni) follow iron to the core while lithophile elements (Li, Be, B, Na) follow oxygen compounds to the surface. Highly oxidizing conditions and high FeO content in the mantle allow some lithophilic behavior of siderophile elements on Mars (Barlow, 2008).

Information about the early evolution of Mars comes mainly from geochemistry of meteorites and geochemical, geomorphological and geophysical analysis of data from

landers and satellites. The most useful meteorites from Mars are the shergottites, nahklites and chassignites (SNC) because they did not form directly from the solar nebula and have distinct mineralogical compositions (Barlow, 2008). The isotopic composition of trapped gases (Ar, Xe) in these meteorites indicates that they are from Mars (Bogard and Johnson, 1983; Barlow, 2008). Analysis of basaltic shergottites provides insight into mantle conditions because of their volcanic texture. Kleine et al. (2002) use Pb and $^{182}Hf/^{182}W$ isotope data from SNC meteorites to suggest that the core of Mars formed very rapidly. The idea that Mars accreted and differentiated rapidly is also supported by the correlative relationships between ^{87}Rb-^{87}Sr, ^{129}I-^{129}Xe, ^{146}Sm-^{142}Nd, ^{182}Hf-^{182}W, ^{187}Re-^{187}Os, ^{235}U-^{207}Pb and ^{238}U-^{206}Pb (Halliday et al., 2001; Barlow, 2008). Meteorite analysis also indicates that Mars' mantle is nearly two times as rich in Fe as Earth's mantle due to highly oxidizing conditions, but smaller than that of Earth's (20% of the mass) (Halliday et al., 2001; Barlow, 2008).

The crust of Mars has significant magnetization – significantly more than could be attributable to the weakly magnetic iron oxides in the soils on the surface which gives Mars its reddish tinge (Hviid et al., 1997). In order for such high remanent magnetization to exist, Mars had to have a core dynamo caused by a highly conducting convecting fluid rich iron core or outer core shell (Acuña et al., 1999; Connerney et al., 2004). Generally, for a rotating planet, the long term average dynamo poles are nearly coincident with the rotation axis (Merrill and McElhinny, 1983). The existence of a core dynamo requires certain thermal or compositional conditions. Glatzmeier and Roberts (1997) have shown that both thermal and compositional convection can drive dynamo action. Temperature gradient between the mantle and the core is the likely mechanism to form and sustain the

dynamo. The mechanisms proposed to have caused the dynamo to cease are changes in mantle convection (Nimmo and Stevenson, 2000), solidification of the core (Stevenson, 2000) and reduction in core heat production (Williams and Nimmo, 2004). Heat and shockwaves from large impacts also could contribute to stopping and restarting of dynamos (Arkani-Hamed and Ghods, 2011).

Timing of Dynamo Shutdown

Since the discovery of remanently magnetized crust on Mars (Acuña et al., 1999), there has been controversy regarding the timing of the magnetic field dynamo (Acuña et al., 1999; Schubert et al., 2000). Regions surrounding the large impact basins do not show remanent magnetization suggesting they have undergone shock demagnetization (Hood et al., 2003; Mohit and Arkani-Hamed, 2004). This led some investigators to conclude that the dynamo terminated before the impacts in the early Noachian (Acuña et al., 1999; Frey, 2006; Arkani-Hamed, 2001a). Schubert et al. (2000), on the other hand, argued that the dynamo initiated after the large impacts in the early Noachian and thus there is magnetized middle and late Noachian age crust as well as some magnetized Hesperian crust.

For terrestrial differentiated rotating planets, dynamos are driven primarily by gravitational potential energy release due to cooling of the planet (Spohn et al., 2014). Trapped heat (heat of formation) is released over time creating thermal stratification which sets up convection cells that transport hotter less dense material outward (Spohn et al., 2014). Other known dynamo driving forces include radiogenic heat and compositional convection. New thoughts and modeling suggest that successive giant

impacts can cause sufficient heating that can propagate to the core of Mars for stopping or temporarily disrupting and re-initiating a core dynamo (Arkani-Hamed and Olson, 2010; Arkani-Hamed and Ghods, 2011; Arkani-Hamed, 2012).

Evidence on the timing of dynamo can be gathered from examining the chronostratigraphic correlations with magnetized and non-magnetized features (Milbury and Schubert, 2010; Milbury et al., 2012). Because of the uncertainty in the magnetization direction and the coalescence of magnetic fields in high altitude observations (Ravat, 2011), the timing of the dynamo can presently only be inferred with limited resolution. It is also widely held that the impact-frequency based chronostratigraphy from surface rocks may not be representative of the age of magnetized units at depth. However, Milbury and Schubert (2010) and Milbury et al. (2012) mapped large magnetized regions of Hesperian and Amazonian ages. Thus, based on their analysis at least, ages of some of the regions of acquisition of magnetization could be related to Hesperian and perhaps Amazonian age terrains.

Using the region of Terra Cimmeria and Terra Sirenum, Sprenke and Baker (2000) found paleopoles clustered near 15°S, 45°E for the south magnetic pole. Paleopoles on Mars imply tilting of the rotational axis of Mars (called True Polar Wander) due to either impacts or internal mass heterogeneities, and the paleopole locations do not necessarily imply mechanisms of plate motion as observed on Earth (called Apparent Polar Wander). Sprenke (2005) showed that most north magnetic poles are located around 17°N, 230°E. Arkani-Hamed (2001b) analyzed 10 isolated, small anomalies and interpreted a magnetic paleopole close to 25°N 230°E (for a comprehensive list of paleopoles see Table 2.1 taken from Milbury et al., 2012 and accompanying Figure 2.1).

Milbury and Schubert (2010) determined paleopoles using the analysis of low spherical harmonic degree magnetic fields from the entire dichotomy boundary on Mars. They used the radial component of magnetic field to correlate magnetized regions of the planet with chronostratigraphic units from Scott and Tanaka (1986) to show that most Noachian, many Hesperian, and a few Amazonian surface age regions are underlain by magnetic features. Using statistical analysis of areas of different age units and locations of anomalies, they argued that the dynamo may have started after the giant impacts of Hellas, Argyre, and the impact basins of Northern Lowlands and remained active until the late Hesperian (Milbury and Schubert, 2010). Milbury et al. (2012) modeled magnetic anomalies that were associated with gravity anomalies in the vicinity of Tyrrhenus Mons and Syrtis Major volcanoes and found sources below Noachian surfaces produced equatorial paleopoles while sources below Hesperian surfaces tended to produce polar paleopoles. Milbury and Schubert assert based on this evidence that the dynamo initiated in the Noachian and continued into the Hesperian. The paleopoles Milbury and Schubert found are located at mid-to-high latitudes and are similar to the paleopoles determined by modeling of isolated magnetic features by Arkani-Hamed (2001b). These different groupings of paleopoles could be interpreted in terms of the true polar wander.

Table 2.1. List of paleopoles by researcher (Milbury et al., 2012).

	Paper	Anomaly Designation	Source Location (°E/°N)	Dipole/Magnetization Parameter	Paleopole Location (°E/°N)	Polarity	Source Geometry	Data
1	*Frawley and Taylor* [2004]	9	0.9/1.4	1.32×10^{16} A m^2	115.1/−81.6	N	dipole/prism	high alt
2	*Arkani-Hamed* [2001]	M1	20/−4	9.69 A/m	18/−20	N	prism	high alt
3	*Hood and Zakharian* [2001]	SA	27/65	2.40×10^{16} A m^2	224/61	S	disk	<200 km
	Arkani-Hamed [2001]	M3	27/65	4.67 A/m	220/36	N	prism	sph 50, 380 km alt
	Richmond and Hood [2003]	B	27/65	9.20×10^4 A	219/38	S	disk	low/high alt
	Hood et al. [2005]	A1	27/65	9.00×10^{15} A m^2	219/38	S	plate	high alt
4	*Arkani-Hamed* [2001]	M2	31/15	8.72 A/m	45/−1	N	prism	sph 50, 380 km alt
5	*Hood and Zakharian* [2001]	NA	32/83	1.20×10^{16} A m^2	219/38	S	disk	<200 km
	Richmond and Hood [2003]	A	32/83	4.20×10^4	224/61	S	disk	low/high alt
6	*Hood et al.* [2005]	A5a	35.1/−3.2	2.70×10^{16} A m^2			plate	high alt
	Hood et al. [2005]	A5b	39.2/−1.6	1.40×10^{16} A m^2	338/36	N	plate	high alt
	Hood et al. [2005]	A5c	45.7/−2.3	2.30×10^{16} A m^2			plate	high alt
7	*Arkani-Hamed* [2001]	M4	66/−5	12.78 A/m	255/23	N	prism	sph 50, 380 km alt
	Arkani-Hamed [2004b]	1	66/−6	13.23 A/m	241/16	N	prism	low/high alt
	Boutin and Arkani-Hamed [2006]	1	66/−6	N/R	198/70	S	prism	high alt (1)
	Boutin and Arkani-Hamed [2006]			N/R	200/70	S	prism	high alt (2)
8	*Arkani-Hamed* [2001]	M5	69/−15	10.95 A/m	72/−12	N	prism	sph 50, 380 km alt
	Arkani-Hamed [2004b]	2	70/−16	26.37 A/m	76/7	N	prism	low/high alt
	Boutin and Arkani-Hamed [2006]	2	70/−16	N/R	193/63	N	prism	high alt (1)
	Boutin and Arkani-Hamed [2006]			N/R	153/64	N	prism	high alt (2)
9	*Arkani-Hamed* [2001]	M6	103/−27	9.91 A/m	78/−7	N	prism	sph 50, 380 km alt
	Arkani-Hamed [2004b]	3	105/−28	14.91 A/m	60/20	N	prism	low/high alt
	Boutin and Arkani-Hamed [2006]	3	105/−28	N/R	204/14	N	prism	high alt (1)
	Boutin and Arkani-Hamed [2006]			N/R	214/22	N	prism	high alt (2)
10	*Richmond and Hood* [2003]	D_b	156/−18	5.80×10^5 A	230/31	S	disk	low/high alt
	Hood et al. [2005]	A6a	161/−26	2.30×10^{16} A m^2			plate	high alt
	Hood et al. [2005]	A6b	155.4/−15.8	1.50×10^{16} A m^2	257/34	S	plate	high alt
	Hood et al. [2005]	A6c	158.8/−23.3	1.60×10^{16} A m^2			plate	high alt
11	*Richmond and Hood* [2003]	D_a	165/−27	2.00×10^5 A	76/42	S	disk	low/high alt
12	*Langlais and Purucker* [2007]	single dipole	174.5/−8.75	N/R	59/−65	N	dipole	low/high alt
	Langlais and Purucker [2007]	multiple dipoles	174.5/−8.75	0.1–10.1 A/m	99/−88	N	dipole	low/high alt
	Hood et al. [2010]	single disk	173.5/−9	1.40×10^{16} A m^2	219/67	N	disk	high alt
	Hood et al. [2010]	dual disk	174.4/−8.7	1.00×10^{16} A m^2	228/66	N	disk	high alt
	Hood et al. [2010]	dual disk	173.6/−9.1	3.20×10^{15} A m^2			disk	high alt
13	*Quesnel et al.* [2007]	AB-A	191/−32	2.70×10^{16} A m^2	309.6/25.7	N	dipole/prism	low/high alt
	Hood et al. [2007]	A9	190.4/−33.8	3.10×10^{16} A m^2	248/61	S	plate	high alt
14	*Richmond and Hood* [2003]	C	194/−14	1.90×10^5 A	194/29	N	disk	low/high alt
	Frawley and Taylor [2004]	3	194/−14.8	16 A/m	7.1/24	N	dipole/prism	high alt
	Hood et al. [2005]	A2a	194.3/−11.8	4.90×10^{16} A m^2			plate	high alt
	Hood et al. [2005]	A2b	191.4/−16.6	3.50×10^{16} A m^2	171/33	N	plate	high alt
	Hood et al. [2005]	A2c	195.7/−22.6	2.20×10^{16} A m^2			plate	high alt
15	*Frawley and Taylor* [2004]	4	196.7/−32.1	23 A/m	90.6/19.4	N	dipole/prism	high alt
16	*Quesnel et al.* [2007]	AB-B	199/−35	1.70×10^{16} A m^2	299.2/45.9	N	dipole/prism	low/high alt
	Hood et al. [2007]	A8a	200.8/−54.5	3.30×10^{16} A m^2	198/38	S	plate	high alt
	Hood et al. [2007]	A8b	197/−56.2	3.20×10^{16} A m^2			plate	high alt
17	*Quesnel et al.* [2007]	AB-C	204/−32	3.40×10^{16} A m^2	221.1/44.3	N	dipole/prism	low/high alt
18	*Arkani-Hamed* [2001]	M7	214/−5	14.66 A/m	40/−35	N	prism	sph 50, 380 km alt
	Richmond and Hood [2003]	F	215/−4	1.30×10^5 A	227/66	N	disk	low/high alt
	Frawley and Taylor [2004]	2	215/−8.6	2.7×10^{16} A m^2	25.6/69.9	N	dipole/prism	high alt
	Arkani-Hamed [2004b]	4	216/−7	18.87 A/m	346/−46	N	prism	low/high alt
	Hood et al. [2005]	A4a	214.9/−5.5	1.60×10^{16} A m^2	178/30	N	plate	high alt
	Hood et al. [2005]	A4b	210.6/−6.2	8.00×10^{16} A m^2			plate	high alt
	Boutin and Arkani-Hamed [2006]	4	216/−7	N/R	254/25	N	prism	high alt (1)
	Boutin and Arkani-Hamed [2006]			N/R	257/23	N	prism	high alt (2)
19	*Arkani-Hamed* [2004b]	7	225/−45	42.16 A/m	111/−42	N	prism	low/high alt
	Boutin and Arkani-Hamed [2006]	7	225/−45	N/R	291/21	N	prism	high alt (1)
	Boutin and Arkani-Hamed [2006]			N/R	296/19	N	prism	high alt (2)
20	*Richmond and Hood* [2003]	E_a	229/−25	2.10×10^5 A	325/51	N	disk	low/high alt
	Richmond and Hood [2003]	E_b	232/−33	2.10×10^5 A	314/54	N	disk	low/high alt
21	*Frawley and Taylor* [2004]	1	252.3/−28.5	1.9×10^{16} A m^2	341.9/36.3	N	dipole/prism	high alt
	Arkani-Hamed [2004b]	8	255/−27	17.65 A/m	351/17	N	prism	low/high alt
	Boutin and Arkani-Hamed [2006]	8	255/−27	N/R	197/−3	N	prism	high alt (1)
	Boutin and Arkani-Hamed [2006]			N/R	190/−13	N	prism	high alt (2)
	Hood et al. [2005]	A7a	254.2/−26.4	1.70×10^{16} A m^2	192/27	N	plate	high alt
	Hood et al. [2005]	A7b	250.5/−22.1	8.00×10^{15} A m^2			plate	high alt
22	*Frawley and Taylor* [2004]	7	294.8/−37.2	3.50×10^{16} A m^2	318.9/58.3	N	dipole/prism	high alt
	Arkani-Hamed [2004b]	9	295/−33	28.73 A/m	182/8	N	prism	low/high alt
	Hood et al. [2005]	A3	297.5/−34.6	1.50×10^{16} A m^2	196/43	S	plate	high alt
	Boutin and Arkani-Hamed [2006]	9	295/−33	N/R	174/4	S	prism	high alt (1)
	Boutin and Arkani-Hamed [2006]			N/R	167/5	S	prism	high alt (2)

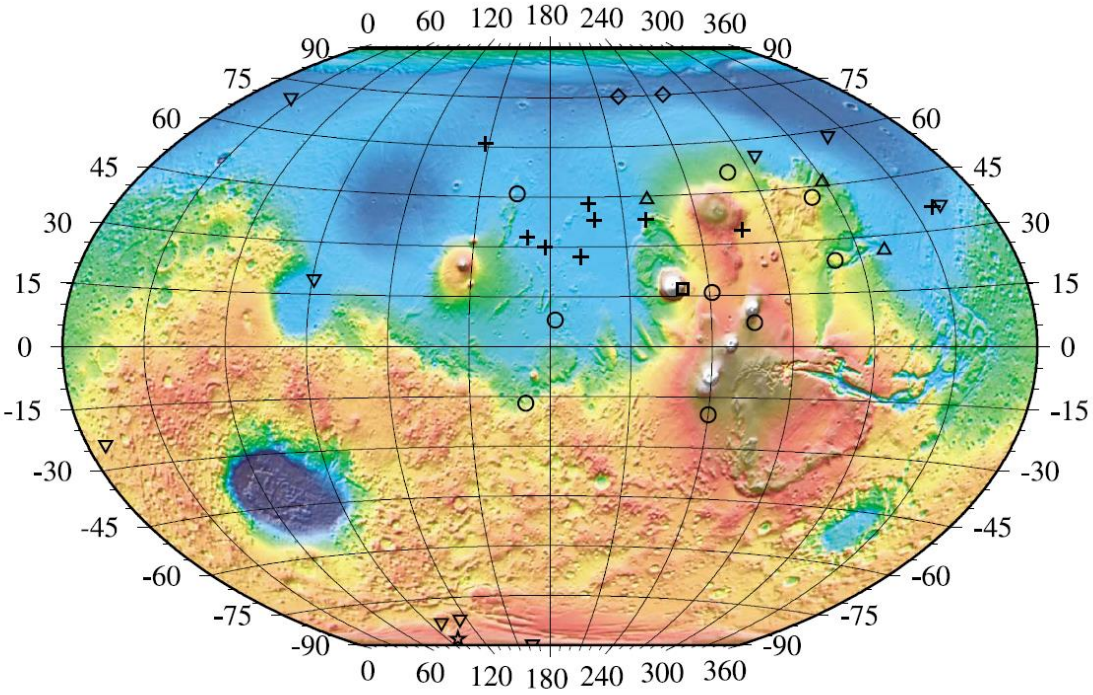

Figure 2.1. Paleopoles from other researchers (Milbury et al., 2010). The poles from Hood et al. (2005, 2007) are crosses, Arkani-Hamed and Boutin (2004) are circles, Frawley and Taylor (2004) are inverted triangles, Sprenke (2005) is a square, Langlais and Purucker (2007) is a star, Quesnel et al. (2007) are triangles, and Mutch et al. (1976) and Hood et al. (2005) are diamonds.

Chapter 3. Methodology: From the Total Gradient Field to Source Regions and Their Association with Chronostratigraphic Ages

Total Gradient

To locate magnetic sources and establish magnetization boundaries, the total gradient (TG) magnetic field was used. TG is invariant of the magnetization direction for two-dimensional sources and acts as a source detector or a source edge detector, depending on the width of the source, the source geometry, and the source to observation distance (Ravat, 2011). The total gradient is given by: $TG = \sqrt{\left(\frac{\partial M}{\partial x}\right)^2 + \left(\frac{\partial M}{\partial y}\right)^2 + \left(\frac{\partial M}{\partial z}\right)^2}$, where M is the total intensity magnetic anomaly or a magnetic field component (z-component for this study). The operators for the relationship between spherical and Cartesian coordinates are: $\frac{\partial}{\partial x} = -\frac{1}{r}\frac{\partial}{\partial \theta}$, $\frac{\partial}{\partial y} = \frac{1}{r sin\theta}\frac{\partial}{\partial \emptyset}$, and $\frac{\partial}{\partial z} = -\frac{\partial}{\partial r}$. The radial derivative can be computed by differentiating the expression of the field in spherical harmonics (e.g., Plattner and Simmons, 2014) or by numerically taking the derivative from data at two different altitudes chosen to minimize noise and highlighting the signal useful for interpretation. For TG from observed fields, we computed the vertical derivative from the field computed at two elevations using the spherical harmonic expansion of coefficients from Langlais et al. (2010). By performing trials of computing fields from Langlais and others' (2010) coefficients at different altitudes, it was found that a stable TG field could be determined at very low altitude (e.g., 10 km) despite the fact that much of the data used in the Langlais et al. (2010) model were at altitudes

between 100 and 400 km.

A model study (Figures 3.1 and 3.2) shows the utility of the TG field in interpreting source characteristics; it also shows how the coalescence of the fields at increasingly higher altitudes is reflected in the TG field. Figure 3.1 (a) shows the profile of the z-component anomaly across a 10 km thick and 5° wide prism placed at the surface (shown in black) for different inclinations of the magnetic field with respect to horizontal. Even in the z-component there is significant anomaly skewness for non-vertical magnetization inclinations. Figure 3.1(b) shows the TG field for the same inclinations of magnetization. The maxima delineate the edges of the source. Figure 3.2(b) shows how the TG maxima merge with increasing depth to source. Even still, the TG field is very useful for source location as it either shows the edges or the center of a source depending on depth and source geometry/width. Whether the TG maximum is at the edge or the center can be generally deciphered from comparison of the anomalous magnetic field and the TG field. TG field is especially invaluable for source location on Mars because the orientation of the main field at the time of magnetization is unknown (Ravat, 2011), and it could be different for different anomalies based on several paleopoles already in the literature determined from isolated anomalies.

A stable TG field was calculated at 10 km from the z-component of the crustal field model of Langlais et al. (2010) (Figure 3.3). Generally, stable fields at lower altitudes cannot be obtained by downward continuation without enhancing noise. This crustal field model, however, involves data spread over a large altitude range (over 300km) from mapping orbit (MO), science phasing orbit (SPO), and aerobraking (AB) satellite phases, and also total intensity data from electron reflectometry (ER) at 185 km

ionosphere bounce points in the regions of weak fields. Having these data spread in altitude over 300 km provides a "built-in global downward continuation function" when determining spherical harmonic coefficients and thus a more stable downward continuation can be achieved in this case (personal communication, Ravat, 2014). The fields >5 nT/km in magnitude in the map in Figure 3.3 are inferred to be the most likely magnetic source regions except where noise is high. Based on comparison of the TG field and the z-component magnetic fields computed at 10 km and 150 km respectively, purple regions are largely either non-magnetic, or the magnetization over these regions is sufficiently small, and/or their sources produce only short-wavelength anomalies such that they are completely attenuated below noise level at the observation altitudes. The regions of large impacts that demagnetized the crust are also associated with < 5nT/km TG fields at 10 km altitude (e.g., Hellas, Argyre, Isidis, Utopia in Figure 3.3) which lends support to the idea that the regions are devoid of magnetic sources.

The z-component field (or radial field as used by Milbury and Schubert, 2010) over magnetic sources has skewness effects related to magnetization inclination which makes it difficult to associate ages to magnetic source regions; the TG, a gradient field, is more closely associated with the edges of sources than the components themselves. In addition, using the TG of the z-component field as opposed to just the z-component field yields a better signal to noise ratio in comparison to individual components through both theoretical error analysis (as discussed below) and comparison of noise in numerical computations of Mars magnetic fields at different altitudes (performed but not shown here).

There are several geophysical and mathematical reasons for using TG fields in

this analysis. Downward continuation cannot recover short-wavelength signal attenuated to the noise level at the observation altitude, but it improves resolution of all anomaly features that are above the noise level of the data. In addition, the TG field is a gradient field and thus has shorter wavelengths than the original components. Error analysis reveals that the calculation of the TG field intrinsically improves the signal quality in comparison to the components themselves. There are several reasons for smaller errors in the TG field than those in the components (Taylor, 1996). First, it can be shown that the error in the TG field is the sum in quadrature (see δM below) which is never larger than the sum of errors in its individual terms for independent random errors,

$$\delta M = \sqrt{\left(\left|\frac{\partial M}{\partial x}\right| \delta x\right)^2 + \left(\left|\frac{\partial M}{\partial y}\right| \delta y\right)^2 + \left(\left|\frac{\partial M}{\partial z}\right| \delta z\right)^2} \text{ and } \delta M \leq \left|\frac{\partial M}{\partial x}\right| \delta x + \left|\frac{\partial M}{\partial y}\right| \delta y + \left|\frac{\partial M}{\partial z}\right| \delta z.$$

This limits the random part of the errors in the TG field relative to the components (summing here is analogous to obtaining the mean of observations, but without dividing by the number of observations, further reducing the error in the estimate). Second, the correlated errors compensate for errors of the individual terms. This is the case here for the components because they obey Laplace's equation, $\frac{\partial^2 V}{\partial x^2} + \frac{\partial^2 V}{\partial y^2} = -\frac{\partial^2 V}{\partial z^2}$, where V is the magnetic potential. Thus, the correlated part of the error of x- and y- derivatives compensates for the error in the z-derivative, reducing significantly the error in the TG field ($i.e.,\ \left|\sigma_{xyz}\right| \leq \sigma_x \sigma_y \sigma_z$, where σ is the standard deviation, Taylor, 1996). And third, squaring the derivatives in the TG field computation, before summing, amplifies the difference between observations with higher signal to noise ratio and suppresses observations with lower signal to noise ratio, making the observations of stronger gradients readily perceptible. In addition, because these components/derivatives are orthogonal, each has independent information. Thus, the signal created by addition of

these independent orthogonal components can never reduce, and the random part of the noise in these components will always reduce (personal comm., D. Ravat, 2014).

There is now available a cleaner, but smoother, magnetic field model from the MGS MAG data (Morschhauser et al., 2014, spherical harmonic degree and order 110 and L1-norm optimization) that can be downward continued to altitudes as low as the planetary surface which clearly increases the resolution of the features identified in comparison to the Mars field models at 200 km altitude (e.g., Purucker et al., 2000; Arkani-Hamed, 2001a; Arkani-Hamed. 2004). The TG from this model shows the same features as the TG field used in this study, but with slightly less resolution due to its lower spherical harmonic degree in comparison to Langlais et al. (2010) field model.

Chronostratigraphic Ages and Geologic Boundaries on Mars

Accurately establishing source location makes it possible to make better comparison of magnetized regions with chronostratigraphic units. Figure 3.4 shows the chronostratigraphic map of Mars created in ArcGIS by Skinner et al. (2006). The map is divided by age and by deposit type. The 2006 map is the digitized Viking-based Atlas of Mars, 1:15,000,000 Geologic Series maps (USGS I-1802A-C) originally published in 1986 by Scott and Tanaka in equidistant cylindrical projection centered on 0°N/0°E. For the 1986 map, geologic units were identified and mapped from 1:2,000,000-scale photomosaics and individual images, ranging from 130 to 300 m/pixel (Scott and Tanaka, 1986). Relative ages of the units were established by superposition/cross cutting relationships and by crater size-frequency distributions (Scott and Tanaka, 1986.). Due to crater degradation, resurfacing, and declining crater-flux rates, relative ages of increasingly older surfaces on

Mars are determined by densities (concentration) of progressively larger craters (Scott and Tanaka, 1986). For relative-age correlation within the Amazonian, Hesperian, and Noachian Systems, Scott and Tanaka selected density scales for craters larger than 2, 5, and 16 km in diameter. Overlap of the scales was empirically determined by calculating ratios of crater densities at different diameters for units most likely to preserve a wide range of crater sizes (Scott and Tanaka, 1986). Geologic map units were defined primarily by geomorphologic, topographical and albedo characteristics in addition to superposition and structural relationships. Problems still exist in assigning absolute ages to Mars' geology and determining rates of surface processes (Scott and Tanaka, 1986).

The age divisions from oldest to youngest are Noachian, Hesperian and Amazonian. Hartmann and Neukum (2001) combine results from Neukum et al. (2001) and Ivanov (2001) with crater counts to estimate ages of Martian surfaces. Those models were combined with studies of Martian meteorites (Nyquist et al., 2001) to establish a rough chronology of Martian history. Figure 3.5 shows that Hartmann and Neukum (2001) place the boundary between Noachian and Hesperian at approximately 3.7 Ga and the boundary between Hesperian and Amazonian at approximately 3.1-2.9 Ga.

Splitting the map in Figure 3.4 into chronostratigraphic units (Figure 3.6) makes it possible in ArcGIS to calculate area of overlap between regions showing TG magnetic field anomalies and the individual chronostratigraphic units. Prior to this calculation some important issues with the magnetic anomaly map and the chronostratigraphic map needed to be addressed. One consideration for the area of overlap calculations was that the derivatives at the poles have higher amplitudes than the original z-component anomalies and therefore are clearly noise. The TG equation written in the Cartesian coordinate

system, or $TG = \sqrt{\left(\frac{\partial M}{\partial x}\right)^2 + \left(\frac{\partial M}{\partial y}\right)^2 + \left(\frac{\partial M}{\partial z}\right)^2}$ reveals the source of this error. In the computer program used to determine TG, the computations of theta and phi derivatives are performed by computing first the Fourier transforms of data on a latitude-longitude grid and then converting these derivatives into the spherical coordinate system. The grid spacing was 0.1° in order to retain the spatial resolution. At the equator on Mars, 0.1° spacing is approximately 6 km, but at the poles 0.1° spacing mathematically tends to zero kilometers. Since the physical distance of data points is very small, when TG is calculated at the poles through Fourier transforms in the Cartesian coordinate system, it is equivalent to a division of very small numbers in both the numerator as well as the denominator. TG values at the poles are unstable primarily due to the near zero denominator. The near zero numerator in this calculation is actually detrimental to understanding the instability issue because it limits the computed values from exceeding the realistic realm. Consequently, in assessing the areas covered by magnetic features of certain ages, a set of calculations were also done excluding polar units.

In addition, classifying the areas of polar deposits as Amazonian is problematic because they lie on top of units that are certainly Noachian in age based on the units surrounding them. This becomes apparent because the units Amazonian polar ice (Api) and Amazonian Polar (Apl) show magnetization and ice cannot be magnetized. Figure 3.7 shows closed black lines that represent the boundaries for units Api and Apl with the underlying TG fields that cannot be attributable to these units. Calculations were also done to place the suspect units (Api & Apl) in with the Noachian terrain. To clarify this ambiguity, future work should be done to use topographic data along with chronostratigraphic data and compare this to selected sources where depth to source can be determined using

depth determination techniques (e.g., Blakely, 1995) with future low altitude data collected over a longer time period (e.g., the MAVEN mission).

Comparison of the Total Gradient Fields with the Age Units

For different strengths and widths of magnetic sources, there can be different TG field cutoff for determining whether a particular region is magnetic or not. Overlap area was calculated between the TG map cutoffs of greater than or equal to 10, 15, 25, 50, 100 and 200 nT/km with Noachian, Hesperian, Amazonian units and also for units with no age designation. Additional information on this process is provided in Appendix 1. The results are provided in Table 3.1 for the calculations of overlap of chronostratigraphic units with regions containing the specified TG cutoffs. The units with Amazonian polar deposits (Apl) and Amazonian polar ice (Api) were included in the Noachian for the following example calculations. The percentages represent the cells of overlap per the total cells of the specified cutoff. For the Noachian and TG ≥10 nT/km cutoff $\frac{total\ cells\ of\ overlap\ of\ the\ Noachian\ with\ TG \geq 10\ nT/km}{total\ cells\ of\ TG \geq 10\ nT/km} x\ 100\%$ or $\frac{19281\ cells}{30957\ cells}$x 100%. For detailed explanation of methods and calculations where units Api and Apl were omitted, see Appendix 1. Calculations removing Api and Apl show the same general trend, but with the Noachian period showing fewer cells of overlap for all categories.

The most interesting observation from this analysis is that as the TG cutoff increases, the amount of Amazonian terrain that is represented all but disappears (see Figures 3.8 and 3.9). This is due in part to the shape of the TG field. Suppose Figure 3.1(b) shows a Noachian source (black box), immediately adjacent to an Amazonian terrain. The tail of the magnetic signal from the Noachian source would map in the

Amazonian terrain. Removing weak signals or increasing the cutoff level, removes erroneous age designations attributable to the tails of the TG field. Figure 3.10 shows three different TG contour levels (A ≥5nT/km, B ≥15nT/km and C ≥25nT/km). The red dashed box in these figures contains within it an example of a Noachian source that has weak TG fields that are erroneously attributed to Amazonian terrain. Looking at this region from Figure 3.10A to 3.10C shows that with increasing TG cutoff, all the magnetization becomes contained within Noachian regions. In other words, the red dashed box region shows how the tails of the TG signal within the Amazonian region disappear with increasing cutoff. This is an example of a Noachian source(s) located adjacent to Amazonian terrain that has weak TG fields that are erroneously attributed to the Amazonian unit.

It is possible that these Amazonian weak fields may also be attributable to the depth of the source since the observed magnetic signal attenuates with depth (indicating the source of magnetization maybe a lower unit stratigraphically, i.e. Hesperian or Noachian). Figure 3.11 shows an example of a magnetic source that has weak TG fields that are erroneously attributed to Amazonian terrain (peach). This source is likely located in either Noachian (purple) or Hesperian (green) units within the region. While using TG field helps some with this issue because it is inherently reflective of more near surface sources than deep ones (gradient fields suppress longer wavelengths from deeper sources) it cannot completely remove the problem of deeper sources (see Figure 3.2b). Of note is the fact that, with increasing TG cutoff, a significant amount of Hesperian terrain continues to be represented, even at high magnetic cutoffs. These results add support for the idea that the core field continued to be active through at least the early Hesperian.

While Figure 3.10 contours demonstrate how the shape of the TG field causes most of the weak fields attributed to the Amazonian terrain, there are also some strong TG areas in Hesperian and Amazonian terrains. Figure 3.12 shows the observed field, TG anomalies, and chronostratigraphic maps associated with a 25 nT/km TG field anomaly located under an Amazonian surface age unit in the Olympus Mons Formation, aureole members 3 and 4. Chronostratigraphy (Figure 3.13 from Skinner et al., 2006, based on Scott and Tanaka, 1986) places the peak of the anomaly in the Amazonian terrain (Aoa3 & Aoa4) adjacent to Hesperian ridged plains material (Hr). Figure 3.14 shows the same profile in the updated Mars map of geology (Tanaka et al., 2014). On the 2014 map, the anomaly falls into Amazonian apron (Aa), Amazonian/Hesperian transition undivided (AHtu), and late Amazonian apron (lAa). This profile and the updated map suggests the possibility that the source of magnetization could be Hesperian from unit AHtu or perhaps late Amazonian from unit lAa. In addition, the pattern of this unit is not distinguishable from the Noachian regions west of this unit (i.e., it is neither subdued nor stronger in one case or the other, and both could be a result of deeper sources). This makes it seem as if Amazonian crust must be magnetized, but a closer look at the geologic map reveals Noachian inliers (see Figure 3.13, Nf, Npl1 and Npl2) within the Amazonian volcanic unit.

Figure 3.15 also shows an example of a high amplitude TG anomaly located in Amazonian terrain (~50nT/km) and an anomaly in Noachian terrain (~50nT/km). The profile shows improvement in locating sources in the TG peaks (edges of sources) with respect to the peaks of the z-component anomaly fields. The TG calculation has removed skewness and collapsed the signal. Based on Mars geology (Figure 3.16), the Amazonian

anomaly peak falls into the geologic units Tharsis Montes Formation members 4 (At4) and 5 (At5) and the Noachian anomaly peak falls into Noachian cratered units (Figure 3.16). Examination of this area on the new map in Figure 3.17 places the Amazonian TG anomaly in Amazonian Hesperian volcanics (AHv) and the Noachian peak in Noachian highland units. The new map detail suggests ambiguity in age designation of geologic units within these areas. The designation of AHv in the new map gives a sense that the anomaly is either Amazonian or Hesperian, but again the volcanic units of Tharsis could easily overlie Noachian "inlier" units which appear between the Amazonian and Hesperian units in the new chronostratigraphic map (Figure 3.17). Also, the proximity to other Noachian highland units (middle Noachian highland (mNh), Noachian highland undivided (Nhu), late Noachian highland (lNh), and early Noachian highland (eNh) in Figure 3.17) covering a larger area to the south (at 110°W longitude) cannot be ignored. In addition, Figure 3.18 shows TG sources which are clearly Noachian with weak fields erroneously attributed to the Hesperian unit between 10° to 20°N latitude and between 5° to 15°S latitude. Examination of Figure 3.19 and 3.20 shows these Noachian sources are located in close proximity to the source shown in 3.15. Further demonstrating that the volcanic units could indeed overlie Noachian terrain and significant portions of both Amazonian and Hesperian units showing TG signal in this area could be thus misattributed.

The assumption that the surface age is close to the age of magnetization (Milbury and Schubert, 2010) is reasonable for Noachian Mars highlands as most of them have formed magmatically/volcanically (Craddock and Greeley, 2009) and not by accretionary processes like on the Earth. While it is possible that Hesperian and Amazonian surface

age terrains showing magnetism may be underlain by crust magnetized during the Noachian, most scenarios where surface age may be different than the age of magnetization acquisition occur at the edges of geologic magmatic terrains such as the high TG anomalies in Figure 3.12 and 3.15. Near the edges, there could be a non-magnetized intrusion displacing a previously magnetized unit, a later non-magnetic volcanic layer may overlie a previously magnetized terrain (e.g., Tharsis volcanics, Johnson and Phillips, 2005), or tectonism may lead to thrusting of a non-magnetized region on top of a previously formed and magnetized region. There could be occasional later intrusions that might disturb the contiguity of a previously magnetized unit, but that is not likely to alter the surface age of the province. A previously magnetized region could also be buried by sedimentary deposits (e.g., Northern Lowlands) and may show presence of older magnetism in the underlying crystalline crust. With the exceptions of burial by extensive volcanic units or sedimentary deposits, the remaining scenarios discussed above occur near the edges of the magnetized regions. This explanation coupled with the ambiguity in surface age designation within these regions explains the isolated strong TG anomalies shown in Figures 3.12 and 3.15.

As the TG cutoff increases, the amount of Amazonian terrain that is represented diminishes due to the shape of the TG field and depth to source. High amplitude Amazonian anomalies can be attributed to Noachian inliers or lie in areas that have multiple unit designations on the 2014 map of Mars. As TG cutoffs increase, however, a significant amount of Hesperian terrain continues to be represented, even at high magnetic cutoffs. Figure 3.10B shows 15nT/km anomalies located in Hesperian terrain at 60°N latitude that are not located near Noachian inliers. These results add support for the

idea that the core field continued to be active through the early Hesperian. In addition, the new map by Tanaka et al. (2014) re-categorizes significant portions of Amazonian terrain as Noachian, Amazonian/Noachian or Amazonian/Hesperian which increases the percentage of TG anomalies contained within Noachian and Hesperian terrains. In the future, it would be ideal to do tests for statistical significance for the area of Hesperian terrain with TG anomalies to strengthen the case for a dynamo that was active in the early Hesperian. Each cell of overlap could be considered an observation and the TG value associated with each cell could be used to calculate mean and standard deviation based on total observations and observations for each unit (Hesperian, Amazonian, Noachian). The only other convincing way to demonstrate the dynamo was active in the Hesperian is to examine smaller Hesperian volcanic or cratered units and TG fields associated with those features similar to Milbury et al. (2012) discussed in Chapter 4.

Table 3.1 Overlap of chronostratigraphic units with TG by cutoffs. The percentages represent the cells of overlap per the total cells of the specified cutoff. The units Amazonian polar deposits (Apl) and Amazonian polar ice (Api) were included in the Noachian for the following calculations.

TG ≥ 10 nT/km		
Unit	Cells of Overlap	Percentage
Noachian	19281	62.28%
Hesperian	7071	22.84%
Amazonian	3327	10.75%
No age designation	1278	4.13%
TOTALS	30957	100.00%
TG ≥ 15 nT/km		
Units	Cells of Overlap	Percentage
Noachian	13367	66.16%
Hesperian	4131	20.45%
Amazonian	1729	8.56%
No age designation	977	4.84%
TOTALS	20204	100.00%

Table 3.1 (continued)

TG ≥ 25 nT/km		
Units	Cells of Overlap	Percentage
Noachian	6995	69.80
Hesperian	1889	18.85
Amazonian	589	5.88
No age designation	548	5.47
TOTALS	10021	100.00%

TG ≥ 50 nT/km		
Units	Cells of Overlap	Percentage
Noachian	2747	79.58
Hesperian	545	15.79
Amazonian	46	1.33
No age designation	114	3.30
TOTALS	3452	100.00%

Table 3.1 continued

TG ≥ 100 nT/km		
Units	Cells of Overlap	Percentage
Noachian	821	89.43
Hesperian	78	8.50
Amazonian	1	0.11
No age designation	18	1.96
TOTALS	918	100.00%

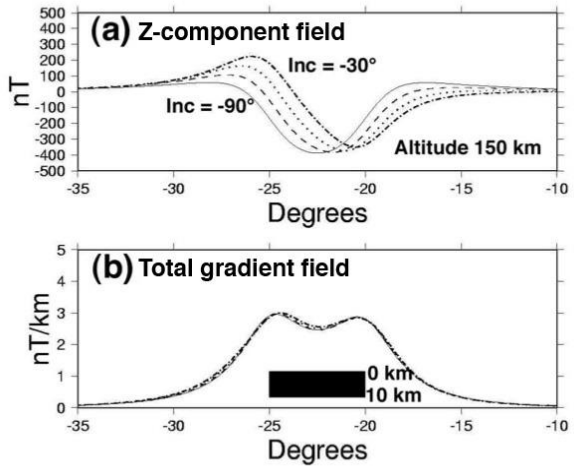

Figure 3.1. (a) Z-component field profiles for different inclinations. Z-component field profiles at 150 km altitude across a source magnetized at inclinations of -30°, -50°, -70°, -90° and (b) TG field profiles for different inclinations. Source is shown in black. (From Ravat, 2011).

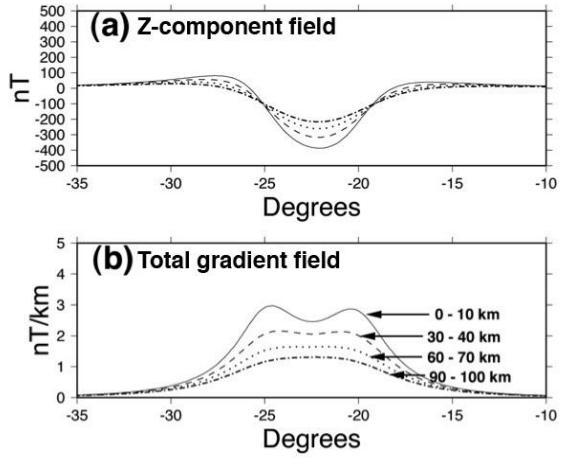

Figure 3.2. (a) Z-component field profiles for different depths. Z-component field across the source for all inclinations as depth of source is varied (b) TG field profiles for different depths. (From Ravat, 2011)

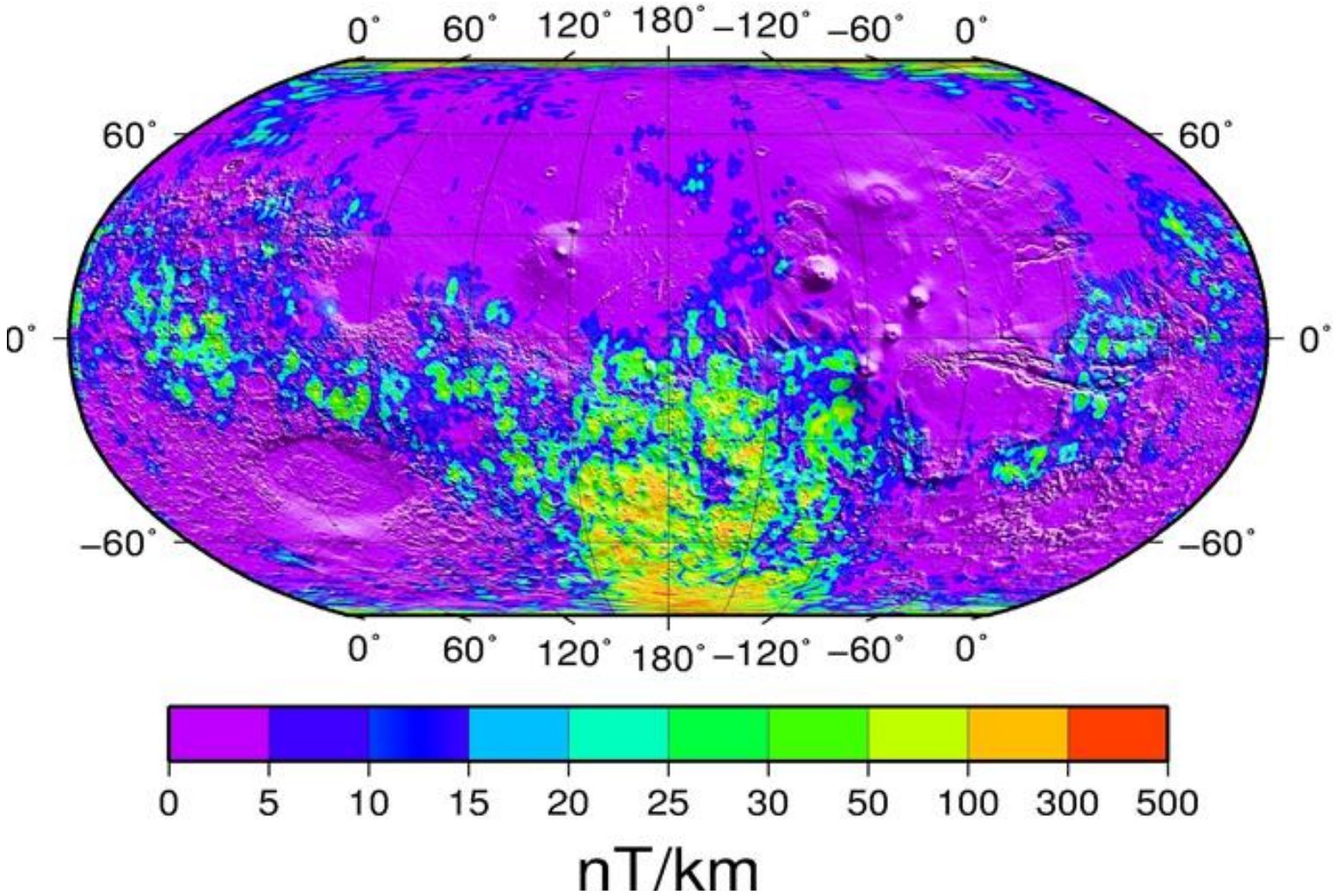

Figure 3.3. Total gradient field at 10 km. TG calculated at 10 km and 0.1° equal area spacing superimposed on a topographic intensity map (Robinson Projection).

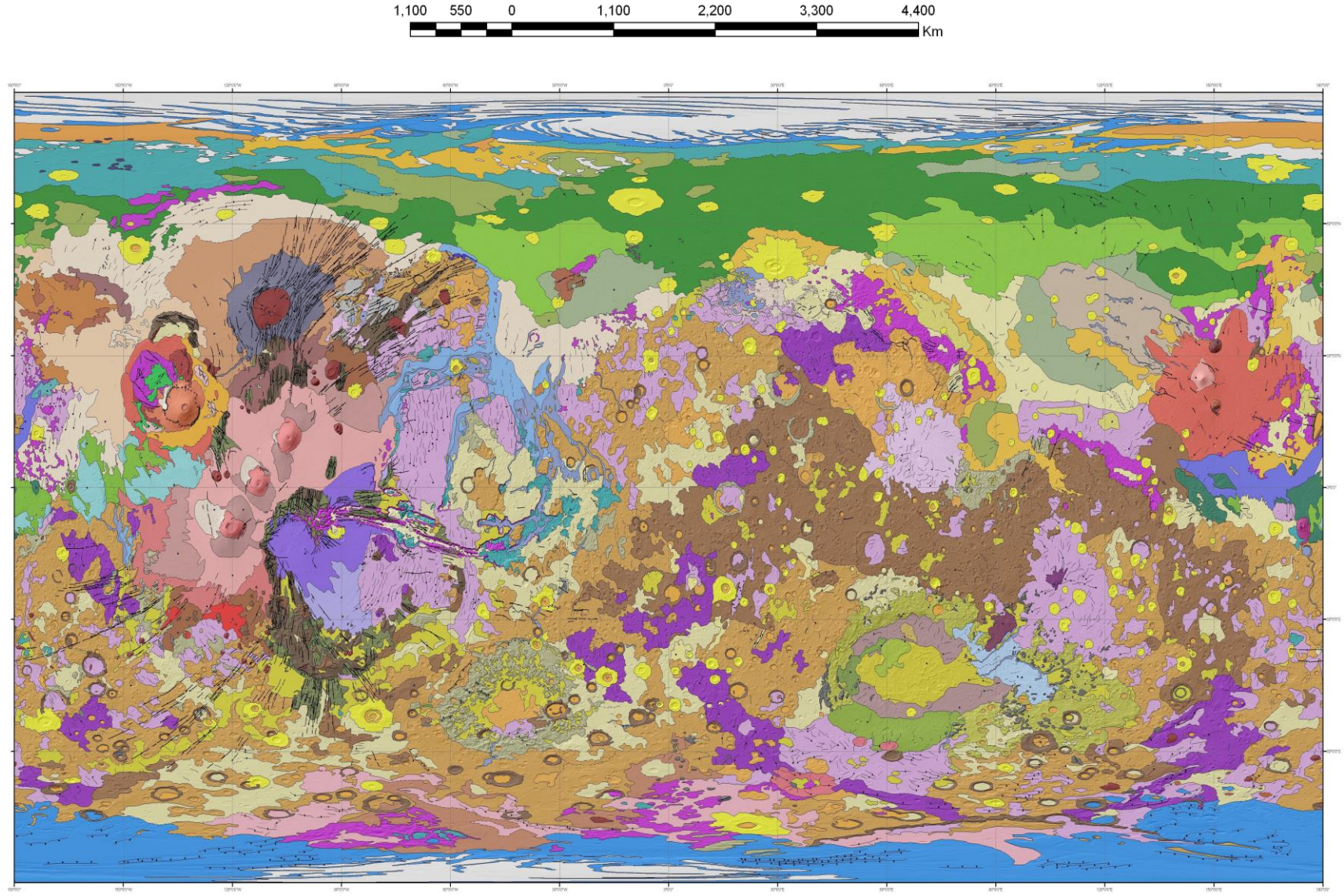
1,100 550 0 1,100 2,200 3,300 4,400
Km

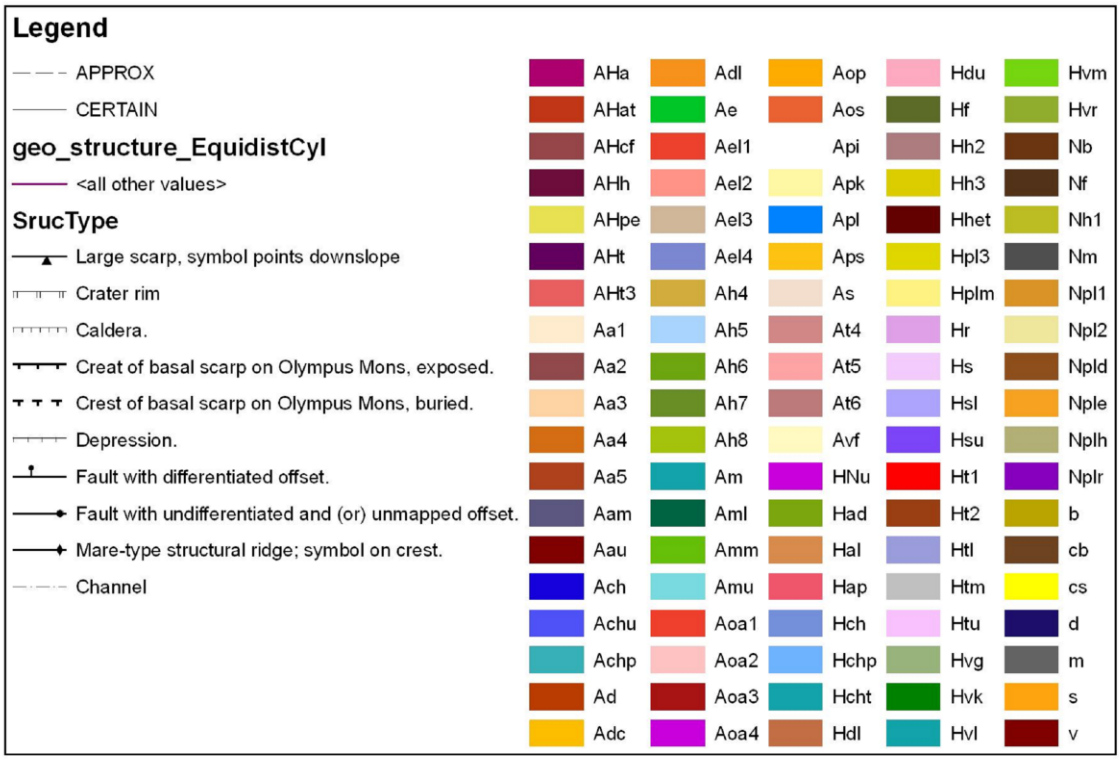

Figure 3.4. Geologic map of Mars. Equidistant cylindrical projection: Skinner et al., 2006.

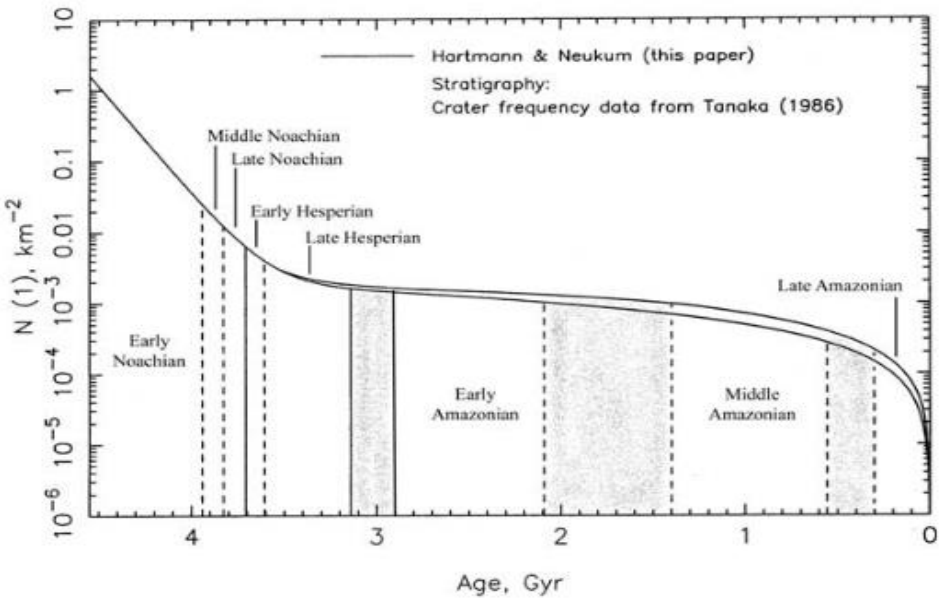

Figure 3.5. Epoch divisions for Mars. Graph from Hartmann and Neukum (2001) showing epochs for Mars based on Scott and Tanaka's (1986) crater densities and Ivanov's (2001) definition of isochrons.

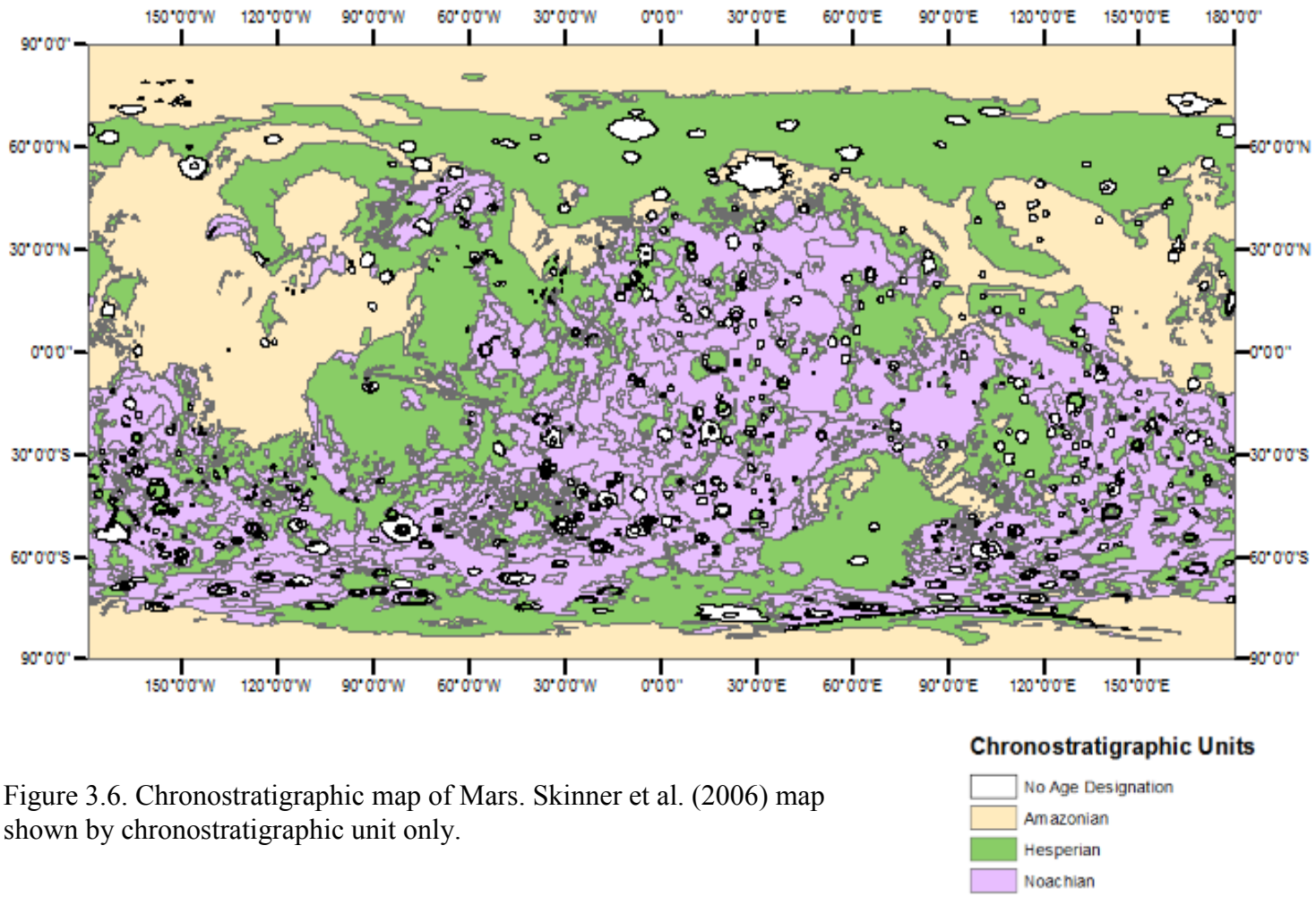

Figure 3.6. Chronostratigraphic map of Mars. Skinner et al. (2006) map shown by chronostratigraphic unit only.

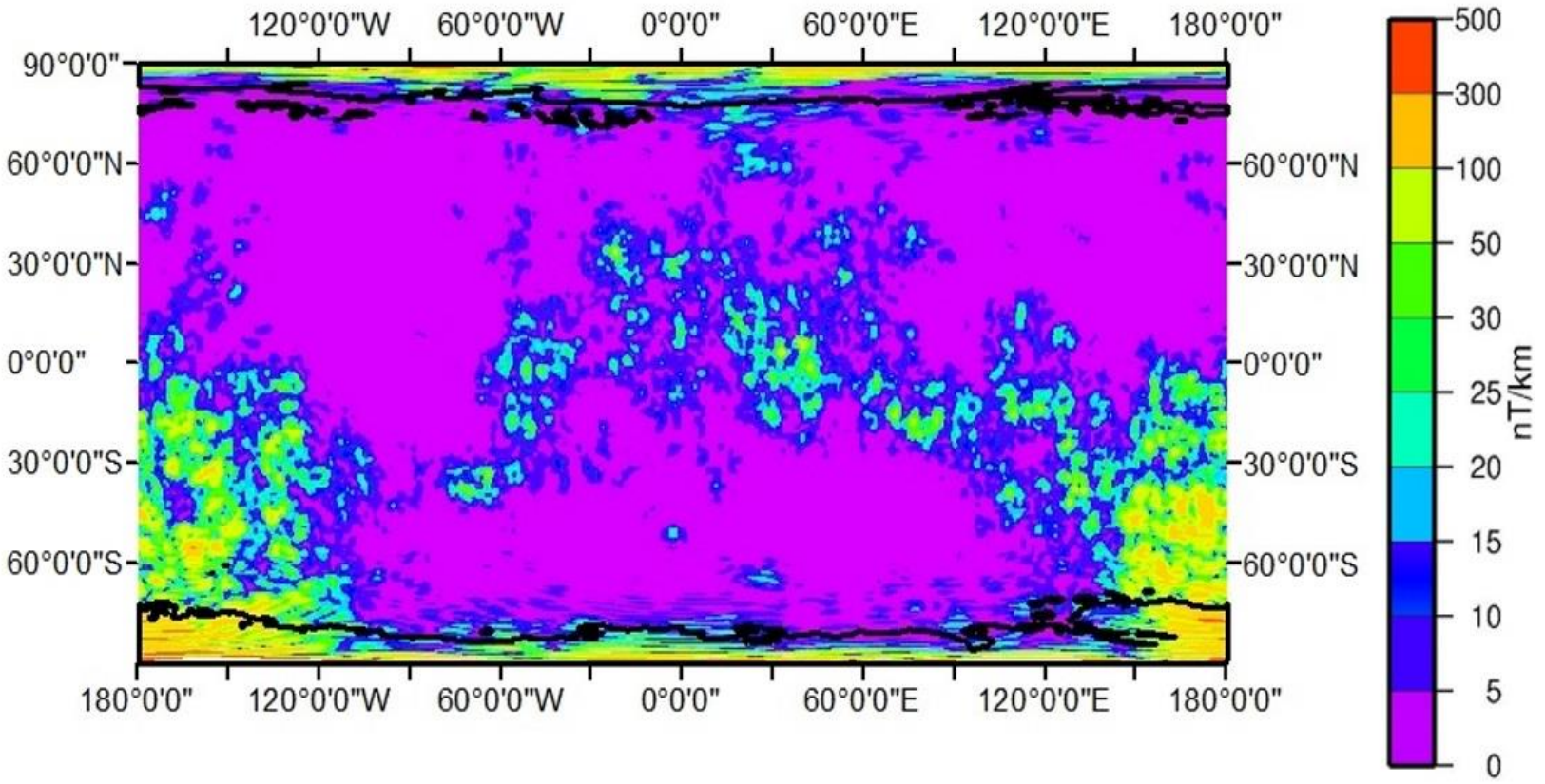

Figure 3.7. Amazonian polar regions on map of Total Gradient. Closed black boundaries located above 80°N and below 75°S show the Amazonian Polar Regions superimposed on the TG map. The magnetic anomalies seen in the region above and below 60° N and S respectively within the black contours should not be attributed to the surface age of Amazonian polar deposit units because those units are non-magnetic and they are underlain by Noachian age crust.

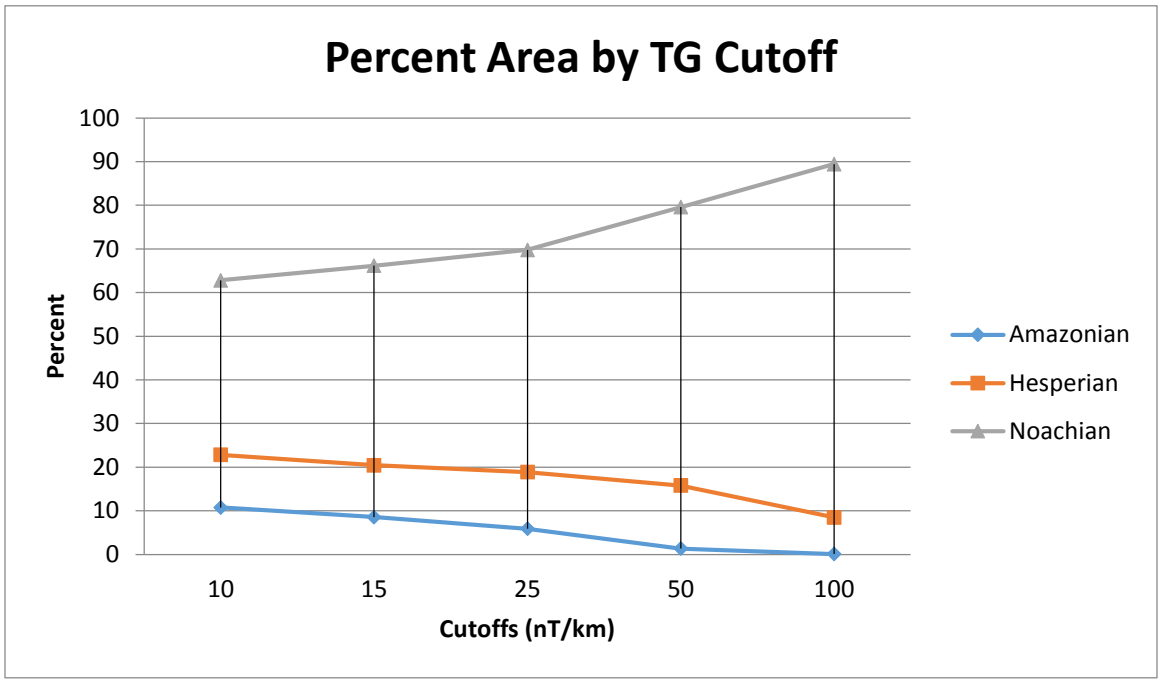

Figure 3.8. Percent area by TG cutoff (see Table 3.1).

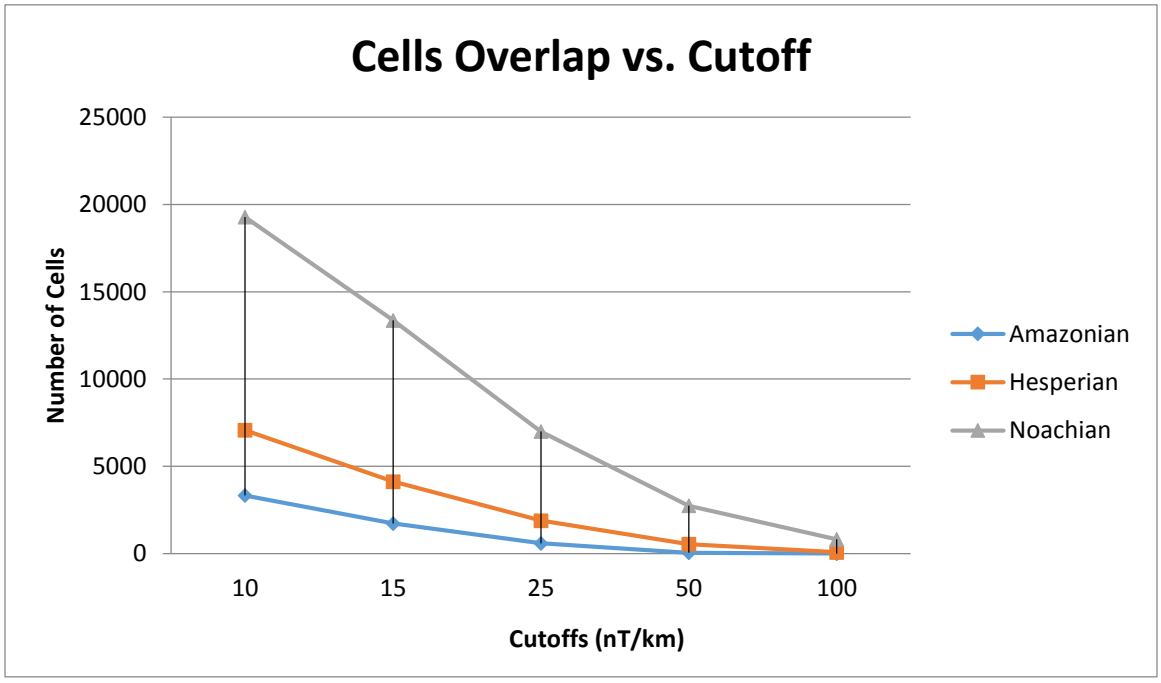

Figure 3.9. Number of cells of overlap by TG cutoff (see Table 3.1).

A)

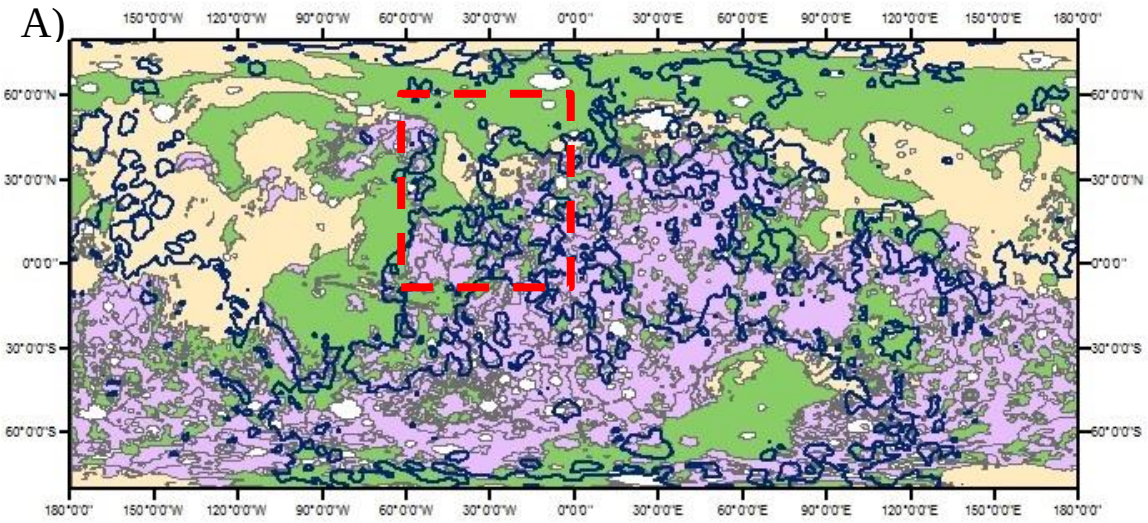

Chronostratigraphic Units

- TG > 5 nT/km
- Amazonian
- Hesperian
- Noachian

B)

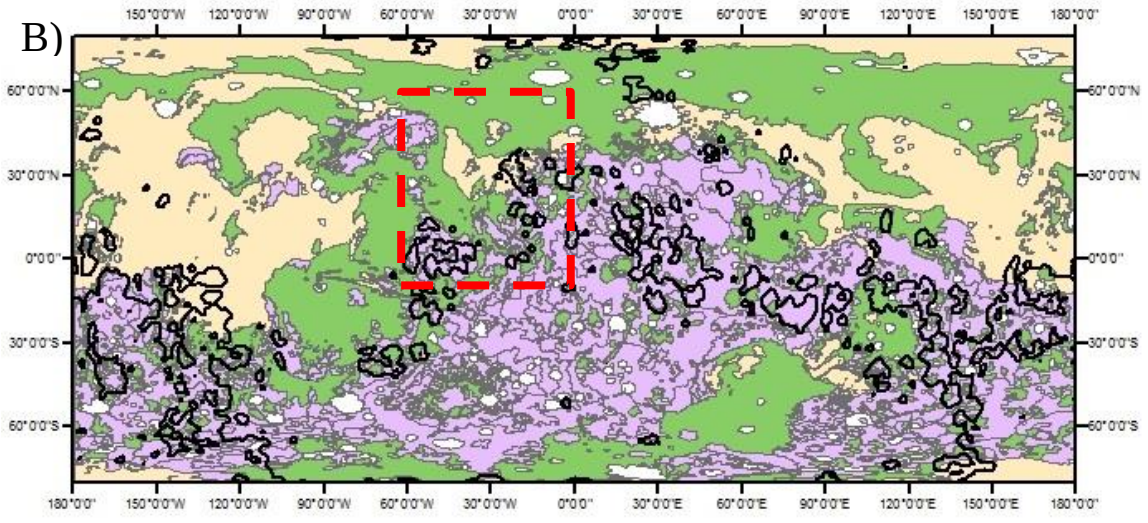

Chronostratigraphic Units

- TG > 15 nT/km
- Amazonian
- Hesperian
- Noachian

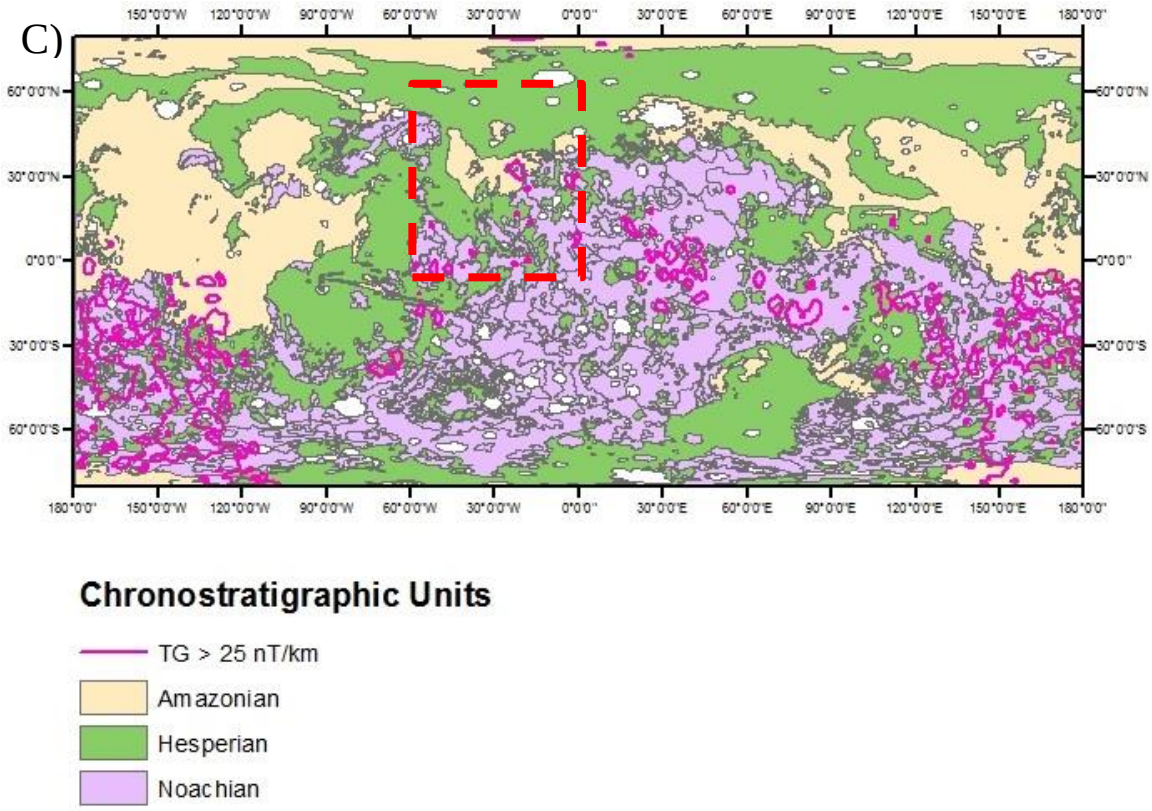

Figure 3.10. A) TG contour for 5 nT/km on chronostratigraphic map of Mars. Blue contour contains areas of TG > 5 nT/km. B) TG contour for 15 nT/km on chronostratigraphic map of Mars. Black contour contains areas of TG >15 nT/km. C) TG contour for 25 nT/km on chronostratigraphic map of Mars. Magenta contour contains areas of TG > 25 nT/km. All contours are on chronostratigraphic units Noachian (purple), Hesperian (green), and Amazonian (peach). Areas above and below 80 degrees latitude were removed from these maps because the TG field is noisy in those regions (see discussion Chapter 3). Red boxes show a region where progressive removal of weaker fields removes TG tails from the Amazonian unit (see discussion Chapter 3).

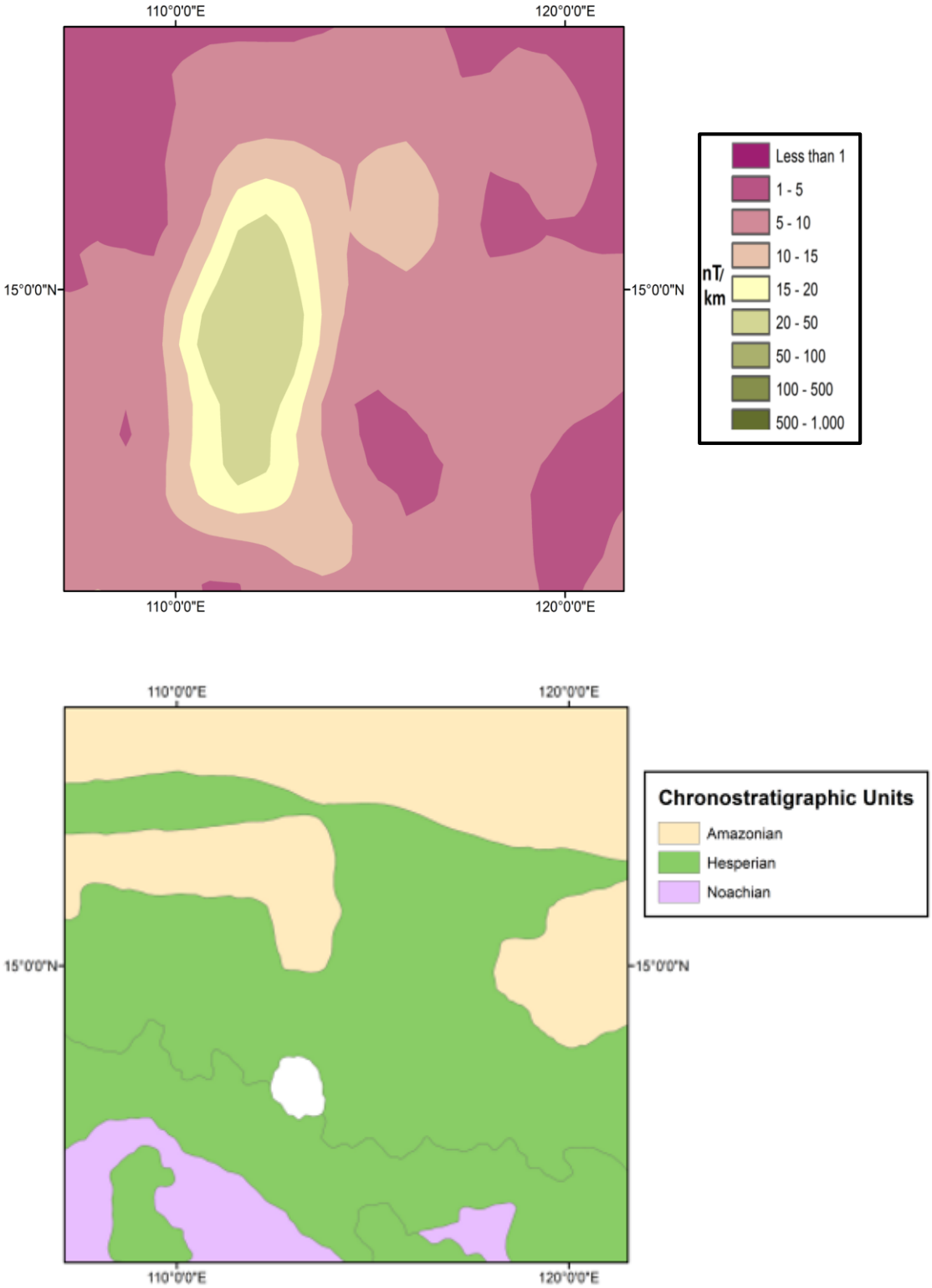

Figure 3.11. Hesperian/Noachian source with weak fields in Amazonian terrain. Top map shows a Hesperian or Noachian source with weak fields that may have been erroneously attributed to the Amazonian Unit as shown in the bottom map.

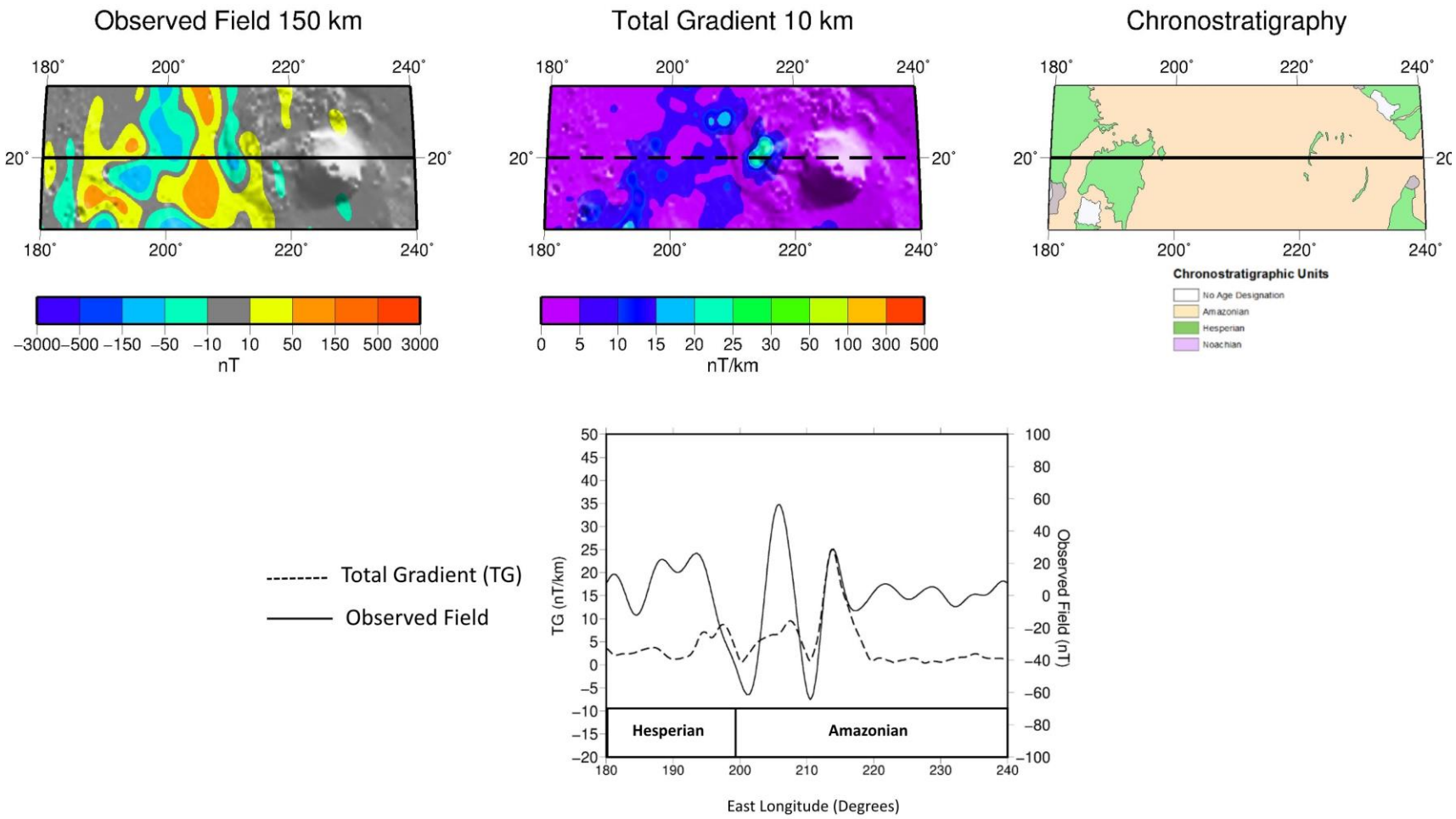

Figure 3.12. High amplitude Olympus Mons anomaly with Amazonian surface age. A profile (black line at 20°N) through the observed field, TG, and chronostratigraphic maps for a magnetic anomaly located under an Amazonian surface age unit through Olympus Mons and the area west of Olympus Mons (primarily the Arcadia Formation). The dashed line in the lower panel represents the TG profile and the solid line represents the Observed Field profile.

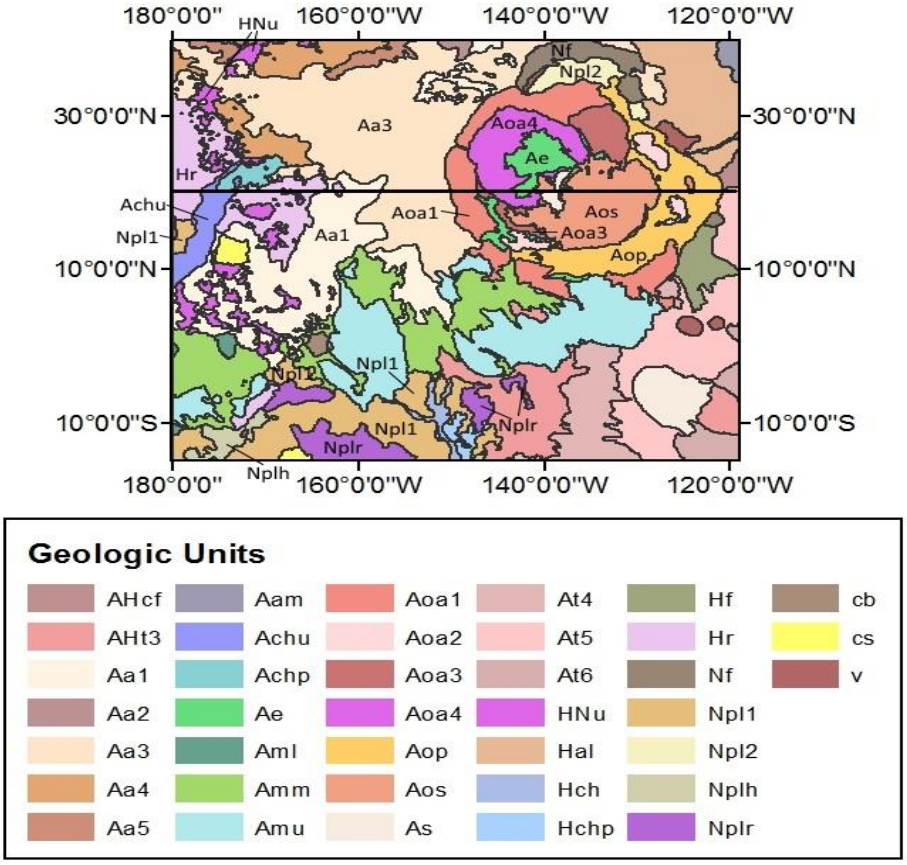

Figure 3.13. Profile high amplitude Olympus Mons anomaly on 2006 map of geology. The profile from Figure 3.11 (black line at 20°N) superimposed on geologic units from Skinner et al. (2006). The units crossed by the profile from left to right are: Hesperian ridged plains material (Hr or eHt on Tanaka et al., 2014, map in Fig. 3.14), Amazonian channel material undivided (Achu or lAv on 2014 map), Amazonian Arcadia Formation Member 1 (Aa1 or lAv on 2014 map), Amazonian Arcadia Formation 3 (Aa3 or lAv on 2014 map), Amazonian Olympus Mons Formation Aureole Member 1 (Aoa1 or Aa on 2014 map), Amazonian Olympus Mons Formation Aureole Member 3 (Aoa3 or Aa on 2014 map), Aos (Ave), and Amazonian Olympus Mons Shield Member (Aop or lAv on 2014 map). Noachian and Hesperian/Noachian units close to the profile are also labeled. HNu (Hesperian Noachian undivided), Npl1 (Noachian plateau sequence, cratered unit), Npl2 (Noachian plateau sequence, subdued cratered unit), Nplh (plateau sequence hilly unit) and Nf (highly deformed terrain material, older fractured material) are present throughout the region (see discussion Chapter 3).

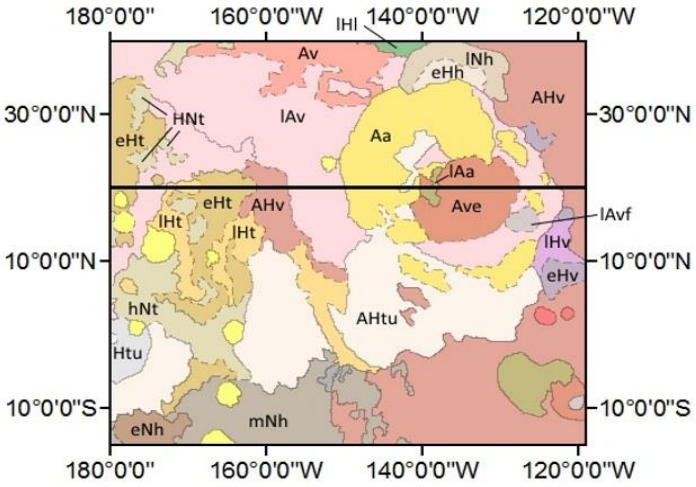

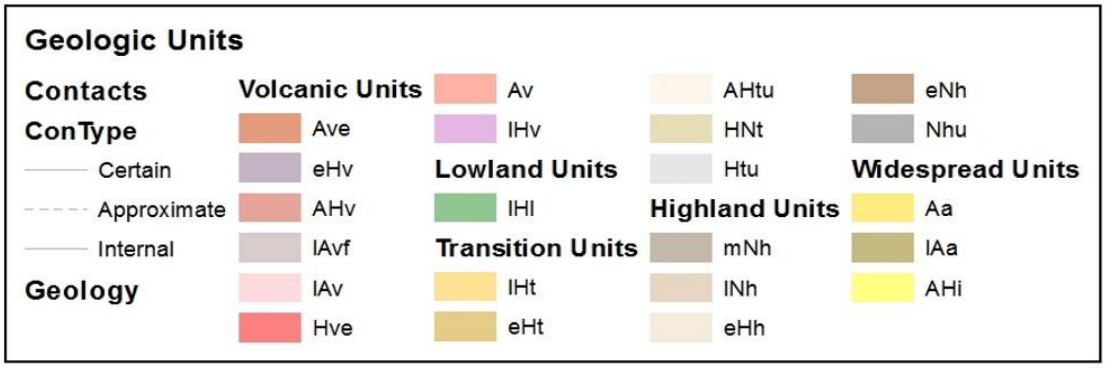

Figure 3.14. Profile high amplitude Olympus Mons anomaly on 2014 map of geology. Profile from Figures 3.12 and 3.13 superimposed on the 2014 map of Mars geology (Tanaka et al., 2014) The profile crosses units eHt (early Hesperian transition), lAv (late Amazonian volcanics), lHt (late Hesperian transition), AHv (Amazonian Hesperian volcanics), lAv (late Amazonian volcanics), Aa (Amazonian apron), Amazonian/Hesperian transition undivided (AHtu), late Amazonian apron (lAa), and Amazonian volcanic edifice (Ave).

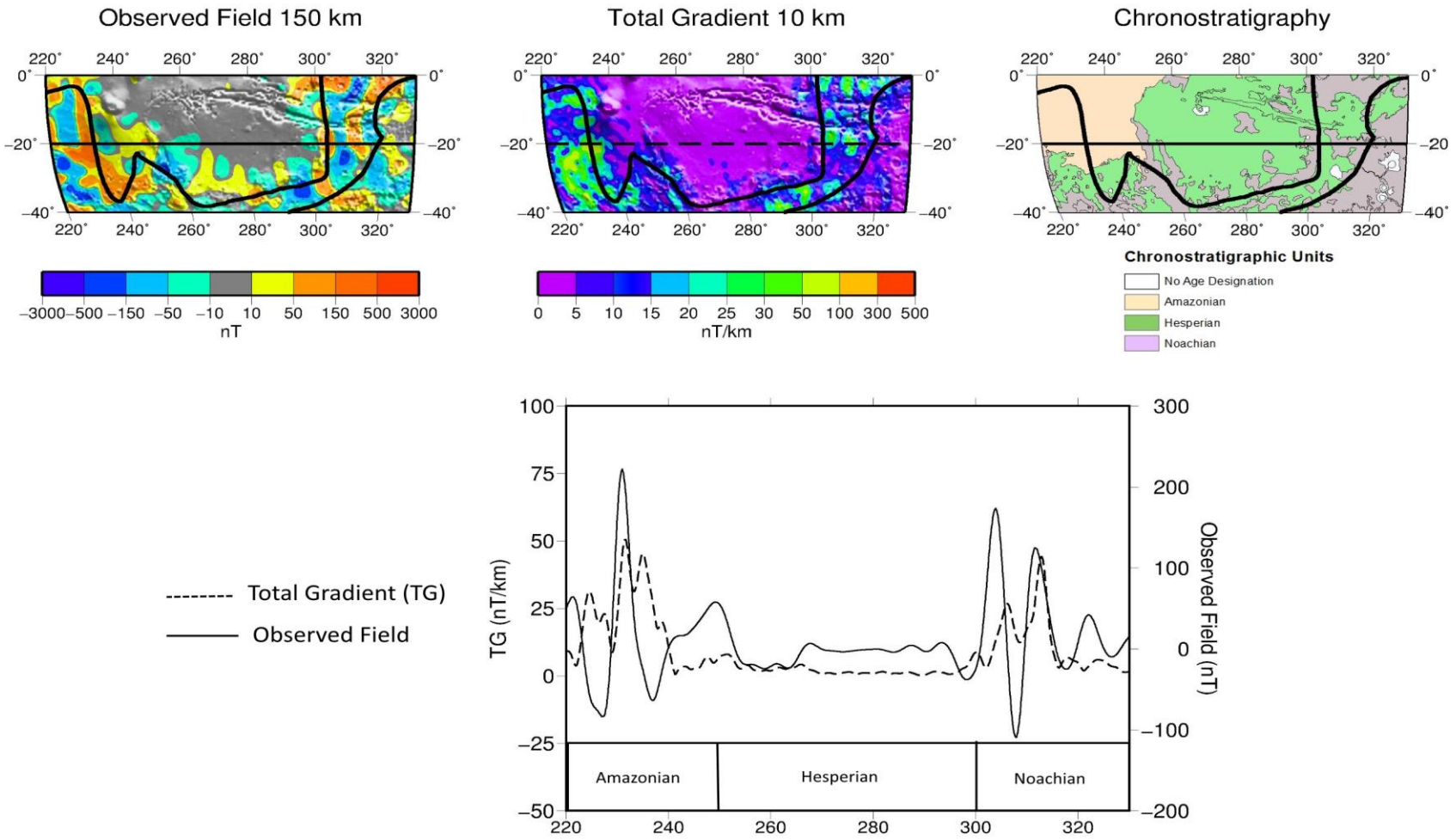

Figure 3.15. High amplitude Tharsis Montes anomaly with Amazonian surface age. A profile (black line at 20°S) through the observed field, TG and chronostratigraphic maps of a magnetic anomaly located under an Amazonian surface age unit within the Tharsis Montes Formation members 4 (At4) and 5 (At5) shown in Figure 3.16. Magnetization in the units classified as Amazonian is near the edge of the Noachian.

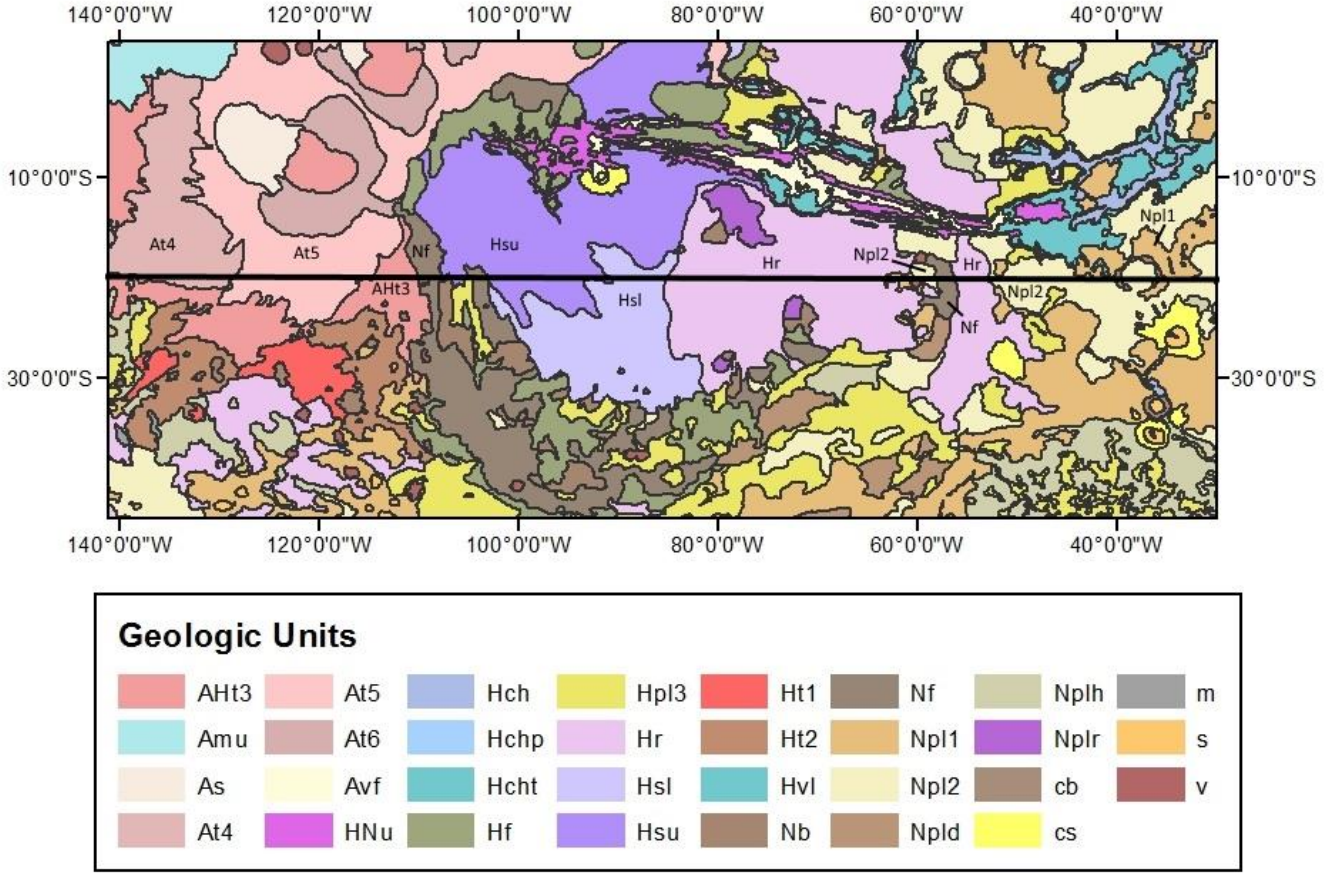

Figure 3.16. Profile high amplitude Tharsis Montes anomaly on 2006 map of geology. The profile shown in Figure 3.15 (black line at 20°S) superimposed on geologic units from Skinner et al. (2006). The units crossed by the profile from left to right are: Amazonian Tharsis Montes Formation members 4 (At4) and 5 (At5), Amazonian/Hesperian (AHt3) Tharsis Montes Formation member 3, Noachian older fractured material (Nf), Hesperian Syria Planum Formation upper member (Hsu) and lower member (Hsl), Hesperian ridged plain materials (Hr), Noachian subdued crater unit (Npl2) and Noachian cratered unit (Npl1).

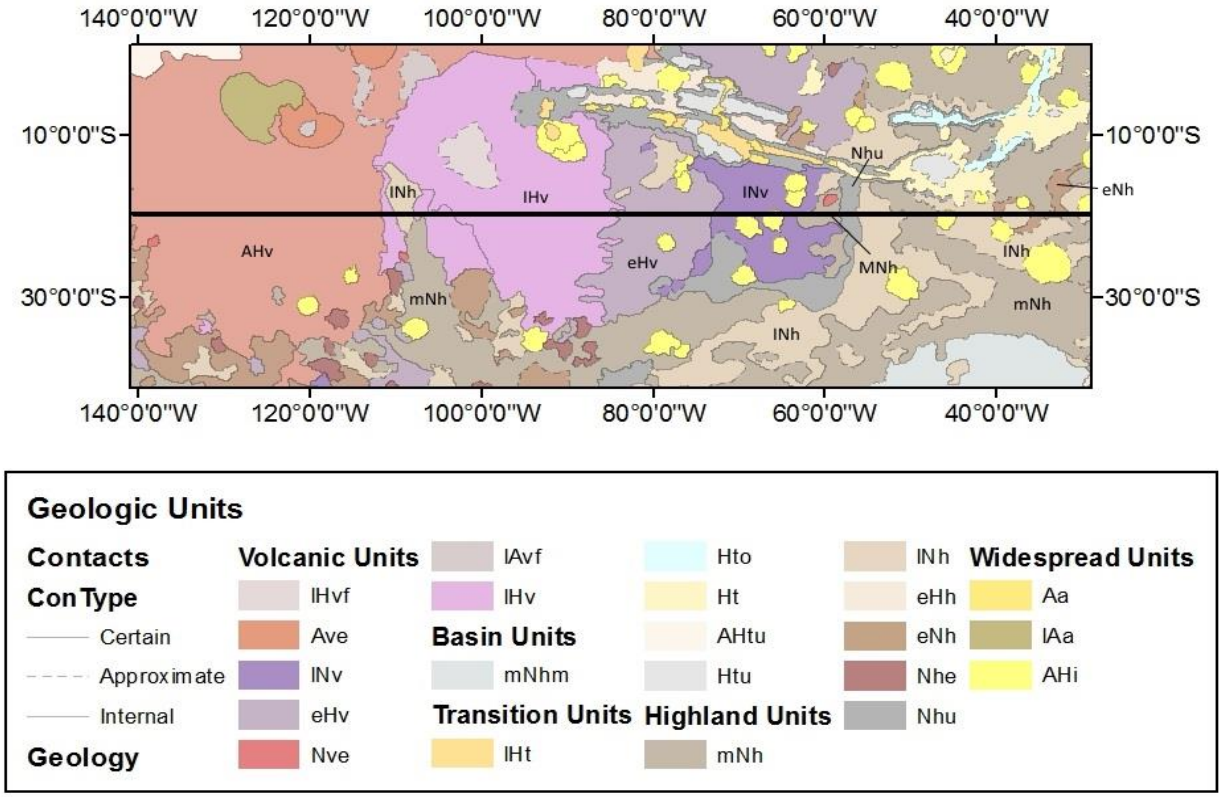

Figure 3.17. Profile high amplitude Tharsis Montes anomaly on 2014 map of geology. Profile from Figures 3.15 and 3.16 superimposed on the 2014 Mars map of geology (Tanaka et al., 2014) The profile crosses units AHv (Amazonian Hesperian volcanics), lHv (late Hesperian volcanics), eHv (early Hesperian volcanics), eHt (early Hesperian transition), lNv (late Noachian volcanics), (mNh) middle Noachian highland, (Nhu) Noachian highland undivided, late Noachian highland (lNh), early Noachian highland (eNh). Units previously classified as A are now considered AH volcanics.

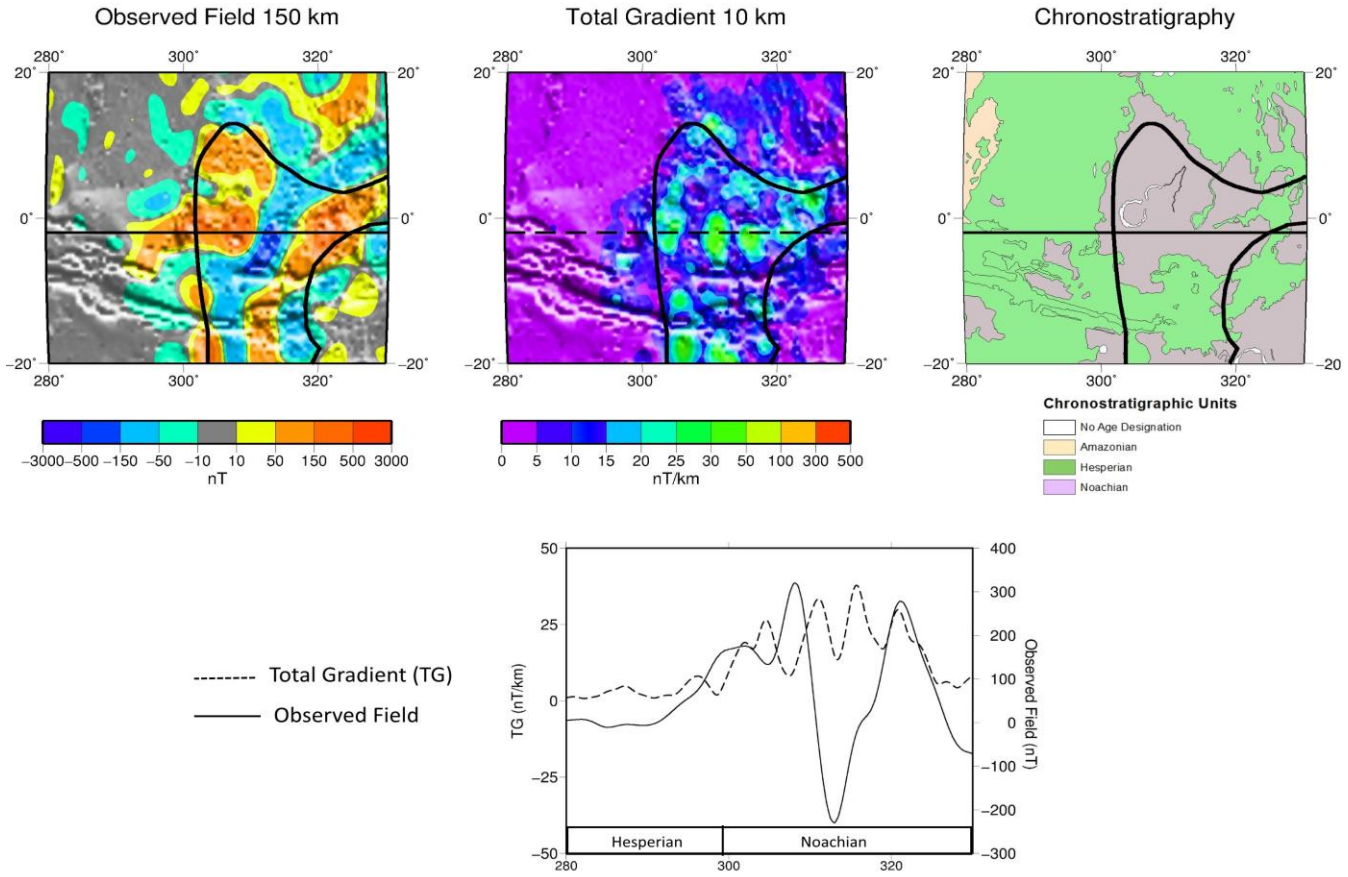

Figure 3.18. High amplitude anomaly with Noachian surface age. A profile (black line at 2°S) through the observed field, TG and chronostratigraphic maps of a magnetic anomaly located under Noachian surface age units just northeast of the profile shown in Figures 3.15, 3.16, and 3.17. Just north of the northern boundary, there is an area of "Hesperian" weak field attributable to the TG tails of Noachian TG sources.

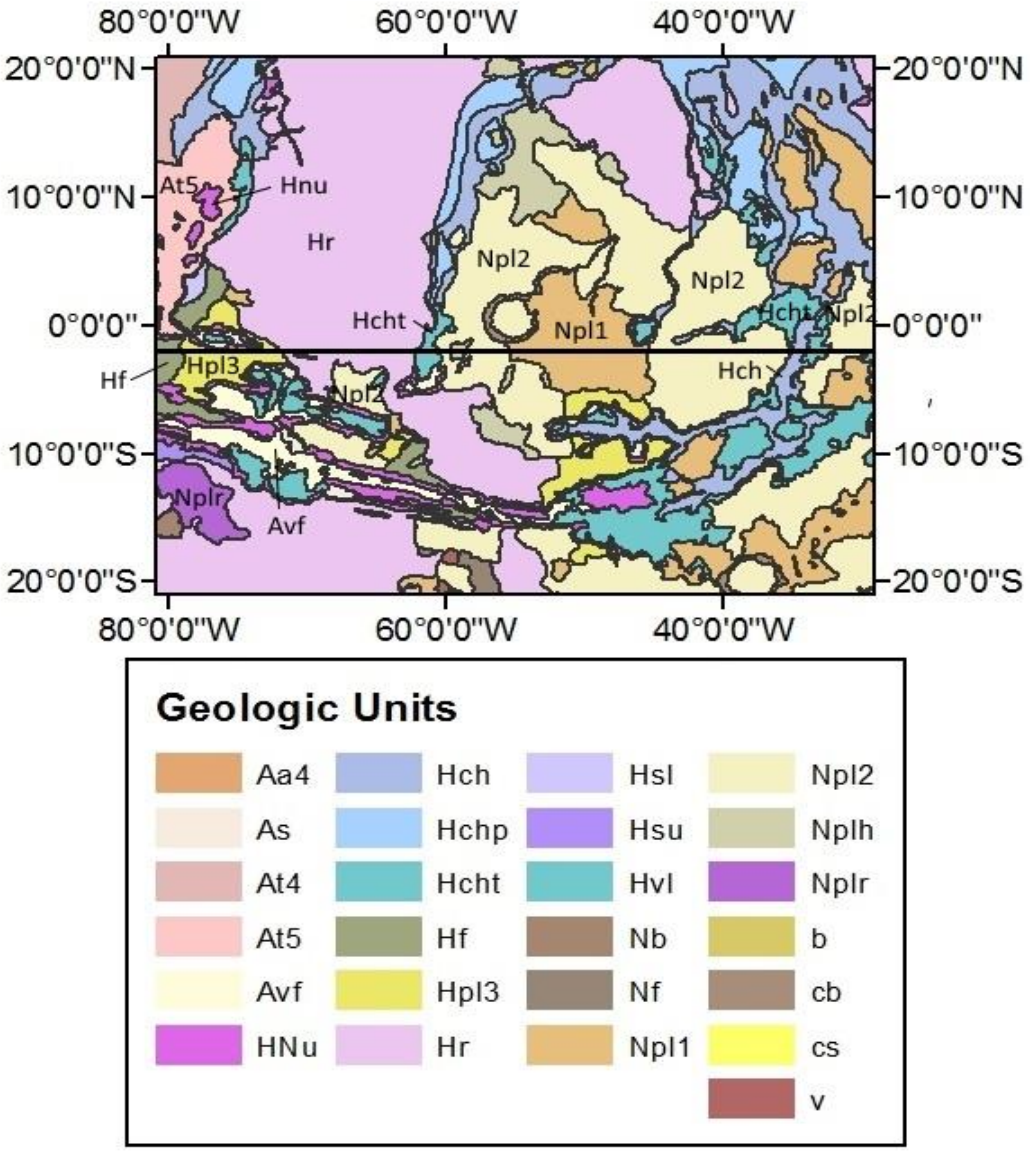

Figure 3.19. Profile high amplitude anomaly with Noachian surface age on 2006 map of geology. Profile shown in Figure 3.18 (black line at 2°S) superimposed on geologic units from Skinner et al. (2006). The units crossed by the profile from left to right are: Hesperian younger fractured material (Hf), Hesperian plateau sequence smooth unit (Hpl3), Hesperian ridged plain materials (Hr), Noachian plateau sequence, subdued cratered unit (Npl2), Noachian plateau sequence cratered unit (Npl1) and highly deformed terrain material, older fractured material (Nf).

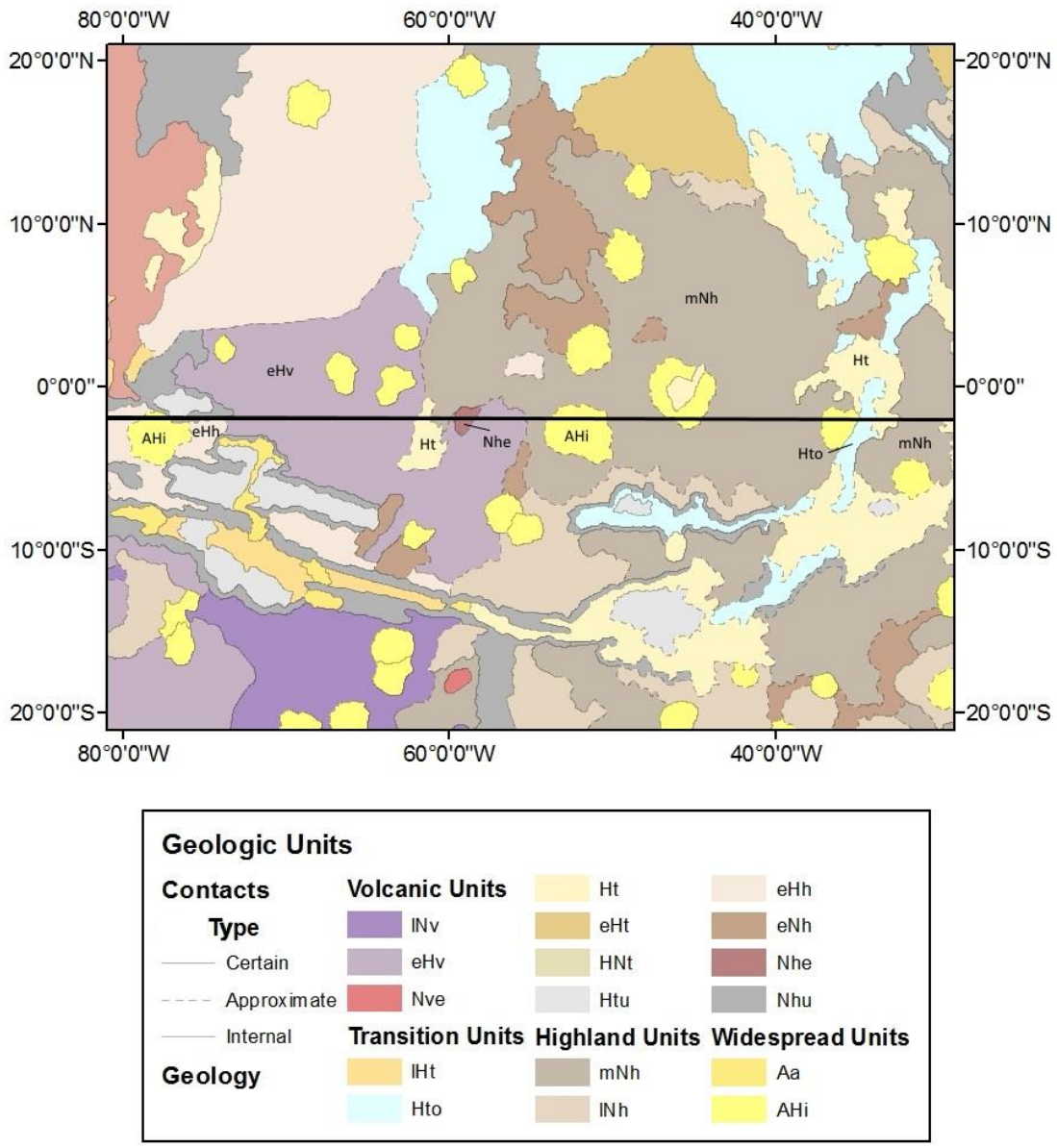

Figure 3.20. Profile high amplitude anomaly with Noachian surface age on 2014 map of geology. Profile from Figures 3.18 and 3.19 superimposed on the 2014 Mars map of geology (Tanaka et al., 2014).The profile crosses units eHh (early Hesperian highland), eHv (early Hesperian volcanics), Ht (Hesperian transition), (mNh) middle Noachian highland.

Chapter 4. Methodology: Paleopoles and Effective Magnetization

Magnetic Edge Effects and Determination of Paleopoles

The main idea behind determining paleopoles from magnetic edge effect anomalies is as follows. Different locations of paleopoles result in different inducing field directions in the vicinity of an edge. Thus, with different paleopoles (called here "test poles"), the resulting magnetic fields from the edges of magnetic sources would be different, and they would correlate differently with the observed fields. The total gradient magnetic field was used to identify the edges of magnetization boundaries (black lines Figure 4.1). TG is invariant of the magnetization direction of 2-dimensional sources and hence acts as a source detector or a source edge detector, depending on the width of the source and the source to observation distance (Ravat, 2011; Figures 3.1 and 3.2; see discussion chapter 3). Figure 4.2 shows an example of the components of the supplied magnetization and the resultant field for a magnetic test dipole at the center of the planet pointing 60°S, 30°E (due to the use of Bz rather than Br) or a test magnetic north at 60°N, 210°E. Figure 4.3 shows the components of the supplied magnetization and resultant field for a test magnetic north at 90°N, 0°E. Comparison of the plots for the resultant fields for test magnetic north at 60°N, 210°E with those at 90°N, 0°E shows how the fields at different edges are different (even though the poles are only 30° away from each other) and would produce different correlation with the observed field. Similarity between the observed field and the field computed from the test pole that best reproduces the observed edge effect field should lead to the identification of a potential paleopole (see for example the Hellas edge in Figures 4.1 to 4.4). Correlation coefficients between observed and calculated fields determined over data windows (in red Figure 4.1) covering the edge segments, for a global distribution of test poles, can be useful in

identifying potential paleopoles. Correlation coefficients measure the degree of similarity, linear relationship, or phase difference between two signals (i.e. observed and calculated fields).

The total gradient field shows that many of the magnetic features (>5 nT/km in Figure 4.1) on Mars are enclosed in an east-west band near the present-day equator (with the exception of the strong anomalies of Terra Cimmeria/Terra Sirenum in the Southern Highlands extending from 150°E to 240°E). The northern boundary of this band corresponds to the crustal dichotomy boundary, regions of impact demagnetization associated with giant impacts (e.g., Isidis), and the boundaries of thermal demagnetization associated with Tharsis. The southern magnetization boundary of this band is demarcated by Hellas and Argyre impact demagnetization areas and the southern edge of Terra Cimmeria/Terra Sirenum high amplitude fields. In places where there are no clear physiographic or geophysical reasons for demarcating boundaries of this band of magnetization, the highs of the TG field which arise from magnetization edges are used (Ravat, 2011). Additional boundaries with different combinations of these above criteria were also considered and tested (see Appendix 2).

To determine paleopoles that magnetized the boundaries, 14 edge segments were considered on the basis of physiographic or geophysical reasons and changes in the direction of the edges. Twenty-nine test pole locations were distributed at approximately 30° spacing using equal area polar tessellation (Katanforoush and Shahshahani, 2000). The global magnetic fields were modeled at 150 km altitude by magnetizing only the region between the two boundaries with dipole moments according to inducing fields created by areocentric dipoles consistent with the test “paleo” (North) poles.

Magnetic fields at 150 km were computed at locations distributed on a sphere using 0.5° (~30 km at the equator) spacing equal area tessellation of Katanforoush and Shahshahani (2000) (polar_tesselate.m developed by Ravat, D and Ditty, M, 2013). In order to compute the magnetization inclination and declination, at the desired pole orientation, polar_tesselate.m calls a function rotateToNorthPole (Comer, MATLAB®, personal communication, 2013). The output of polar_tesselate.m is supplied to remove_in_polygon.m (developed by Ravat, D and Ditty, M, 2013) to select the appropriate points contained within the boundaries shown in Figure 4.1 (additional alternative boundaries tested are shown in Figure A2.1). The output of this program is the input to dbcomp.f (modified from Purucker et al., 2000) in which equivalent dipole moments are computed and converted into magnetization of a volume of equal area spherical prisms of dimensions 0.5°x0.5° (in surface area) x 40 km (thickness). The output of dbcomp.f is the input to Sphharmonics_driver1_final.m (developed by Ravat, D. and Ditty, M., 2013) which utilizes spherical harmonic functions (Plattner and Simons, 2014) and filters out the residual magnetic signal beyond 120 degrees (primarily to avoid high degree and order noise that may be present in the model of Langlais et al., 2000). It is the result of this process that is shown in Figure 4.2 for one test magnetic north paleopole. For each data window shown in Figure 4.1, parameters of least squares linear regression (slope and intercept) and correlation coefficients are computed between the observed and calculated magnetic field components at 0.5° spacing to be used in corr_spatial_2d_xcor_tess.m, developed by Ravat, D. 2013. The magnetic source edge locations could be inaccurate by a few degrees and that could reduce the goodness of fit or the correlation coefficient. To counter the effect of the mis-picked boundaries,

program corr_spatial_2d_xcor_tess.m presently shifts computed fields by up to 2° at 0.5° intervals in latitude and longitude (i.e., 25 computations of correlation coefficients) and picks the highest absolute correlation coefficient. The correlation coefficient method was tested by using the idealized case of a known calculated field (90°N, 0°E) versus the other calculated fields and the test showed that the correlation coefficient was 1.0 for the calculated field with the paleopole of (90°N, 0°E) and it degraded as the test poles got farther away.

Correlation coefficients were computed between the observed and modeled fields from the entire data window over each of the 14 segments. Meaningful correlation coefficients in such analysis tend to be low because the observed fields include the effects of all magnetic features within the data window, whereas the computed fields are only from the magnetization edges (Figures 4.2 and 4.3; see also Milbury and Schubert, 2010). As an example, two paleopoles with the highest correlation coefficients for the data window over Segment 13 have correlation coefficients -0.37 (paleopole at 15°S,165°E) and -0.35 (paleopole at 45°S, 180°E shown in Figure 4.4); the two paleopoles are geographically close to each other and produce similar results in profile comparisons. The profile comparison of edge effects is less satisfactory for other test poles of only slightly lower correlation coefficients. The negative correlation coefficient indicates a reversed core field (magnetic north in the geographic south).

In this analysis, in addition to determining relative correlation coefficients separately for each edge segment (instead of the entire boundary as in Milbury and Schubert, 2010), it proved important to examine profiles, shapes and locations of magnetic features across the edges (see Figure 4.4 and several examples of edges shown

later). This relative quantitative and visual qualitative comparison of anomaly field profiles made it possible to distinguish between high and low quality correlation coefficients. For several edge segments, acceptable pole locations are geographically close to each other (meaning they cluster in the same region of Mars), an expectation which gives validity to the results. For edge segments 9, 11, and 13 the poles are geographically close (Table 4.1). Some of the paleopoles, however, are different than this group of paleopoles and suggest that a few of the magnetization edge boundaries may have been formed under the influence of different magnetic dipole orientations (resulting in different paleopole locations; Table 4.1).

Effective Magnetization of the Edges

The global magnetic fields were modeled at 150 km altitude by magnetizing only the region between the two boundaries with dipole moments according to inducing fields created by twenty-nine areocentric test "paleo" (North) dipoles distributed at 30°. Then the dipole moments were equated to a volume of 0.5°x0.5° equal area by 40 km thick prisms (dbcomp.f). Matching the amplitudes of the dipole produced anomalies with the spherical prism produced anomalies gives the equivalent magnetization. The amplitude differences between the observed and computed fields at this point are caused purely by magnetization differences. To derive the equivalent magnetization at the edges, the computed field amplitudes are adjusted to match the amplitude of the observed field. This was done in two steps, first using the least-squares slopes derived for each window and then a fine adjustment for the particular region of the profile. The result of these operations is called effective magnetization because it is normalized with respect to 40 km thick prisms.

Thus, magnetization yielding the edge effect anomaly of similar amplitude and shape to the observed edge effect field gives an estimate of the effective magnetization of the edge. For the edge of Segment 1 (Figure 4.1), for a 50,000 nT inducing paleo-field and 40 km thick crust of uniform magnetization, the effective susceptibility (at the time of induction of the sources – presented for readers more familiar with susceptibility values on Earth) is 0.1325 to 0.1764 SI units and its equivalent magnetization is 5.2 to 7 A/m. For Segment 13, on the northeast edge of Hellas (Figure 4.1), these values are approximately 0.0662 SI units and 2.63 A/m, respectively. For Segment 2 (Figure 4.1), the north-south edge east of Tharsis, the effective magnetization is 10.53 A/m in the north for an effective susceptibility of 0.2647 SI units (see Table 4.2 for all high quality results for the best boundary set).

Figure 4.4 shows an example of the above process for segment 13. Segment 13 is located on the northeast edge of the Hellas impact basin. There are three representative profiles for this region. For all the profiles, the edge appears only once and thus the edge effect appears only once. Sometimes, the modeled edge is not in the exact location and so the red arrow on the figure suggests the shift needed in the location of the edge. The magnetic edge boundary on Profile A needs to be moved southward, whereas on Profile C it needs to be moved northward.

Although it is impossible to attribute the determined paleopoles with absolute certainty to a particular time period, based on Figure 4.4, 4.5, and 4.6 for segment 13 the edge effects lie primarily in early Noachian units. Figure 4.5 shows a significant area of Amazonian terrain along the edge, but the new map from Tanaka et al. (2014) in Figure 4.6 shows this area has been re-designated as Hesperian or Hesperian/Noachian.

Therefore it is likely that the best paleopoles determined by correlation coefficients and visual analysis (15°S, 165°E; 45°S, 180°E) for this region represent early Noachian paleopoles during a period of reversal as indicated by the negative correlation coefficients (magnetic north pole located in geographic south). This is the straightest and simplest edge as well and one of the best-resolved poles in the present analysis.

Segment 1 is contained within a complex region (Figures 4.7, 4.8 and 4.9). This edge is located along the northeast trending edge of Arabia Terra east of Tharsis and contains several outflow channels (Ares Vallis, Tiu Valles and Simud Vallis) that at one time flowed north into Chryse Planitia (also contained within window 1). The segment has good edge anomalies along the TG edge where it coincides with the crustal dichotomy boundary (Figure 4.7). The edge in profile A (Figures 4.8 and 4.9) is located in the early Hesperian transition (eHt) and in profile B is located in Amazonian/Hesperian volcanics (AHv), both of which are close to the Hesperian/Noachian transition unit (HNt). The edge crosses profile C two times in the west at the contact between HNt and eHt and in the east at the contact of HNt and AHv. Therefore it is likely that the best paleopoles determined by correlation coefficients and visual analysis (15°S, 285°E; 0°, 292.5°E) for this region represent an average of late Noachian to early Hesperian age.

Segment 2 (Figure 4.10) is the north-south edge east of Tharsis located west of segment 1. This region (window 2) contains Lunae Planum which is the transition between the Tharsis rise and the northern lowland plains. It also contains part of Vallis Marinaris including Candor and Coprates Chasma as well as Ganges and Eos Chasma. In Figure 4.10, the edge along A-A' could be move slightly east and along C-C' to the northwest. The correlation coefficients for window 2 reflect a period of normal polarity.

The best fit paleopole is 75°N, 300°E (Table 4.1). This pole agrees well with the pole, 58.3°N, 318.9°E determined by Frawley and Taylor (2004). There is good correlation with a couple of features for the window particularly in the north, but there are interfering anomaly features as well in the central portion of the window from 5°S to 25°S latitude (Figure 4.10). Dividing this segment into 3 separate windows would be beneficial so the central portion which contains Vallis Marineris, a possible rift system associated with the Tharsis buldge, (Chapman, 2007) could be modeled separately. Comparing the edge locations on the profiles with the age of the units in Figure 4.11 and 4.12, the northern portion reflects primarily Hesperian ages (eHt/HNt along profile A and eHt/lHt along profile B) and the southern portion reflects a Noachian age (mNh/eNh along profile C). This would be another good reason to subdivide this segment for modeling to keep Hesperian age terrain (along profiles A and B) in one window and Noachian terrain (along Profile C) in another window. It is likely if this segment is subdivided and remodeled, the northern feature of this window would lead to a similar pole to window 1. The central sub-segment located in the region of Vallis Marineris (between 5°S and 25°S), has a distinct positive-negative z-component field dipolar pattern along the edge which indicates that the edge may have been magnetized in a equatorial, horizontal magnetic field. This pole does show a shift to higher latitude similar to the poles determined by Milbury et al. (2012). They found sources close to cratered or volcanic Hesperian units favoring paleopole positions closer to the current rotation axis, which would be consistent with the pole determined for segment 2 (75°N, 300°E). The presently determined pole for the entire window 2, however, cannot be a true pole because the region needs to be subdivided into multiple segments.

Segment 9 is located in Solis Planum, a high elevation volcanic plain south of Valles Marineris and east of Tharsis. Segment 9, shown in Figure 4.13, also needs to be subdivided and remodeled. Profile A (Figures 4.14 and 4.15) is over Hesperian age basinal units (eHb, lHb) surrounded by Noachian age units (volcanics, highlands) and profile B traverses early and middle Noachian highland units (mNh and eNhm). Profile C does not have a distinct edge anomaly (Figure 4.13), but has a few magnetic features overlying early Noachian highlands to early Hesperian volcanics and highland (eNh, eHv and eNhm) as shown in Figure 4.15. Therefore it is likely that the best paleopoles determined by correlation coefficients and visual analysis (45°N, 135°E; 15°N, 135°E) for this region represent an average of early Noachian to early Hesperian paleopoles. One of these poles is low latitude similar to the other poles that are likely to represent Noachian sources, but the other (45°N, 135°E) is higher latitude perhaps due to the Hesperian age terrain reflected in window 9. These poles do agree reasonably well with poles determined by Arkani-Hamed (2001b) 10°N, 162°E, Boutin and Arkani-Hamed (2006) 5°N, 167°E and Hood et al. (2005) 27°N, 192°E and 43°N, 196°E within this region.

Segment 11 (Figure 4.16) is located in Terra Cimmeria and Terra Sirenum which are heavily cratered regions of the southern highlands with very high amplitude magnetic anomalies. The edge effect for segment 11 is best defined along the southern and eastern edges (Figure 4.16). It appears from the map in Figures 4.17 and 4.18 that the polar units in these areas overlie early, middle, and late Noachian highland. Therefore it is likely that the best paleopole determined by correlation coefficients and visual analysis (15°N, 195°E) for this region represents a Noachian paleopole during a period of normal polarity

indicated by positive correlation coefficients (magnetic north pole located in geographic north). Pole 11 is close in proximity to pole 13 (Figure 4.19).

With the exception of Connerney et al. (1999) and Sprenke and Baker (2000) who modeled profiles across long, linear anomalies in Terra Cimmeria and Terra Sirenum, researchers have modeled isolated magnetic sources in order to extract magnetization information. The method presented here, which is also discussed in Ditty and Ravat (2013), is an entirely new method of determining magnetization strength, direction, and paleopole location from magnetic anomalies across the edges of magnetic sources on Mars. The results presented in Table 4.1 and shown in map form in Figure 4.19 imply that some of the paleopoles for different edge segments in the magnetization band considered are located in different parts of the planet. The magnetization of sources along the edges ranges from 2.5 to 11 A/m for a 40 km thick crust for most edges, but it could be as high at 95 A/m in some of the southern highlands (Table 4.2). In conjunction with chronostratigraphic information from magnetized geologic units, the analysis and the paleopoles presented here, and those from other workers, have the potential to provide additional constraints on the true polar wander path of Mars.

Table 4.1. Summary results for edge segments. Some of the well-correlated observed and computed magnetic edge fields. Correlation coefficients are window/sample size dependent; their values among different windows depend on the complexity of the edge segment and non-edge-related magnetic fields. However, the probability of a random sample exceeding any of these correlation coefficients is $<10^{-6}$ (p-value, Bevington and Robinson, 1991). HQ indicates a high quality result using visual comparison of shapes of the observed and computed fields in maps and profiles. For negative correlation coefficients, the pole locations are converted to their respective north areomagnetic pole. Negative values indicate reversed core field. Additional acceptable poles are listed where applicable.

Segment/ Window number	Correlation coefficients for the best poles	Location (latitude, longitude) of the North Areomagnetic Paleopole
1	-0.26 (HQ)	15°S, 285°E 0°, 292.5°E
2	0.36 (HQ)	75°N, 300°E
3	0.33	15°N,165°E
8	0.26	75°N, 300°E
9	0.45 (HQ)	45°N, 135°E 15°N, 135°E
10	0.30	0°N, 22.5°E 0°N, 67.5°E
11	0.48 (HQ)	15°N, 195°E
12	0.25	15°N, 225°E
13	-0.37 (HQ) -0.35 (HQ)	15°S, 165°E 45°S, 180°E

Table 4.2. Summary results of effective magnetization. Effective magnetization and effective susceptibility for the HQ results in Table 4.1.

Segment Number	Corr. Coeff. for best poles	Pole Location (lat., long.)	Effective Magnetization Range (A/m)	Effective Susceptibility Range (SI units) (@ 50000 nT inducing field)
1	-0.26	15°S, 285°E 0°, 292.5°E	7.02	1.76
2	0.36	75°N, 300°E	10.53	0.264
9	0.45	45°N, 135°E 15°N, 135°E	2.63 - 7.02	0.066-0.176
11	0.48	15°N, 195°E	42.13 - 94.79	1.06-2.38
13	-0.37 -0.35	15°S, 165°E 45°S, 180°E	2.63 - 3.51	0.066-0.088

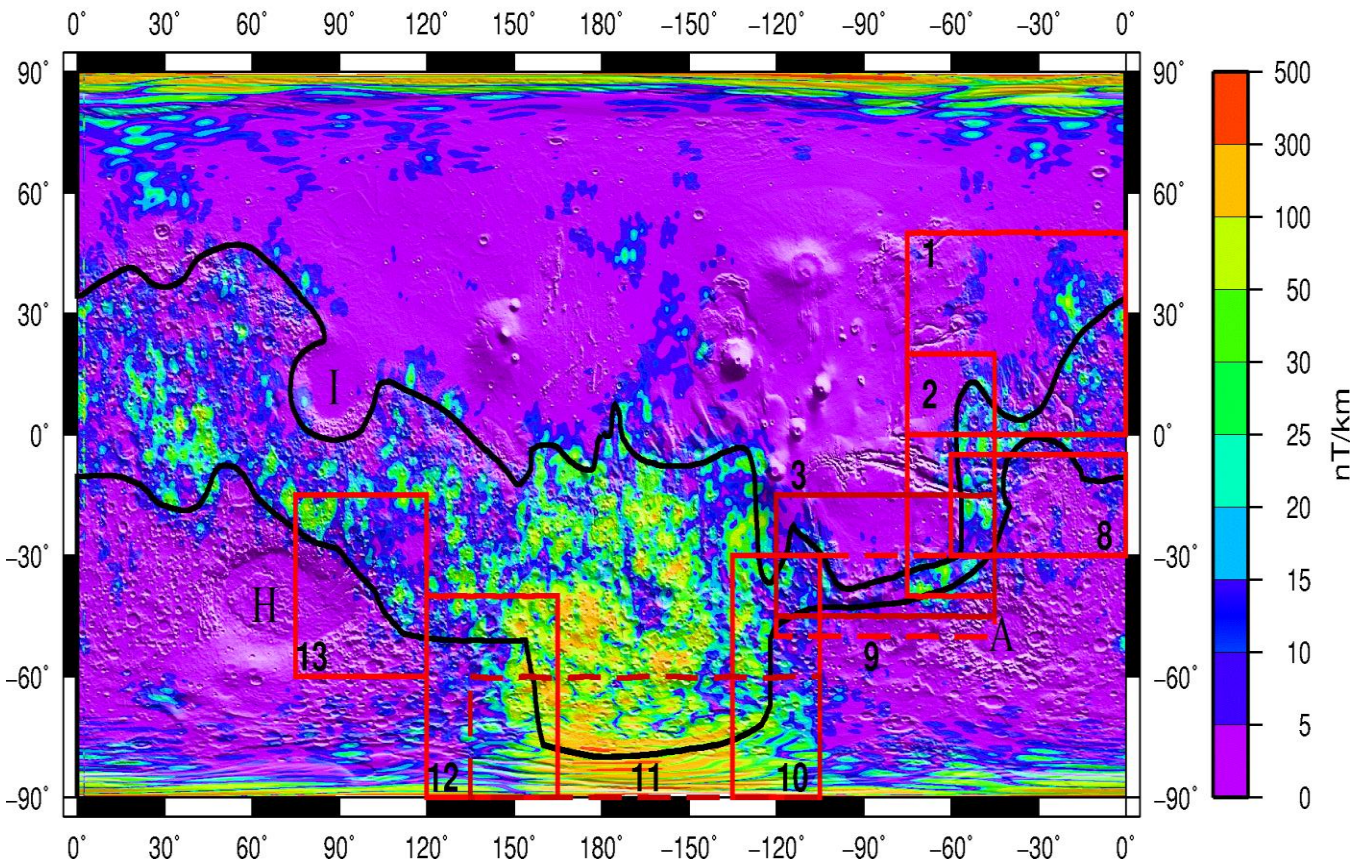

Figure 4.1. Map of TG at 10 km with boundaries and windows. Equidistant Cylindrical global map of TG calculated from the crustal field model of Langlais et al. (2010). Purple regions are largely non-magnetic, whereas the fields >5 nT/km indicate magnetic source regions. Heavy black lines denote magnetization boundaries used in this study. Red boxes and adjacent black numbers are data windows listed in Table 4.1 and 4.2. H, A, I stand for Hellas, Argyre, and Isidis giant impacts, respectively.

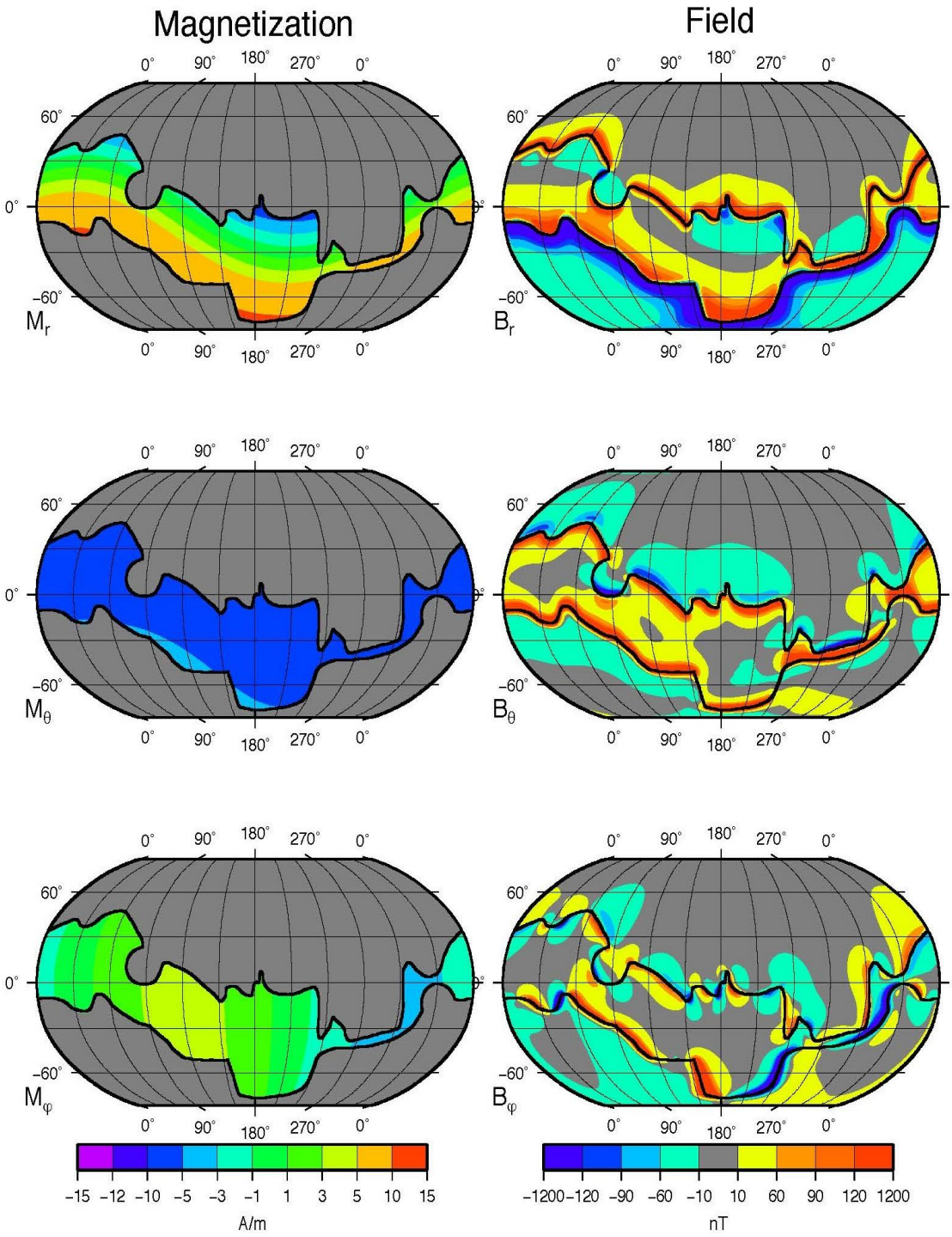

Figure 4.2. Magnetization and resultant field at 150km for a test magnetic north at 60°N, 210°E. The r (top), θ (middle) and φ (bottom) components of the supplied magnetization (left) and the resultant field (right) (see also Milbury and Schubert, 2010). Negative magnetization implies opposite direction of magnetization in the coordinate system.

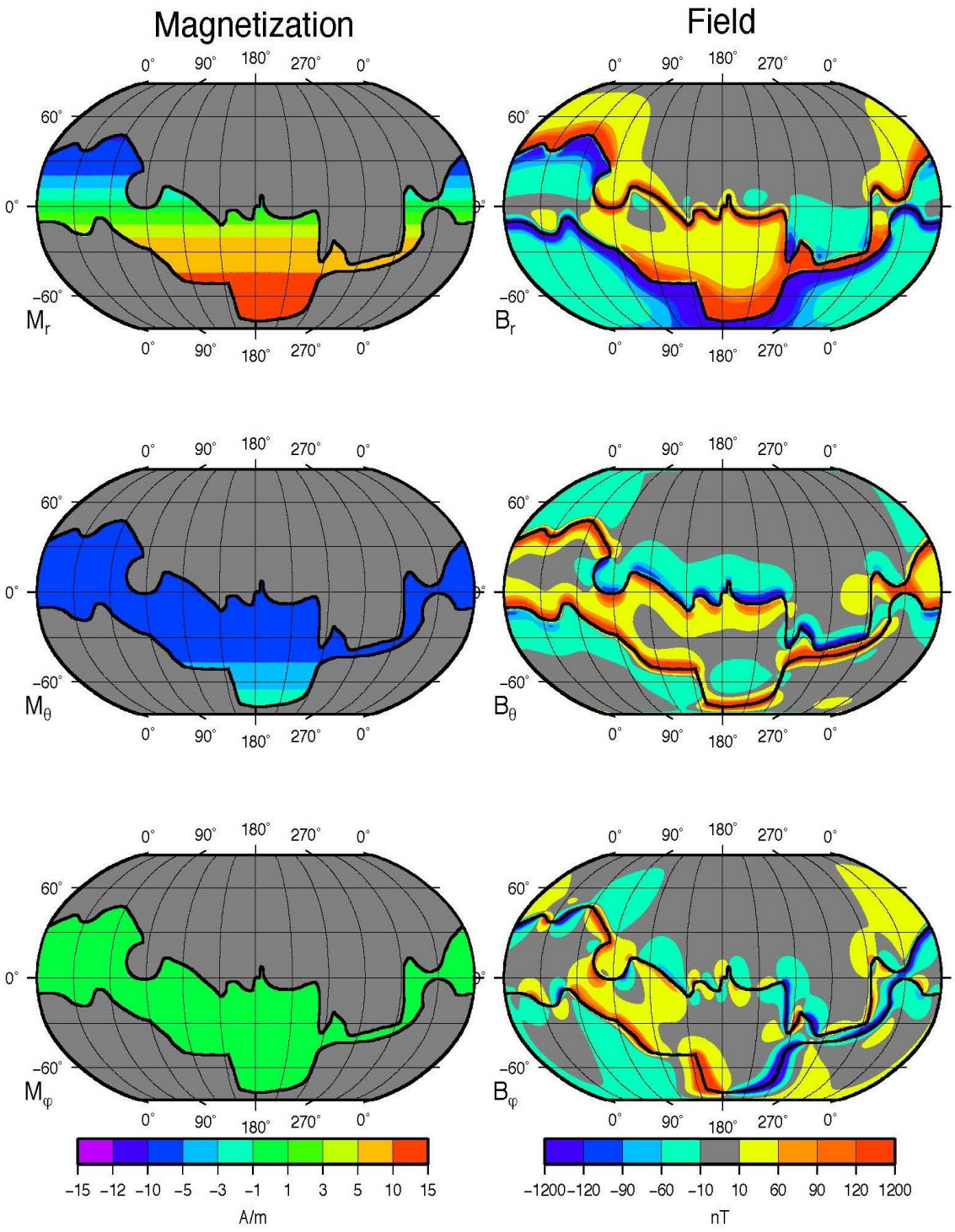

Figure 4.3. Magnetization and resultant field at 150km for a test magnetic north at 90°N, 0°E. The r (top), θ (middle) and φ (bottom) components of the supplied magnetization (left) and the resultant field (right) (see also Milbury and Schubert, 2010).

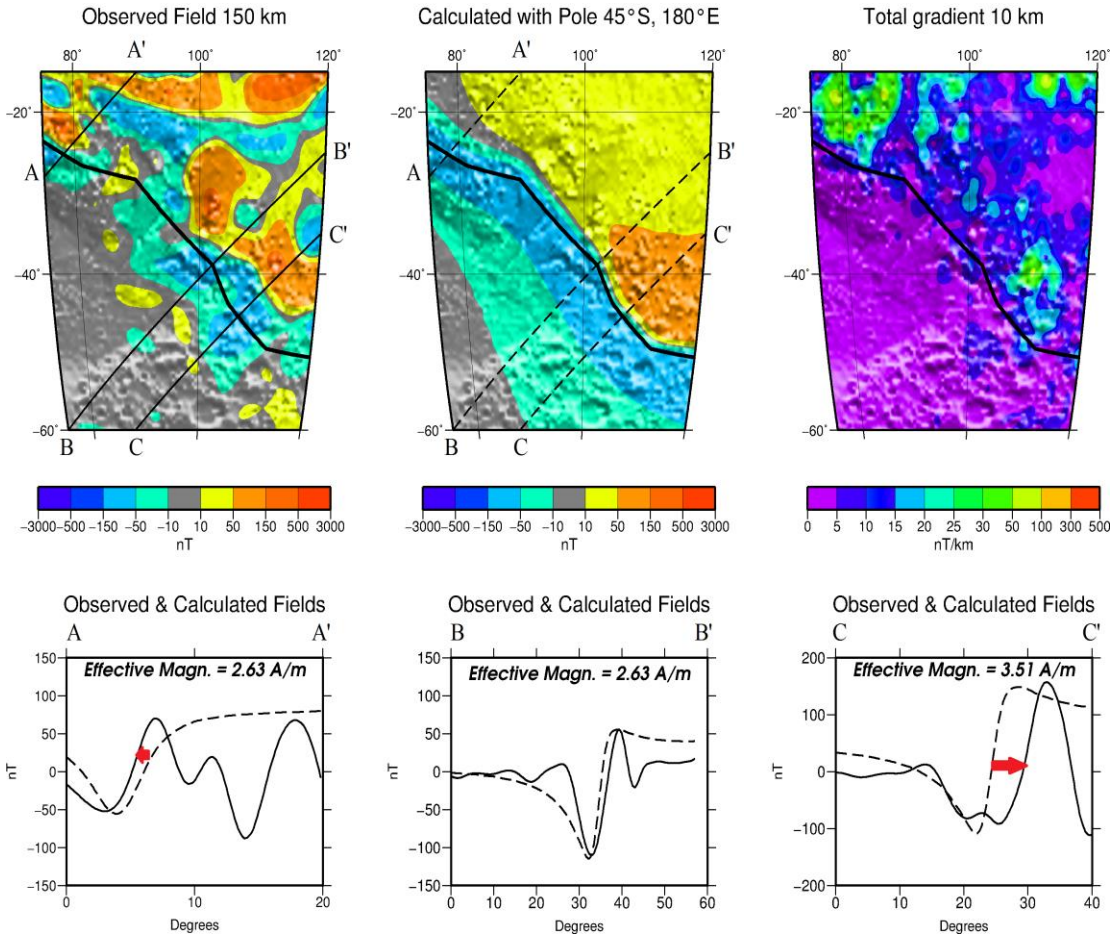

Figure 4.4. Magnetic fields and profiles across Segment/Window 13. Magnetic fields and profiles across the northeast edge of Hellas Planitia (Segment/Window 13 in Table 2). (Top Left) the observed z-component field from Langlais et al. (2010) at 150 km altitude; (Top Center) the calculated field from the test pole at 45°S, 180°E. Heavy black lines are the magnetization boundaries from Figure 4.1. The continuous & dashed lines with labels A-A', B-B', and C-C' represent the profile locations shown in the bottom figures. The red arrow suggests the shift needed in the location of the edge to account for the lateral offset in the fields. Additional magnetic sources are required in the edge region for Profile C-C'.

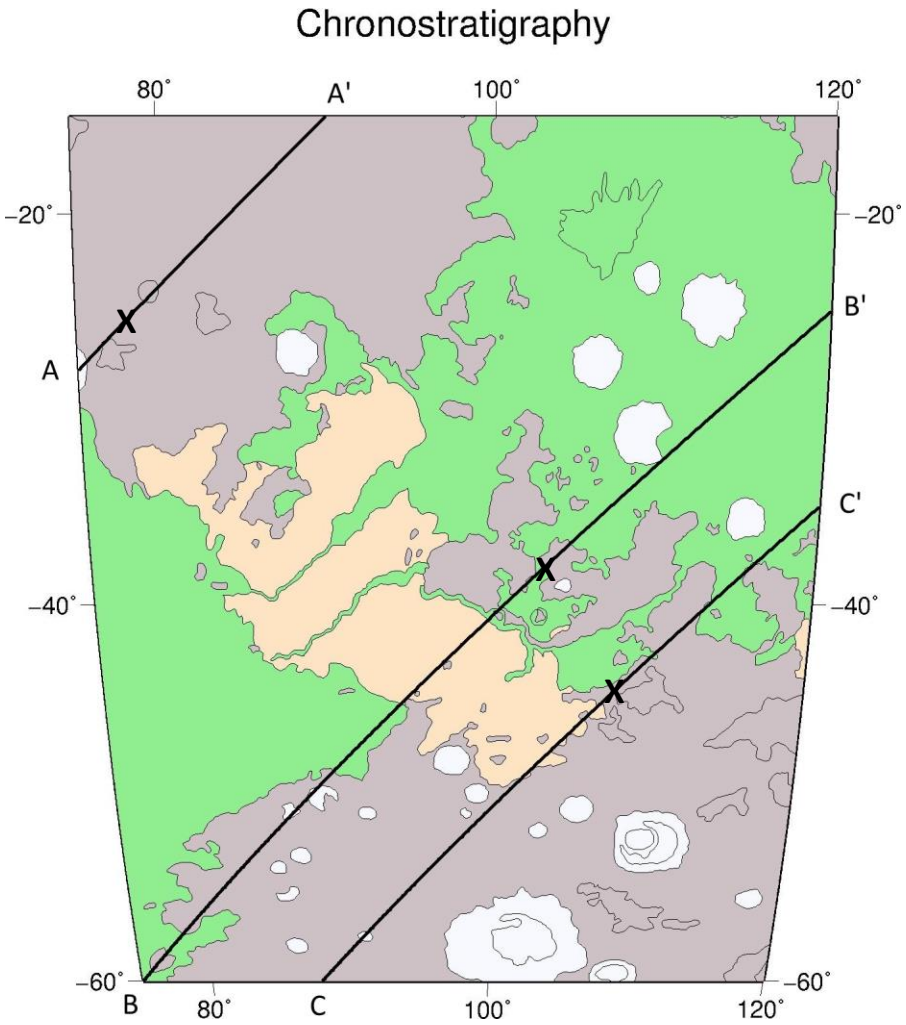

Figure 4.5. Profiles from Segment/Window 13 on 2006 map of chronostratigraphy. Profiles A-A', B-B' and C-C' from Figure 4.4 placed on a map of chronostratigraphy based on Skinner et al. (2006) after Tanaka et al. (1986). Noachian is shown in purple, Hesperian in green and Amazonian in peach. Black X shows the location the TG edge effect on the profiles. The edge effects from profiles A and C lie within the Noachian. The edge effect along profile B falls at the edge of the Noachian and Hesperian.

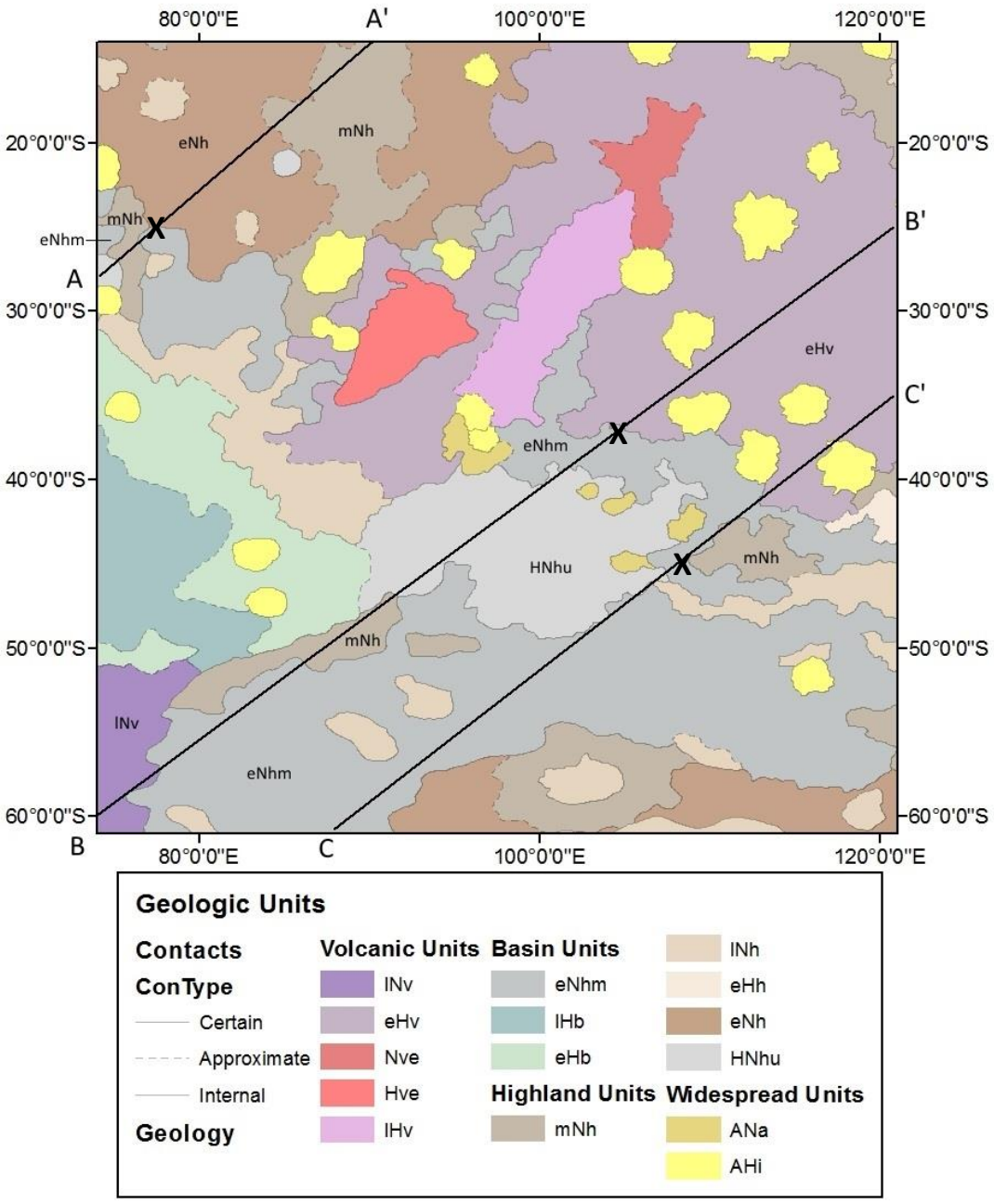

Figure 4.6. Profiles from Segment/Window 13 on 2014 map of geology. Profiles from Figure 4.4 on geology from Tanaka et al. (2014). Profile A crosses early and middle Noachian units, profile B crosses early Noachian to early Hesperian units, and profile C lies mainly in early Noachian units with the northeastern section of the profile in early Hesperian volcanic units. Profile B crosses no Amazonian unit in the 2014 map which is in contrast to profile B in Figure 4.5 from the map of Skinner et al. (2006). Black Xs denote where the edges cross the profiles.

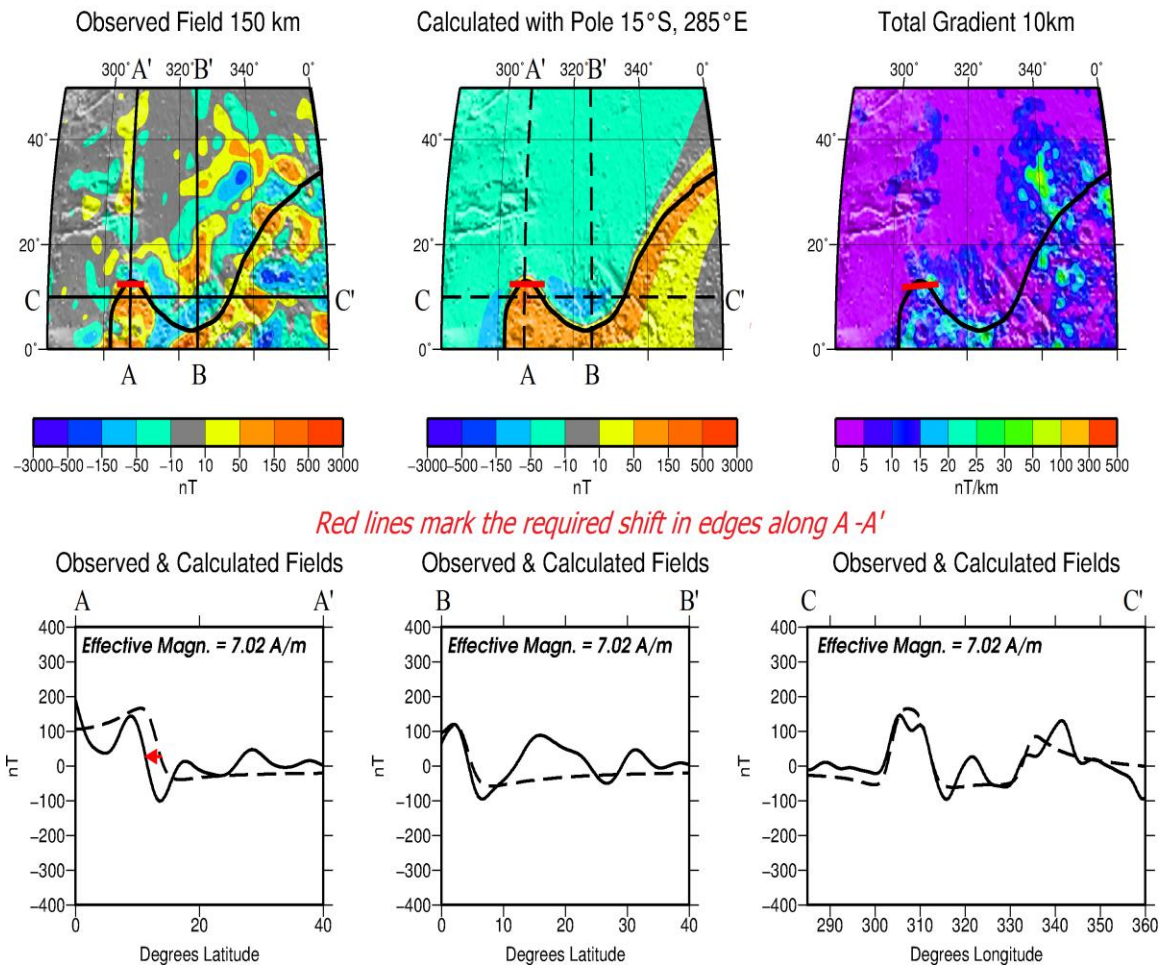

Figure 4.7. Magnetic fields and profiles across Segment/Window 1. Segment 1 is the northeast trending edge along Arabia Terra east of Tharsis. (Top Left) the observed z-component field from Langlais et al. (2010) at 150 km altitude; (Top Center) the calculated field from the test pole at 45°S, 285°E. Heavy black lines are the magnetization boundaries from Figure 4.1. The continuous & dashed lines with labels A-A', B-B', and C-C' represent the profile locations shown in the bottom figures. The red arrow suggests the shift needed in the location of the edge to account for the lateral offset in the fields.

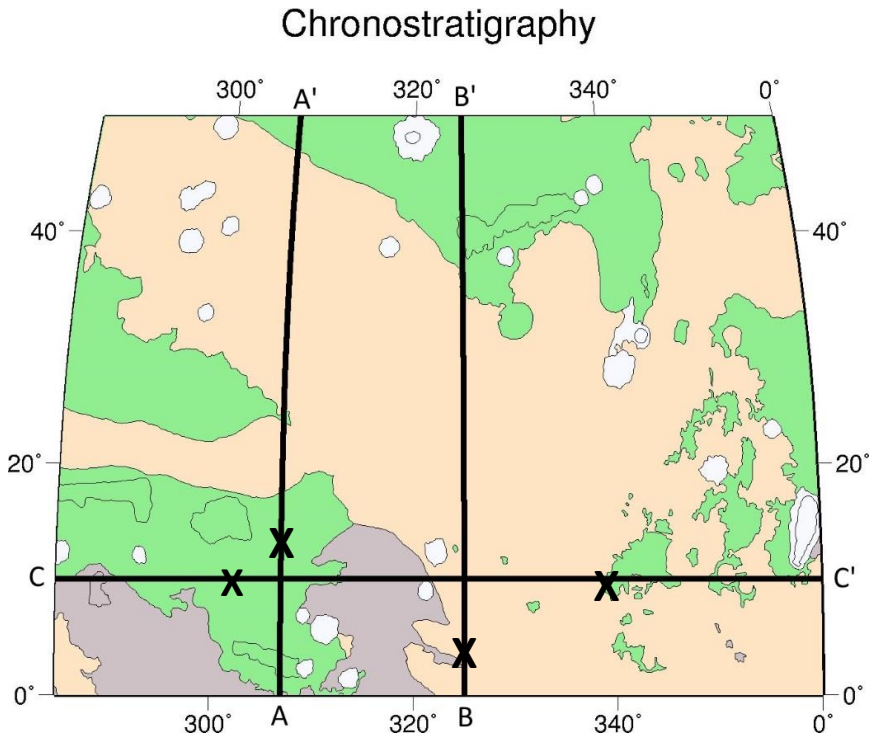

Figure 4.8. Profiles from Segment/Window 1 on 2006 map of chronostratigraphy. Profiles A-A', B-B' and C-C' from Figure 4.7 placed on a map of chronostratigraphy based on Skinner et al. (2006). Noachian is shown in purple, Hesperian in green and Amazonian in peach. The edge effects from profile A lie at the black X in the Hesperian, from profile B at the black X at the contact of the Noachian and Amazonian and from profile C in the Hesperian (western black X) and at the Hesperian/Amazonian contact (eastern black X).

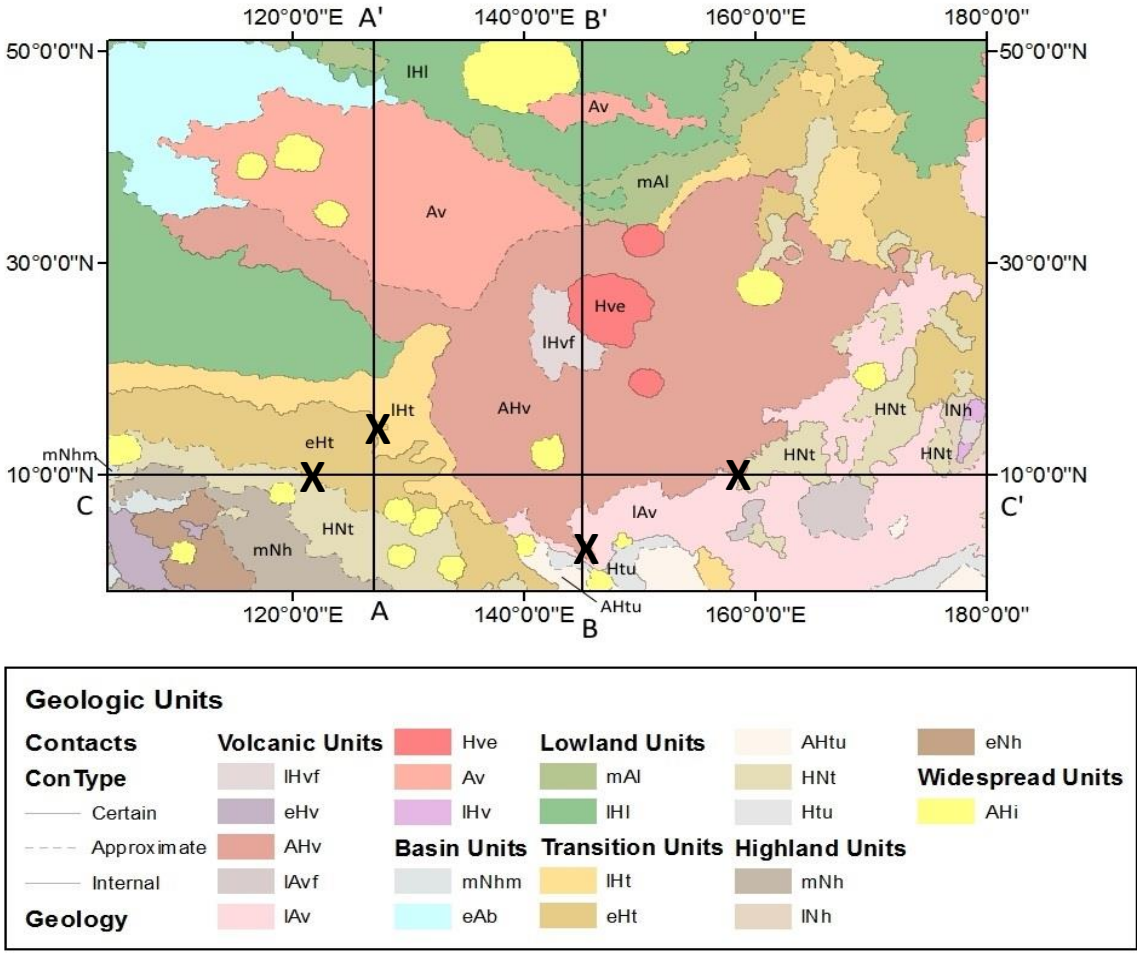

Figure 4.9. Profiles from Segment/Window 1 on 2014 map of geology. Profiles from Figure 4.7 on geology from Tanaka et al. (2014). Profile A crosses middle Noachian highland (mNh), Hesperian/Noachian transition (HNt), early Hesperian/late Hesperian transition (eHt/lHt), Amazonian/Hesperian volcanics (AHv), Amazonian volcanics (Av) into late Hesperian lowland (lHl). The updated units significantly differ from those shown in Figure 4.8, the southern portion is in Noachian and Hesperian/Noachian units and the central portion is shown as Amazonian/Hesperian units instead of the Amazonian unit only. Profile A lies primarily in Noachian and Hesperian units, with the edge located at the contact between eHt and lHt. Profile B crosses units ranging in age from Hesperian to Amazonian with the edge located at AHv and lAv. Profile C crosses units ranging in time from middle Noachian to late Amazonian and the edge crosses twice, in the west at the contact of HNt and eHt and in the east at the contact of HNt and AHv.

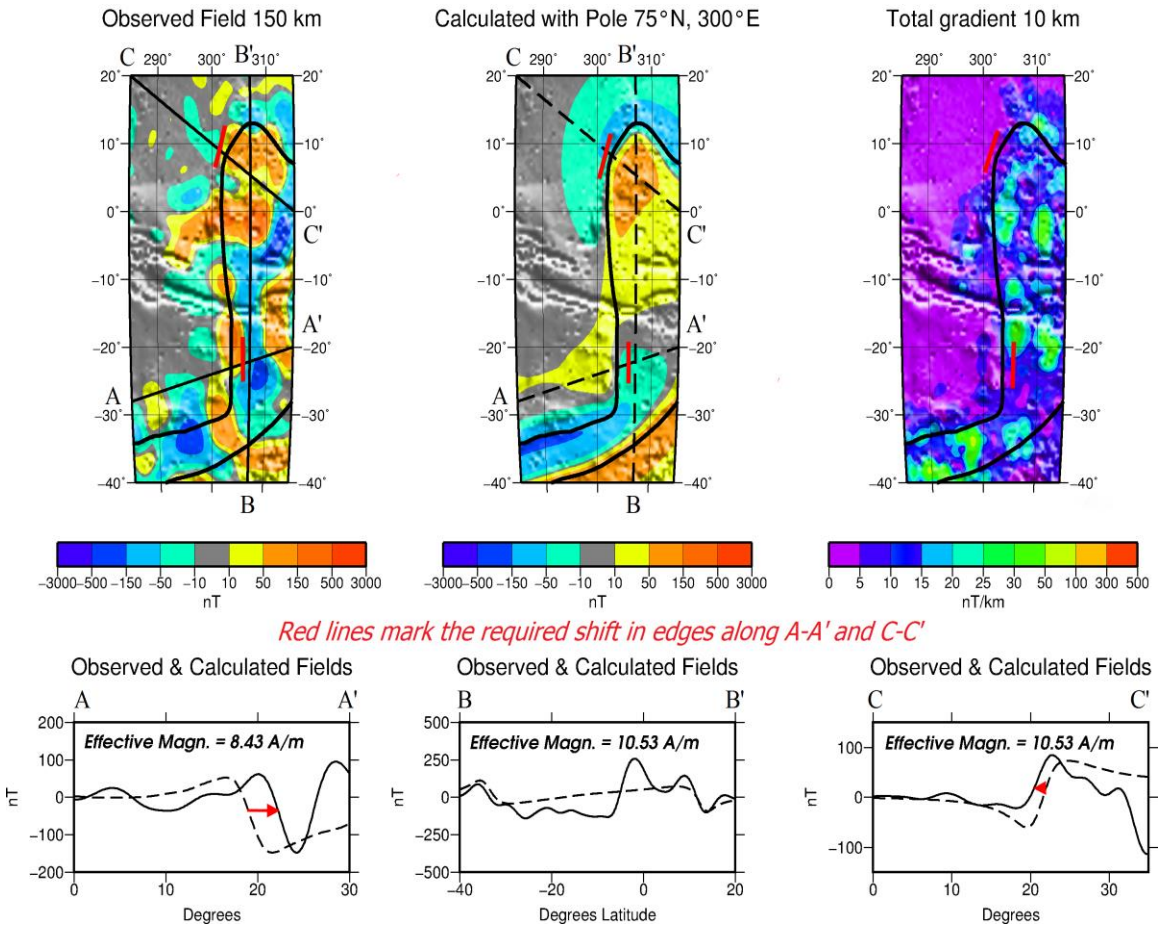

Figure 4.10. Magnetic fields and profiles across Segment/Window 2. Segment 2 is the north-south edge east of Tharsis. The edge along A-A' could be move slightly east and along C-C' to the northwest. (Top Left) the observed z-component field from Langlais et al. (2010) at 150 km altitude; (Top Center) the calculated field from the test pole at 75°N, 300°E. Heavy black lines are the magnetization boundaries from Figure 4.1. The continuous & dashed lines with labels A-A', B-B', and C-C' represent the profile locations shown in the bottom figures. The red arrow suggests the shift needed in the location of the edge to account for the lateral offset in the fields.

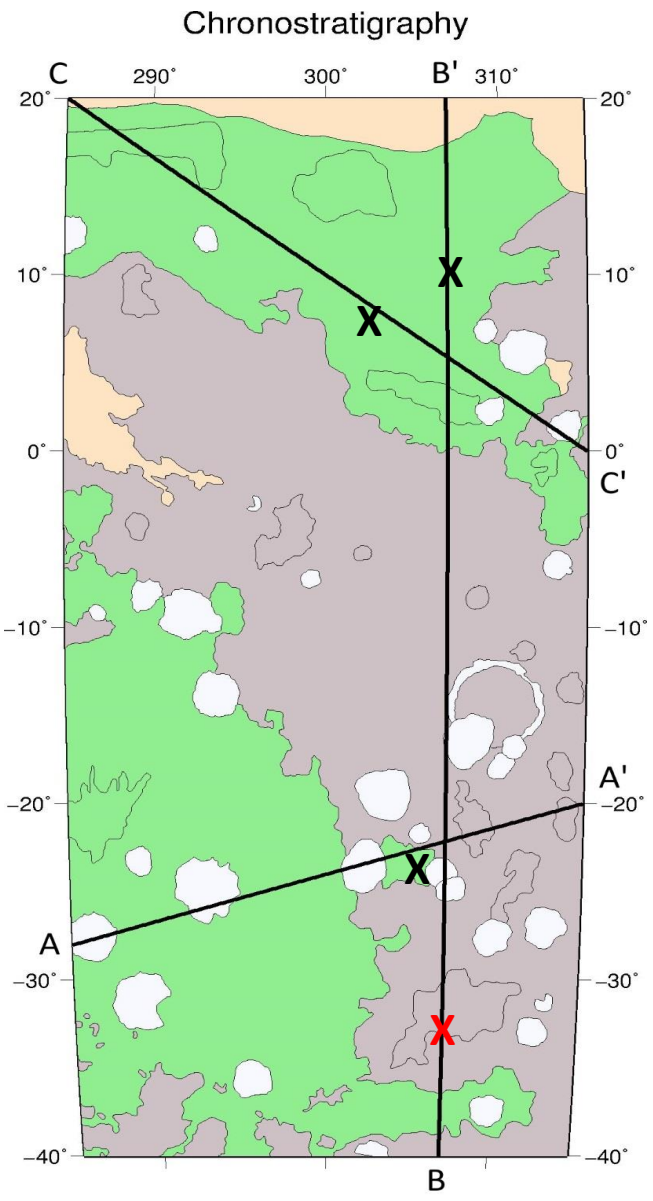

Figure 4.11. Profiles from Segment/Window 2 on 2006 map of chronostratigraphy. Segment 2 profiles A-A', B-B' and C-C' from Figure 4.10 placed on a map of chronostratigraphy based on Skinner et al. (2006). Noachian is shown in purple, Hesperian in green, Amazonian in peach and undesignated units in white. The edge effect along profile A lies at the black X at a contact between the Hesperian and Noachian. Profile B has two edge effects, one at the black X above 10°N in the Hesperian and one at the red X below 30°S in the Noachian. The edge effect for profile C is located just below 10°N in the Noachian.

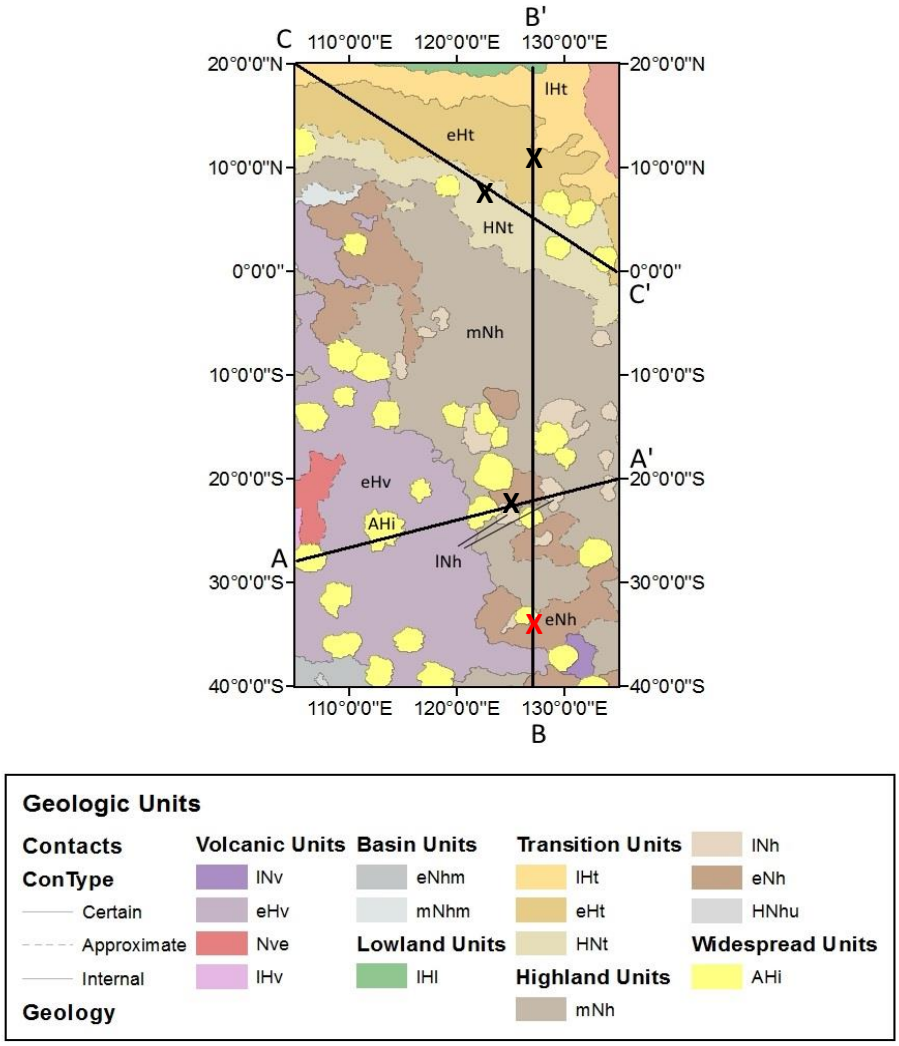

Figure 4.12. Profiles from Segment/Window 2 on 2014 map of geology. Profiles from Figure 4.10 on geology from Tanaka et al. (2014). Profile A crosses early Hesperian volcanics (eHv), early Noachian highland (eNh) and middle Noachian highland (mNh). The edge effect for profile A is located Noachian only (black X) while Figure 4.11 shows the edge effect at the contact of a Hesperian unit and the Noachian. Profile B crosses from south to north, eHv, eNh, mNh, Hesperian/Noachian transition (HNt), early Hesperian transition (eHt) and late Hesperian transition (lHt). The southern edge effect along profile B lies at the contact of eNh and mNh (red X) and the northern edge effect at the contact between eHt and lHt. Profile C crosses lHt, eHt and HNt. The edge effect (black X) is located close to the contact between eHt and HNt. In Figure 4.11 the entire C-C' profile is in only the Hesperian unit.

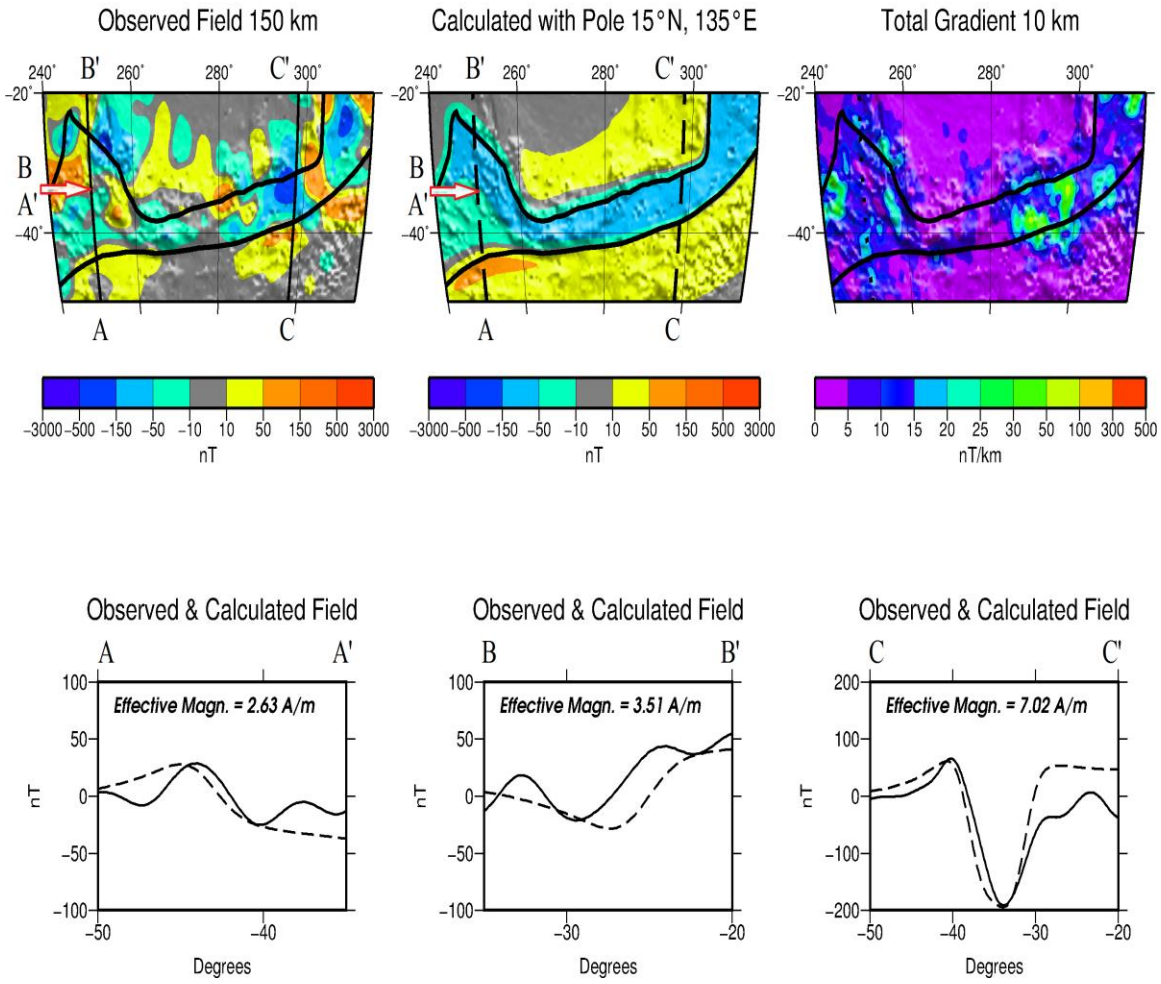

Figure 4.13. Magnetic fields and profiles across Segment/Window 9. Segment 9 contains the both the northern and southern boundaries (thick black lines) trending east/west located south of Tharsis. The westernmost profile is split into A-A' that covers the southern boundary and B-B' that covers the northern boundary. The location dividing A-A' and B-B' is indicated by the red arrow.

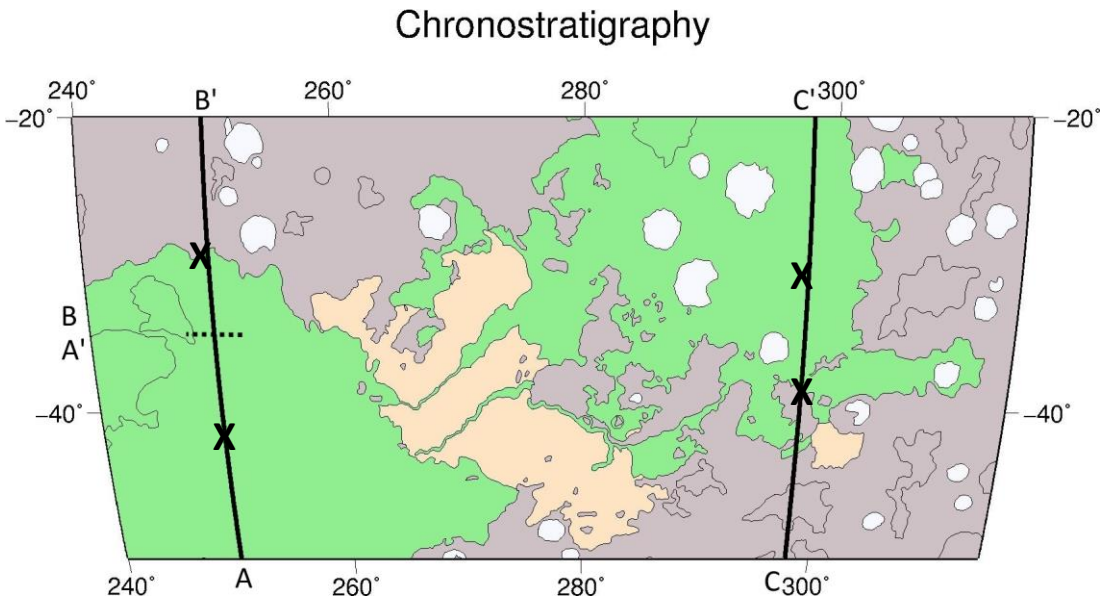

Figure 4.14. Profiles from Segment/Window 9 on 2006 map of chronostratigraphy. Segment 9 profiles A-A', B-B' and C-C' from Figure 4.13 are placed on a map of chronostratigraphy based on Skinner et al. (2006). Noachian is shown in purple, Hesperian in green, Amazonian in peach and undesignated units in white. The black dashed line indicates the division between Profile A-A' and Profile B-B'. The edge effect along Profile A lies at the black X located in the Hesperian. Profile B edge effect is located at the black X at the contact of the Hesperian and Noachian. There are two TG field edge effects located on profile C, one at the black X above 40°S at the contact of the Hesperian and Noachian and another in the Hesperian at approximately 30°S.

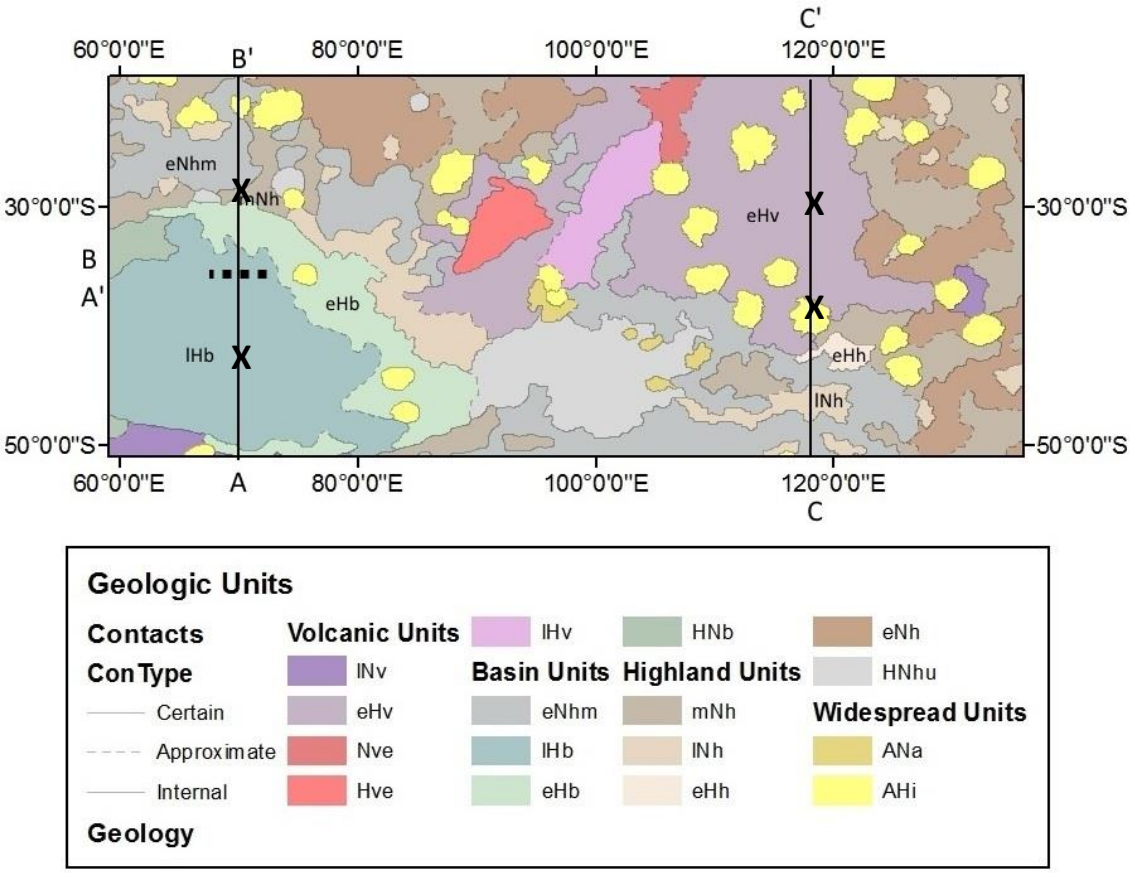

Figure 4.15. Profiles from Segment/Window 9 on 2014 map of geology. Profiles from Figure 4.13 (segment 9) on geology from Tanaka et al. (2014). Profile A crosses early Hesperian basin (eHb) and late Hesperian basin (lHb). Profile B crosses middle Noachian highland (mNh) and early Noachian highland massif (eNhm). Profile C crosses eNhm, late Noachian highland (lNh), early Hesperian highland (eHh) and early Hesperian volcanics (eHv). The TG field edge effect for Profile A is located in lHb (black X) and, for Profile B, it is located in proximity to eHb, mNh and eNhm. Profile C has two edges, the southern edge is located close to the contact between eHv mNh and the northern edge is located in eHv.

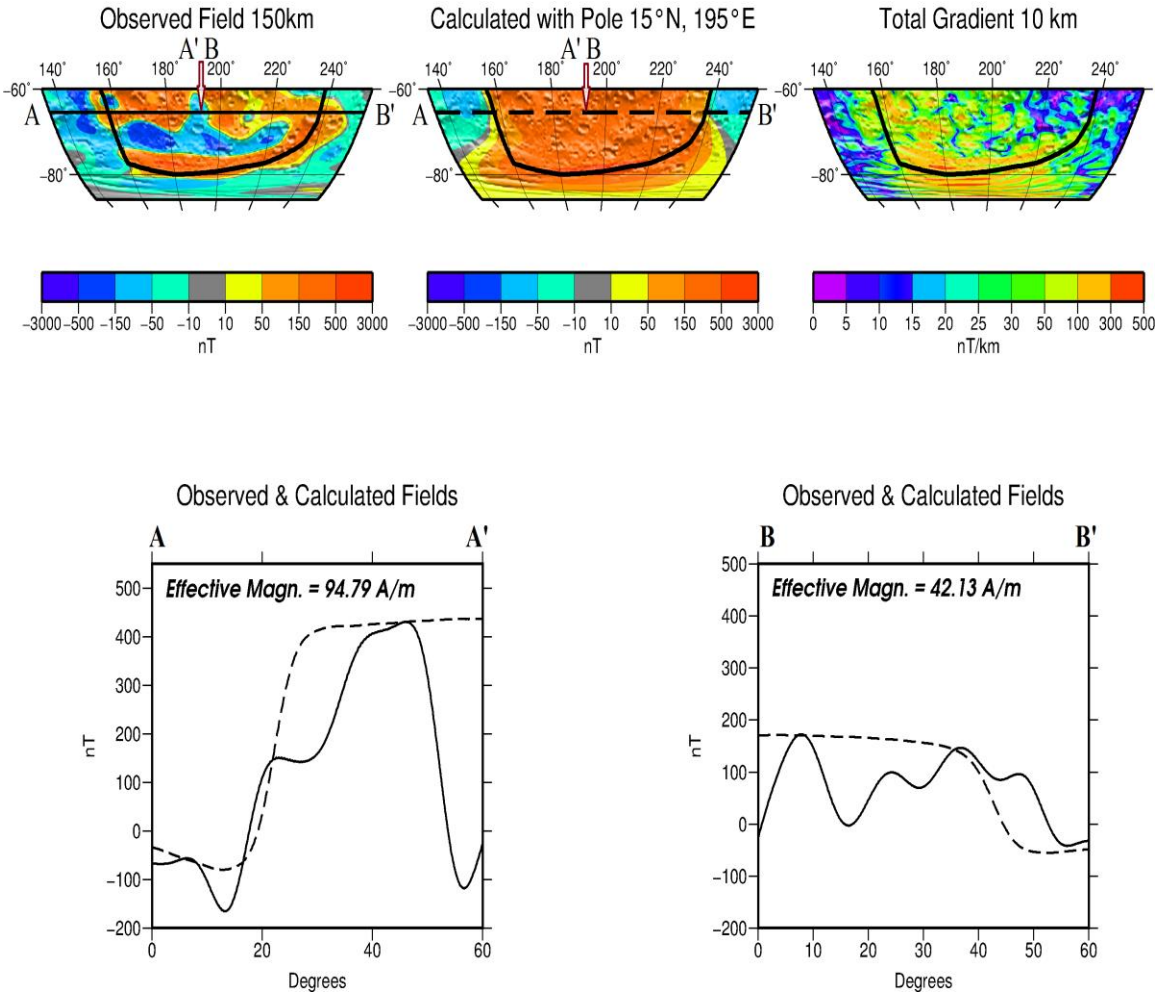

Figure 4.16. Magnetic fields and profiles across Segment/Window 11. Segment 11 contains the southern boundary located in the Terra Cimmeria and Terra Sirenum area. The east/west trending profile is split into A-A' (across the western edge of the boundary) and B-B' (across the eastern edge of the boundary). The edges analyzed here are not optimum as there are several coalescing anomaly features in those regions and no clear 2D edge. The best correlation is on the southern E-W oriented boundary.

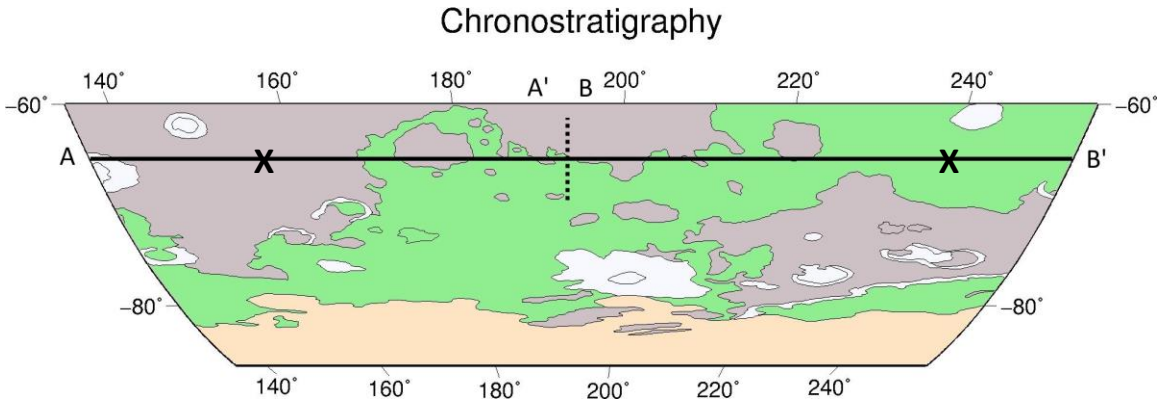

Figure 4.17. Profiles from Segment/Window 11 on 2006 map of chronostratigraphy. Segment 11 profiles A-A' and B-B' from Figure 4.16 are placed on a map of chronostratigraphy based on Skinner et al. (2006). Noachian is shown in purple, Hesperian in green, Amazonian in peach and undesignated units in white. The black dashed line indicates the division between Profile A-A' and Profile B-B'. The TG field edge effect along Profile A lies at the black X in the Noachian. Profile B edge effect is located at the black X in the Hesperian.

.

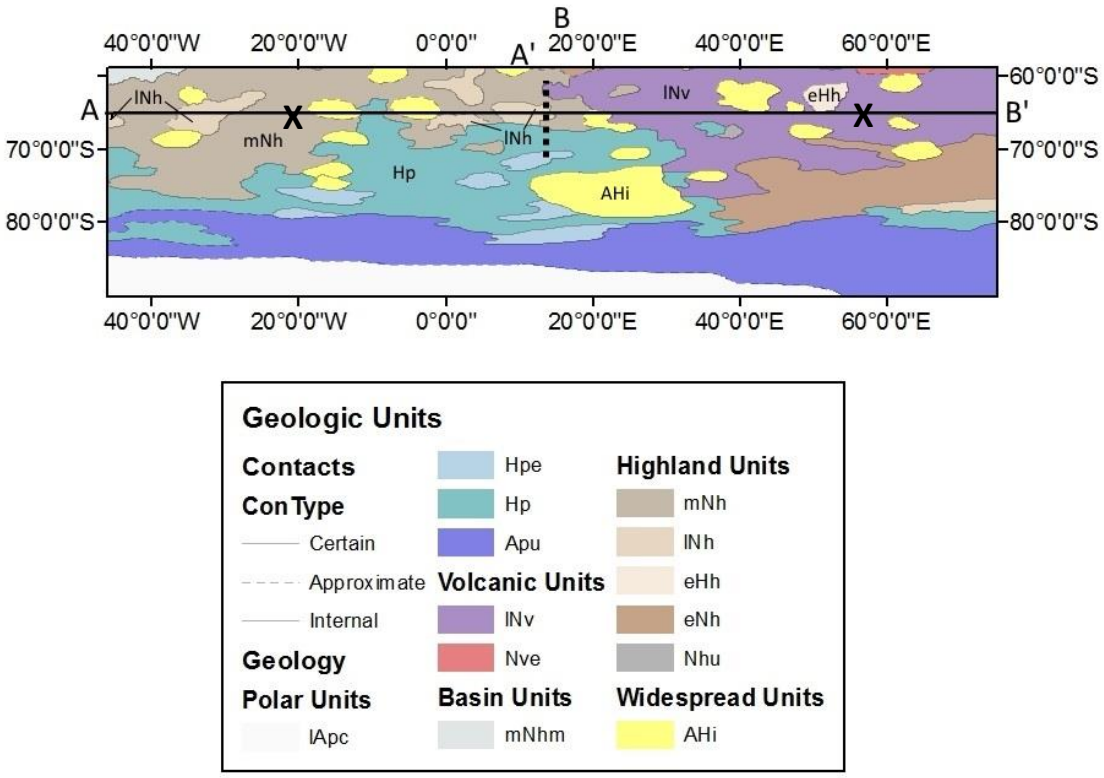

Figure 4.18. Profiles from Segment/Window 11 on 2014 map of geology. Profiles from Figure 4.16 shown on geology from Tanaka et al. (2014). Profile A crosses late Noachian highland (lNh), middle Noachian highland (mNh) and Hesperian polar (Hp) from west to east. Profile B crosses mNh and late Noachian volcanics (lNv) from west to east. Black X's denote location of the edge effect.

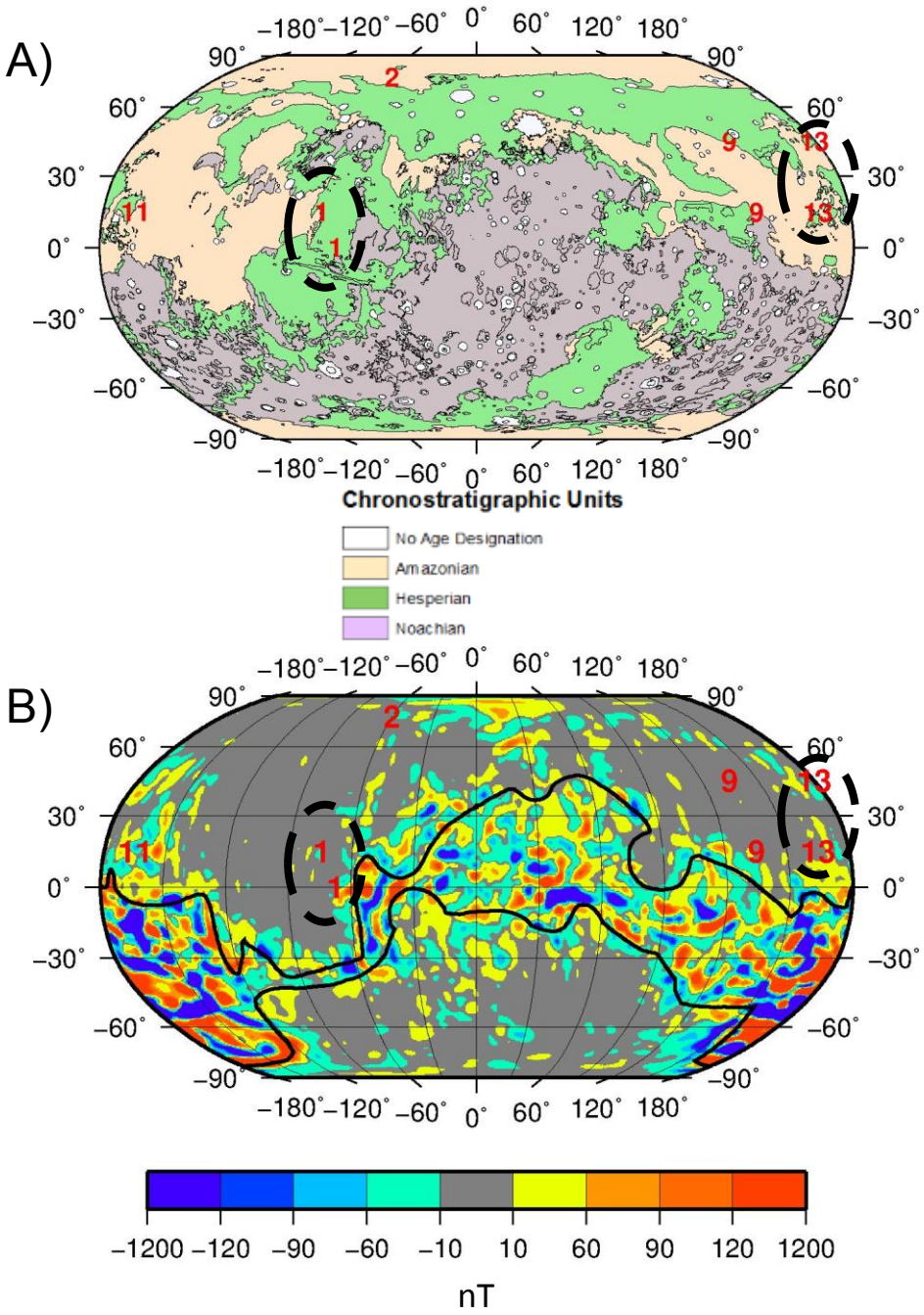

Figure 4.19. A) Map of high quality poles on chronostratigraphy. Amazonian, Hesperian and Noachian chronostratigraphic units in Robinson projection. Red numbers reflect the north test pole location for the highest quality correlation by the associated window numbers (black dashed ovals contain south test pole locations). B) Map of high quality poles on z-component. The z-component at 150 km showing the location of the highest quality north test pole locations by associated window number (in red). Black ovals contain south test pole locations.

Chapter 5. Discussion

This study, with several important modifications, builds upon the study of Milbury and Schubert (2010) for determining paleopoles using magnetic boundaries and for determining the timing of the dynamo using comparison of magnetic field with geologic age units. One key modification of this study is the use of higher spherical harmonic order magnetic field features to permit defining of the magnetic boundary based on magnetic features. Milbury and Schubert (2010) used low spherical harmonic degrees (up to degree 7) of the magnetic field from the entire crustal dichotomy boundary on Mars (see boundary Figure 5.1) to determine an average paleopole for the entire boundary. The Mars magnetic field power spectrum shows that the power in low degrees is small (as opposed to that of Earth) because there is no core field, whereas the power in higher degrees is larger for Mars. Milbury and Schubert use up to degree 7 which contains only long wavelength fields that are spread out over a large area. The edge effects of interest for paleopole correlation also produce short wavelength, high amplitude anomalies and this information is not utilized by Milbury and Schubert (2010).

The dichotomy boundary reflects several different age terrains and those different age terrains may have formed under different orientations of the dynamo (multiple paleopoles) if progressive true polar wander occurred during the dynamo episodes. To capture these details in the analysis, it is important to consider smaller edge segments according to physiographic features as well as ages of terrains across the boundary segment. There are also many magnetic field features that go beyond the dichotomy boundary into the lowlands and therefore it is judicious to use magnetic features in delineating the magnetic boundary. Thus, in this study, in addition to the crustal

dichotomy boundary, the total gradient (TG) field, which was shown earlier to be magnetization direction invariant across two-dimensional magnetic features, was used in determining the magnetic boundary. For the southern edge (making up the central band of magnetization), there are no dichotomy features (unless edges of Hellas and Argyre large impacts are considered), the magnetic boundary is based on TG features and connecting lines enclosing the Terra Cimmeria/Terra Sirenum magnetic features. Higher resolution in locating the boundary was further achieved by downward continuation of the TG field to 10 km altitude. The TG field was not noisy because of mean square noise reduction and the other reasons mentioned in Chapter 3.

The second key difference from Milbury and Schubert is the use of TG field and ArcGIS methods to examine which age regions have magnetization features. Milbury and Shubert also use the radial component of the magnetic field (Br) that has features with greater skewness at non-vertical magnetization directions. Even in locations where magnetization is restricted to one lithology/age region, the Br component from that magnetization could transgress into neighboring age units and thus lead to incorrect magnetization-age relationships causing problems in inferring the timing of the dynamo episodes. In addition, polar units (Api and Apl) likely underlain by Noachian terrain were not considered by Milbury and Shubert.

The results presented in Table 4.1 and 4.2 show that some of the paleopoles for different edge segments in the magnetization band considered are located in different parts of the planet. This suggests different orientations of the inducing core field dipole. In addition, it appears that the poles from edge segments have recorded both normal and reversed directions of the core dipole. In conjunction with chronostratigraphic

information from magnetized geologic units, the analysis and methods in this research have the potential to provide additional constraints on the true polar wander path of Mars. While Milbury and Schubert (2010) provided a global average paleopole, the paleopoles derived in this study represent averages across smaller boundary segments and the windows of comparison were also chosen taking into account Tharsis demagnetized regions across Noachian age segments (see Figure 5.2).

Table 3.1 shows the area of magnetization is highest for the Noachian regions and decreases into the Hesperian and Amazonian regions. It also shows that the strongest fields are associated with the Noachian and to a lesser extent the Hesperian and weaker fields with the Amazonian unit. The few isolated strong TG anomalies found within the Amazonian unit (≥25nT/km) were mapped and examined in profile (Figure 3.12 and 3.15) and were conjectured to be associated with underlying Noachian units within Amazonian volcanic terrain because there are Noachian inliers in the younger terrain. In addition, the updated map in Figure 5.3, by Tanaka and others (2014) shows sizable areas that were previously designated as Amazonian (A) are now given the designations Amazonian/Noachian (AN) and Amazonian/Hesperian (AH). The strong TG anomalies over regions previously classified as Amazonian fall in these re-designated regions. The change in designation from A to AN or AH would only further increase the percentage of TG anomalies that are present in Noachian and Hesperian units.

In magnetized regions of differing age units, the possibility of thin and non-magnetic Amazonian or Hesperian cover rocks (either sedimentary or volcanic), underlain by magnetic Noachian rocks must be considered. While using TG field helps with this issue because it is inherently reflective of more near surface sources than deep

ones (gradient fields suppress longer wavelengths from deeper sources) it cannot completely remove the problem of magnetization of deeper sources (see Figure 3.2b). Examination of Figure 3.10B shows there are a few (≥15nT/km) Hesperian volcanic areas that are likely to carry Hesperian age magnetism. Milbury et al. (2012) found Hesperian sources within Hesperian volcanic units near Syrtis Major that favored paleopoles that were high latitude (close to the rotation pole).

Figure 5.4 was taken from Milbury et al. (2012) and shows all the best-fit paleopoles for magnetic sources modeled for Syrtis Major and Figure 5.5 shows all the best-fit paleopoles for magnetic sources modeled for Tyrrhenus Mons (presently called Tyrrhena Terra/Hesperia Planum). Figure 5.6 (also from Milbury et al., 2012) shows the location of the modeled magnetic sources superimposed on geologic units (diamonds for Syrtis Major sources and stars for Tyrrhenus Mons sources). Milbury and others (2012) concluded that paleopoles clustered in 2 groups by latitude, an equatorial group and a high latitude group close to the current rotation axis. Noachian cratered units produced low latitude poles and Hesperian cratered or volcanic units produced high latitude poles. Despite there being some correlation in latitude of paleopoles based on proximity to either Noachian or Hesperian units, Milbury et al. (2012) results still show significant scatter in pole locations as seen in Figures 5.4 and 5.5.

Milbury and others (2012) assumed magmatic magnetic anomalies were entirely due to magnetization of solidified magma beneath a volcanic edifice and that the surface age would correspond to the age of magmatism and thus the age of acquisition of magnetization. They used gravity anomalies to help target intrusion sites assuming the magmatic intrusion sites should have a lateral contrast in density with the surrounding

country rock. Syrtis major was active during the Hesperian and Milbury further assumes the associated weaker magnetization is attributable to Hesperian magmatism rather than to underlying units (Noachian).

Figure 2.1 from Milbury et al. (2012) shows that scatter is also seen in poles from other researchers. This figure has paleopoles determined from isolated anomalies. Hood et al. (2005) determined a mean paleopole of 202°E, 34°N based on modeling 7 dipolar anomalies spread across the planet and 2 additional strong east-west trending anomalies in the south, Arkani-Hamed and Boutin (2004) modeled 9 anomalies and found a mean paleopole centered at 232°E, 22°E, Sprenke (2005) used statistical analysis to determine a pole of 230°E, 46°N, Langlais and Purucker (2007) modeled anomalies associated with Apollinaris Patera and found a high latitude pole at 99°E, 88°N, Quesnel et al. (2007) modeled 3 anomalies near Newton crater and determined 3 poles (310°E, 26°N; 299°E, 46°N; 221°E, 44°N). A comprehensive list (taken from Milbury et al., 2012) of paleopoles by author is provided in Table 2.1 along with source location and parameters used for modeling.

These above mentioned poles are the mean of a set of poles calculated for isolated magnetic anomalies. These methods require assumptions about the direction of magnetization, while the use of TG to locate edge sources in this study does not require these assumptions (at least for the long straight edge segments). In addition, the data used for these studies is not the same for all researchers. This study uses the z-component at 150 km from the model of Langlais et al. (2010) based on MGS MAG and ER data. Other studies use different sets of data, modeling, and methodologies (for a detailed list of data and methods by author see Tables 2.1 and 5.1-5.6). The methods outlined in this

study take into account a much larger area than the studies mentioned above, so spread in paleopoles is not surprising. Even so, the mean pole (34°N, 202°E) determined by Hood et al. (2005) and the mean pole (22°N, 232°E) determined by Arkani-Hamed and Boutin (2004) is relatively close to the poles determined for windows 11 (15°N, 195°E) and 12 (15°N, 225°E). For the purpose of comparison, it is more meaningful to look at the individual poles (determined by other authors) by anomaly location versus the window in which the modeled anomalies are located (Tables 5.1 to 5.6)

Magnetization yielding the edge effect anomaly of similar amplitude and shape to the observed edge effect field gives an estimate of the effective magnetization of the edge. The effective magnetization of sources along the edges from this study ranges from 2.5 to 11 A/m for a 40 km thick crust for most edges, but could be as high at 95 A/m in some of the southern highlands (see Table 4.2). See Table 2.1 (Milbury et al., 2012) for a list of magnetization/dipole parameters and paleopoles for authors including Frawley and Taylor (2004), Arkani-Hamed (2001b), Hood and Zakharian (2001), Hood and Richmond (2002), Hood et al. (2005), Arkani-Hamed (2004), Boutin and Arkani-Hamed (2006), Langlais and Purucker (2007), Hood et al. (2010), Quesnel et al. (2007), Hood et al. (2007). Additional magnetization/dipole parameters are provided in Table 5.1 for Milbury et al. (2012), Ravat (2011), Connerney et al. (1999) and Connerney et al. (2001).

Tables 5.2 to 5.6 show all the source locations, magnetization/dipole values and paleopoles that fall within a defined window region by author. For the edge of Segment 1 (Figure 4.3, region 285 to 360/0 to 50- following Milbury's convention of E°/N°), for a 50,000 nT inducing paleo-field and 40 km thick crust of uniform magnetization, the effective susceptibility (at the time of induction of the sources) is 0.1325 to 0.1764 SI

units and its equivalent magnetization is 5.2 to 7 A/m (Table 5.2). Arkani-Hamed (2001b; 2004) modeled 2 sources within the area and determined magnetizations of 10.8-15.32 A/m. The poles determined for this region vary greatly (Table 5.2). This is due in part to the complexity of the area (see discussion Chapter 4). For an area bound by the coordinates 341-344°E and 0- 4.7°N, the paleopoles determined by other authors range from 79-168°E in longitude and 70°N - 89.9°S in latitude. The pole determined in this study was 285°E, 15°S and reflects a much larger area range 285-360°E /0-50°N.

Table 5.3 shows the magnetization values for segment 2 (the north-south edge east of Tharsis, 285-315°E /40°S-20°N in Figure 4.10), ranged from 8.43 to 10.53 A/m. Arkani-Hamed modeled 2 sources that are located within window 2, one at 309°E /25°S that had a magnetization of 9.54 A/m which agrees well with the values determined in this study. The correlation coefficients for window 2 reflect a period of normal polarity. The best fit paleopole is 75°N, 300°E. This pole agrees well with the pole, 58.3°N, 318.9°E determined by Frawley and Taylor (2004). This window needs to be subdivided and re-modeled however, for the reasons discussed in Chapter 4.

Table 5.4 shows values of effective magnetization for segment 9 (the edge trending east/west located south of Tharsis, Figure 4.13) range 2.63 to 7.02 A/m. Values for other researchers range from 9 A/m to 29 A/m. The best fit poles determined for this area (45°N, 135°E; 15°N, 135°E) do agree reasonably well with poles determined by Arkani-Hamed (2001b) 10°N, 162°E, Boutin and Arkani-Hamed (2006) 5°N, 167°E and Hood et al. (2005) 27°N, 192°E , 43°N, 196°E within this region.

Table 5.5 shows the values of effective magnetization in the southern highlands over segment 11 (Figure 4.16) range from 42.13 to 94.79 A/m determined from E-W

profiles from N-S pseudo edges (these do not appear to be linear TG field features, but nonetheless high magnetization values would be necessary for these 200 and 500 nT amplitude features at 150 km altitude). Arkani-Hamed (2004) determined magnetization values of 42.16 A/m close to the Terra Sirenum and Terra Cimmeria regions (225/-45, just outside the window 11 range). Magnetization estimates from N-S profiles across the linear magnetic features in this region from Connerney et al. (1999) and Ravat (2011) are smaller than those determined in this study. Ravat (2011) modeled the linear features with multiple sources determining values of 10-55 A/m for the region 160-230°E/80°-75°S and values of 12.5-27.5 A/m for 160-215°E/57-50°S (just north of window 11). Connerney et al. (2001) determined a value of 60 A/m for a 200km diameter disc 3km thick was necessary to produce the anomaly for Terra Cimmeria at 400km altitude. While 42.13 A/m seems to be consistent with values determined by other researchers, 94.79 A/m is high. These values cannot be explained by production of magnetite through chemical reactions of serpentinization which is a process invoked to explain the high values of magnetization in the southern highlands (Quesnel et al., 2009) unless the inducing field was much stronger than modeled. More profiles in different locations should be done for segment 11 and the segment should be subdivided according to anomaly patterns.

Table 5.6 shows the effective magnetization value is 3.51 A/m in the region of segment 13 (the northeast edge of the Hellas Planitia, Figure 4.4). In susceptibility, this value is approximately 0.0662 SI units. Values from other authors range from 9 to 15 A/m for this region. In general, the methods in this study produce lower effective magnetization values than those found in other research, except in the area of the southern highlands. The best paleopoles for this region (15°S, 165°E; 45°S, 180°E) are

close to the pole determined by Milbury et al. (2012) for the Tyrrhenus Mons source (T10) once the pole is converted to the north areomagnetic paleopole (202°E, 67°S). There is still significant spread in the paleopoles for this region.

Window 13 poles (15°S, 165°E; 45°S, 180°E) likely represent early Noachian paleopoles during a period of reversal as indicated by the negative correlation coefficients (magnetic north pole located in geographic south). Window 11 has a best fit paleopole of 15°N, 195°E and likely represents a Noachian paleopole during a period of normal polarity indicated by positive correlation coefficients (magnetic north pole located in geographic north). Pole 11 is close in proximity to pole 13 (Figure 4.19). It is possible that pole 13 represents the early Noachian and sometime after the early Noachian the orientation of the dynamo reversed and this magnetic signal was recorded in the rocks formed during the middle and late Noachian in the region contained in window 11. The best fit paleopoles for window 1 are 15°S, 285°E; 0°, 292.5°E (during a period of reversed polarity) and likely represent an average of late Noachian to early Hesperian units although the area is complex geologically and there is significant spread in poles reported by all authors for this area. So it is possible the pole from window 11 reversed and "wandered" in the late Noachian to the pole location for window 1 (15°S, 285°E).

The results for windows 2 and 9 are questionable. The correlation coefficients for window 2 reflect a period of normal polarity. The best fit paleopole is 75°N, 300°E (Table 4.1) and likely represents a primarily Hesperian age range. This pole agrees well with the pole, 58.3°N, 318.9°E determined by Frawley and Taylor (2004) and does follow the trend to high latitude poles for Hesperian units reported by Milbury et al. (2012). The presently determined pole for the entire window 2, however, cannot be a true pole

because the region needs to be subdivided into multiple segments. For window 9, it is likely that the best paleopoles determined by correlation coefficients and visual analysis (45°N, 135°E; 15°N, 135°E) for this region represent an average of early Noachian to early Hesperian paleopoles based on the chronostratigraphic map versus anomaly locations. This pole is located close to the poles for window 13 (Figure 4.19). This region too, needs to be subdivided and re-modeled.

The methods outlined here have many benefits. If there are edge effects for a region, this method takes into account a much larger source area which can be modeled with fewer assumptions regarding the source shape, coalescence of the features or direction of magnetization. Segments 13, 11 (the southern and possible the eastern portion) and 1 are certainly edges and produce the most reliable paleopoles and effective magnetizations. The paleopoles for segment 2 do follow the trend to higher latitude poles for Hesperian sources recognized by Milbury et al. (2012) and the paleopole agrees well with Frawley and Taylor (2004), but, in retrospect, this region has differently oriented positive-negative anomaly lobes and needs to be subdivided into 3 sections and retested. Segment 9 needs to be subdivided as well to target the Noachian and Hesperian regions shown in Figure 4.14.

Table 5.1 Supplemental magnetization and pole locations by author. Paleopole locations and magnetization/dipole parameters to supplement Table 2.1.

Study	Source Location (°E/°N)	Magnetization/ Dipole	Paleopole Location (°E/°N)	Data/Method
Milbury et al. (2012) T1	106/-27.5	-1.5 x 10^{15} A m^2	284/45	Source identified from localized gravity and magnetics
T2	102/-30	-7.1x 10^{15} A m^2	222/4	
T3	100/-27	8.7 x 10^{15} A m^2	76/2	
T4	99.5/-20	-7.8 x 10^{15} A m^2	192/71	
T5	93.5/-19	-1.2 x 10^{16} A m^2	155/62	
T6	99.5/-11	-6.4 x 10^{15} A m^2	1/56	
T7	90/-10	-7.2 x 10^{15} A m^2	309/59	
T8	104.75/-10	6.4 x 10^{15} A m^2	190/24	
T9	110.5/-14.5	1.2 x 10^{16} A m^2	94/73	
T10	112/-18.5	-5.0 x 10^{15} A m^2	22/67	
T11	115/-15	1.0 x 10^{16} A m^2	65/47	
T12	118/-17.5	-5.5 x 10^{15} A m^2	59/53	
T13	119.5/-12.75	6.7 x 10^{15} A m^2	76/45	
S1	74/8.5	2.8 x 10^{15} A m^2	32/49	
S2	74.5/5.5	-3.2 x 10^{15} A m^2	204/87	
S3	70/-7.5	4.3 x 10^{15} A m^2	295/52	
S4	65.5/-7	1.4 x 10^{16} A m^2	211/75	
S5	58.5/-6	4.2 x 10^{15} A m^2	303/40	
S6	53/-5.5	1.0 x 10^{16} A m^2	293/44	
S7	43/-3	-6.9 x 10^{15} A m^2	122/28	
S8	49/-3	1.2 x 10^{16} A m^2	283/3	
S9	53/3	-9.0 x 10^{15} A m^2	247/84	
S10	59/9	-2.3 x 10^{15} A m^2	301/20	
S11	62.5/17	-2.8 x 10^{15} A m^2	356/59	
S12	57.25/19	-5.4 x 10^{15} A m^2	239/64	
S13	65/22.5	2.0 x 10^{15} A m^2	137/10	
S14	52.25/20	-1.6 x 10^{15} A m^2	265/44	
S15	52.5/23	6.7 x 10^{14} A m^2	332/19	
S16	56/24	-8.5 x 10^{15} A m^2	302/37	
Ravat (2011) L2	160 to 230/-75 to -80	10 – 55 A/m		Forward modeling of MGS long, linear anomalies at 150 km altitude
L1	160 to 215/-50 to -57	12.5 – 27.5 A/m		

Table 5.1. (continued)

Connerney et al. (1999)	196.1/-54.5	±20 A/m in Jx, Jz		Forward modeling of MGS observations below 200 km with seafloor spreading assumption
Connerney et al. (2001)	Terra Cimmeria	60 A/m		MGS at 400 km

Table 5.2. Window 1 Magnetization and Pole Comparison to Other Studies.

Study	Coordinates (°E-°E/°N-°N)	Magnetization/ Dipole	Pole (°E/°N)	Data/Method
This Study Window 1	285-360/0-50	7.02 A/m	285/-15	TG edge effect; test magnetization correlations between observed and computed fields; z-component at 150 km from the model of Langlais et al. (2010)
Richmond and Hood (2003) G	341/0	2.10 x 10^5 A	79/70	Low/high alt
Frawley and Taylor (2004) 8	343/4.7	1.46 x 10^{16} Am^2	163.4/-89.9	MGS 400 km data
Arkani-Hamed (2001b) M10	344/2	10.80 A/m	168/4	SH to degree 50; MGS 380 km alt
Arkani-Hamed (2004) 6	344/0	15.32 A/m	110/-24	Low/high alt

Table 5.3. Window 2 Magnetization and pole comparison to other studies

Study	Coordinates (°E-°E/°N-°N)	Magnetization/ Dipole	Pole (°E/°N)	Data/Method
This Study Whole window 2	Window 2 285 to 315/-40 to 20	8.43-10.53 A/m	300/75	TG edge effect; test magnetization correlations between observed and computed fields; z-component at 150 km from the model of Langlais et al. (2010)
This study Central sub-segment	305/-20		~215/~0	Estimated without modeling based on the pattern of positive-negative z-component
Frawley and Taylor (2004) 7	294.8/-37.2	3.50×10^{16} A m2	318.9/58.3	High alt
Arkani-Hamed (2004) 1	295/-33	28.73 A/m	182/8	Low/high alt
Hood et al. (2005) A3	297.5/-34.6	1.50×10^{16} A m^2	196/43	High alt
Frawley and Taylor (2004) 5	305.9/-4.8	2.21×10^{16}A m^2	99.3/82.6	High alt
Arkani-Hamed (2001b) M8	309/-25	9.54 A/m	162/10	SH to degree 50; MGS 380 km alt
Frawley and Taylor (2004)	311.2/-31.5	3.66×10^{16} Am^2	276.7/55.3	High alt

Table 5.4. Window 9 magnetization and pole comparison to other studies.

Study	Coordinates (°E-°E/°N-°N)	Magnetization/ Dipole	Pole (°E/°N)	Data/Method
This Study Window 9	240 to 315/-50 to -20	2.63 to 7.02 A/m	135/15	TG edge effect test magnetization correlations between observed and computed fields; z-component at 150 km from the model of Langlais et al. (2010)
Frawley and Taylor (2004) 1	252.3/-28.5	1.9 x 10^{16} Am^2	341.9/36.3	High alt
Arkani-Hamed (2004) 8	255/-27	17.65 A/m	351/17	Low/high alt
Boutin and Arkani-Hamed (2006) 8	255/-27		197/-3	High alt
Hood et al. (2005) A7a	254.2/-26.4	1.70 x 10^{16} Am^2	192/27	High alt
A7b	250/-22.1	8.00 x 10^{15} Am^2		High alt
Frawley and Taylor (2004) 7	294.8/-37.2	3.50 x $10^{16}Am^2$	318.9/58.3	High alt
Arkani-Hamed (2004) 9	295/-33	28.73 A/m	182/8	Low/high alt
Hood et al. (2005) A3	297.5/-34.6	1.5 x 10^{16} Am^2	196/43	High alt
Boutin and Arkani-Hamed (2006) 9	295/-33		174/4	High alt

Table 5.4. (continued)

Boutin and Arkani-Hamed (2006) 9	295/-33		167/5	High alt
Arkani-Hamed (2001b) M8	309/-25	9.54 A/m	162/10	SH to degree 50; MGS 380 km alt
Frawley and Taylor (2004) 6	311.2/-31.5	3.66 x $10^{16}Am^2$	99.3/82.6	High alt

Table 5.5. Window 11 magnetization and pole comparison to other studies.

Study	Coordinates (°E-°E/°N-°N)	Magnetization/ Dipole	Pole (°E/°N)	Data/Method
This Study Window 11	135 to 250/-90 to -60	42.13 to 94.79 A/m	195/15	TG edge effect test magnetization correlations between observed and computed fields; z-component at 150 km from the model of Langlais et al. (2010)
Ravat (2011) L2	160 to 230/-75 to -80	10 to 55 A/m	Within 20° of feature location	Forward modeling of MGS long, linear anomalies at 150 km
Ravat (2011) L1	160 to 215/-50 to -57	12.5 to 27.5 A/m	Within 20° feature location	Forward modeling of MGS long, linear anomalies at 150 km
Arkani-Hamed (2004) 7	225/-45	42.16 A/m	111/-42	Low/high alt

Table 5.5. (continued)

Connerney et al. (1999)	196.1/-54.5	±20 A/m	Close to the source	MGS observations below 200 km
Connerney et al. (2001)	Terra Cimmeria	60 A/m		MGS at 400 km
Quesnel et al. (2007)	Terra Sirenum	>30 A/m		Low/high alt

Table 5.6. Window 13 magnetization and pole comparison to other studies.

Study	Coordinates (°E-°E/°N-°N)	Magnetization/ Dipole	Pole (°E/°N)	Data/Method
This Study Window 13	75 to 120/-60 to -15	2.63 to 3.51 A/m	180/-45	TG edge effect test magnetization correlations between observed and computed fields; z-component at 150 km from the model of Langlais et al. (2010)
Arkani-Hamed (2001b) M6	103/-27	9.91 A/m	78/-7	SH to degree 50; MGS 380 km alt
Arkani-Hamed (2004) 3	105/-28	14.91A/m	60/20	Low/high alt
Boutin and Arkani-Hamed (2006) 3	105/-28		204/14 214/22	High alt
Milbury et al. (2012) T5	93.5/-19	-1.2×10^{16}	155/62	Source identified from localized gravity and magnetics
T4	99.5/-20	-7.8×10^{15}	192/71	
T3	100/-27	8.7×10^{15}	76/2	
T2	102/-30	-7.1×10^{15}	222/4	

T1	106/-27.5	-1.5 x 10^{15}	284/45	

Table 5.6. (continued)

T10	112/-18.5	-5.0 x 10^{15}	22/67	
T11	115/-15	1.0 x 10^{16}	65/47	
T12	118/-17.5	-5.5 x 10^{15}	59/53	

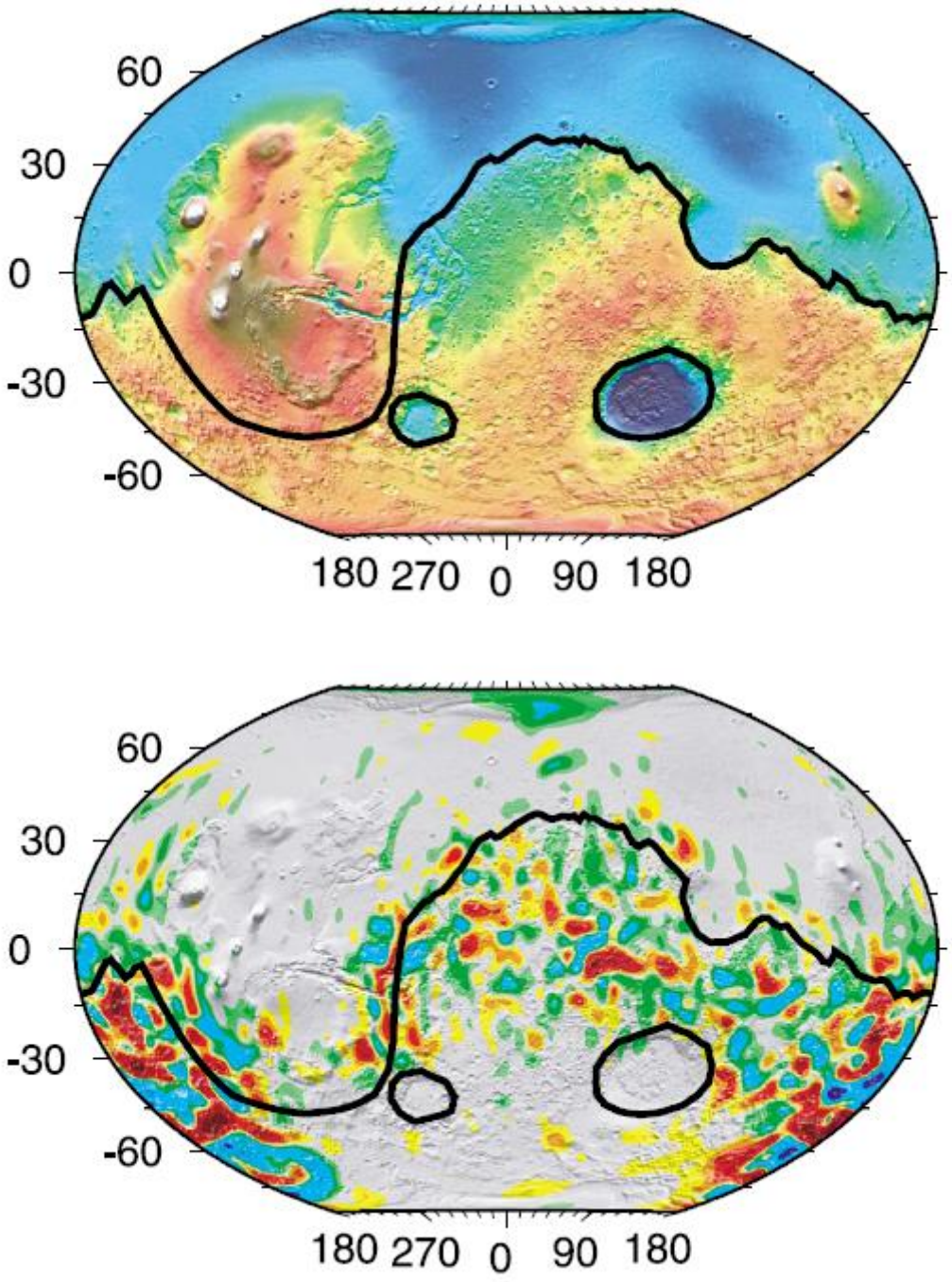

Figure 5.1. Dichotomy boundary (Milbury and Schubert, 2010). Dichotomy boundary used by Milbury and Schubert (2010). The top shows the boundary on topography and the bottom shows the boundary on the radial magnetic field of Langlais et al. (2004).

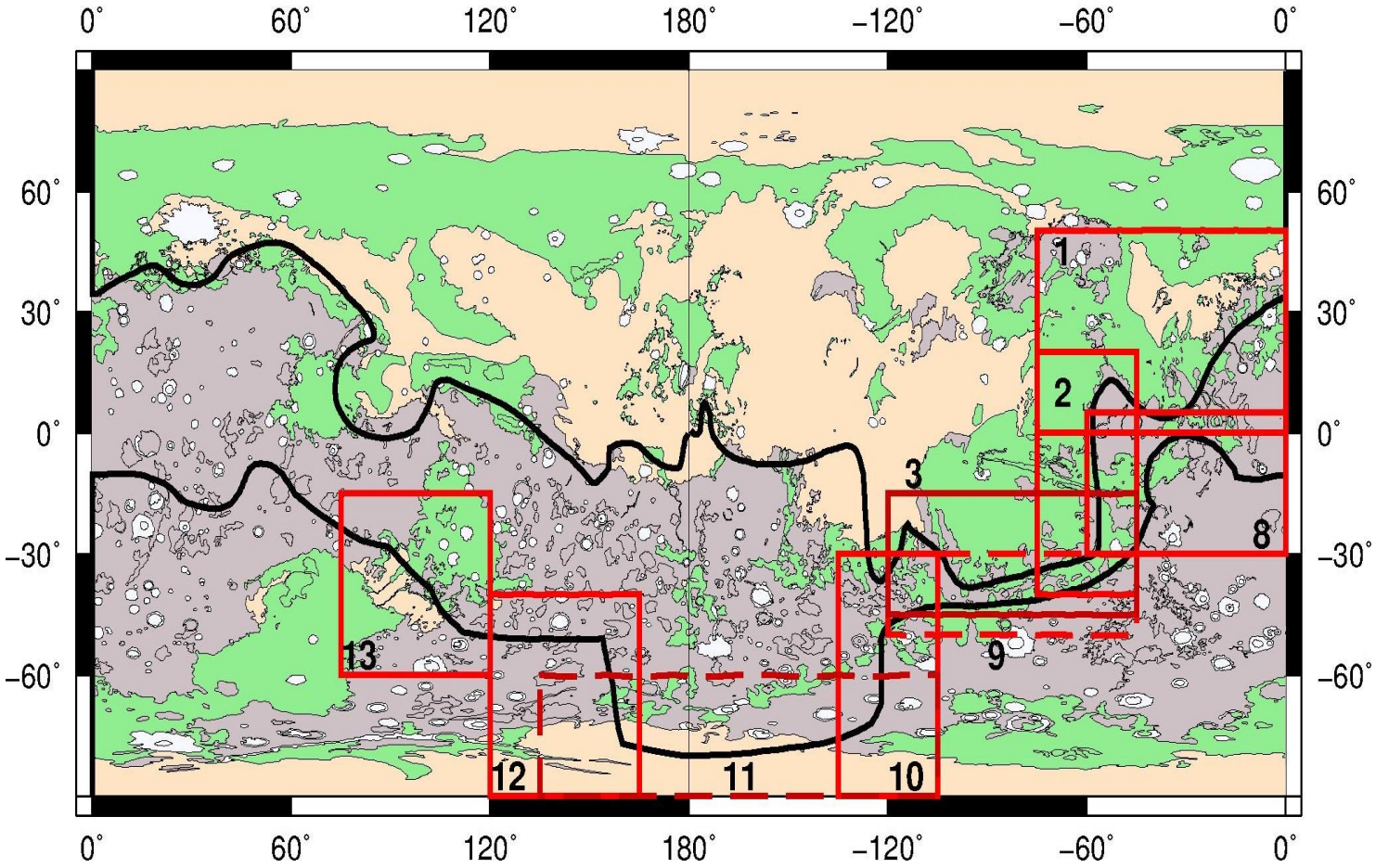

Figure 5.2. Map of chronostratigraphic units with windows and boundaries (after Skinner et al., 2006). Heavy black lines denote magnetization boundaries. Red boxes and adjacent black numbers are data windows.

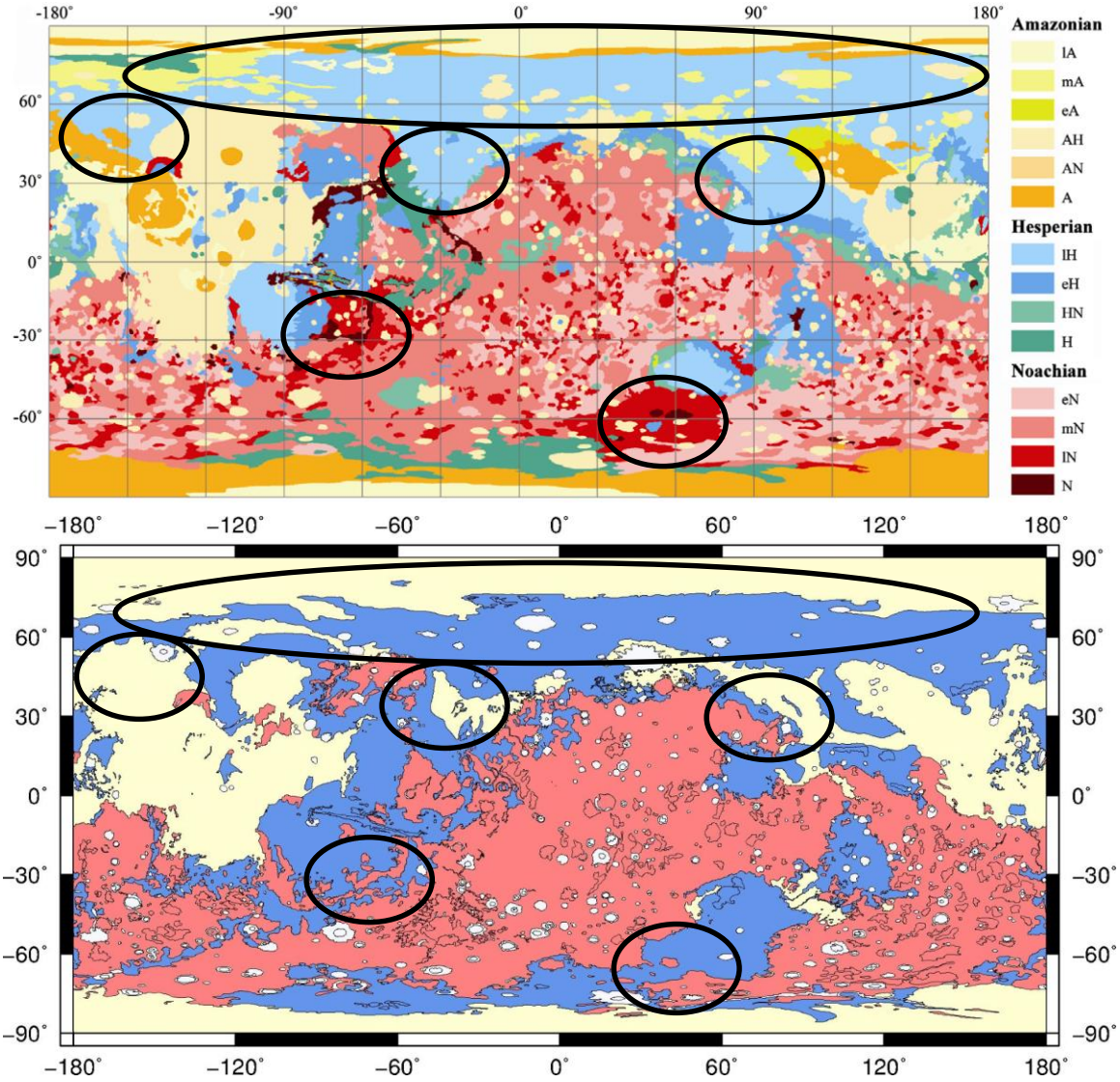

Figure 5.3. Comparison of 2014 map of Mars with 2006 map of Mars. The top is the chronostratigraphic map of Mars by Tanaka et al. (2014). The bottom map is the older map digitized by Skinner et al. (2006) based on Scott and Tanaka (1986) divided into age units. Ovals indicate significant areas of unit designation changes. Units in the upper map are designated by early (e), middle (m) and late (l), Amazonian (A), Hesperian (H) and Noachian (N). Of note are the large areas designated as multiple units (AH, AN) that were originally attributed to the Amazonian only. Also, some of the formations originally classified as Amazonian were changed to Hesperian and a few Hesperian units are now designated as Noachian. Color scheme for the bottom map was matched to the general color scheme of the top map.

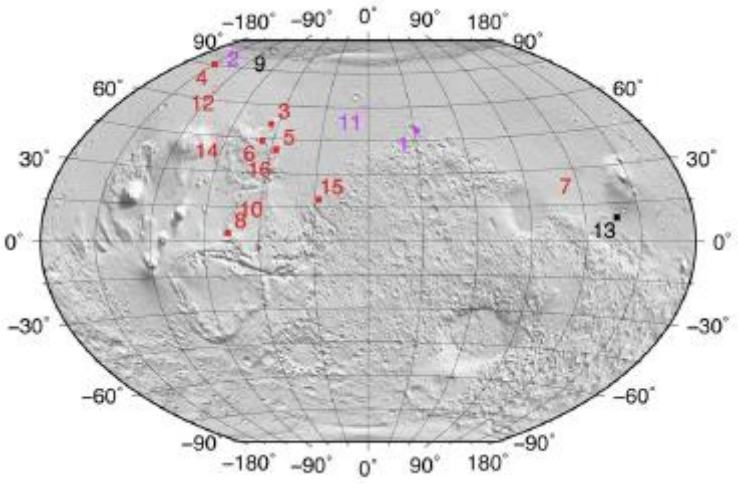

Figure 5.4. Best-fit paleopoles from magnetic anomalies near Syrtis Major (Milbury et al., 2012). Closed squares represent positive polarity and open squares negative polarity. Brown represents Noachian cratered features, purple represents Hesperian volcanic features and black represents cratered features by Greeley and Guest (1987).

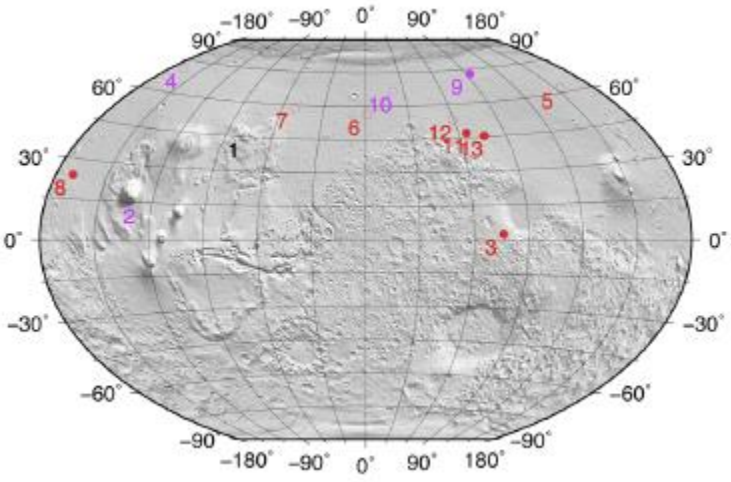

Figure 5.5. Best-fit paleopoles from magnetic anomalies near Tyrrhenus Mons (Milbury et al., 2012). Closed circles represent positive polarity and open circles negative polarity. Brown represents Noachian cratered features, purple represents Hesperian volcanic features and black represents cratered features by Greeley and Guest (1987).

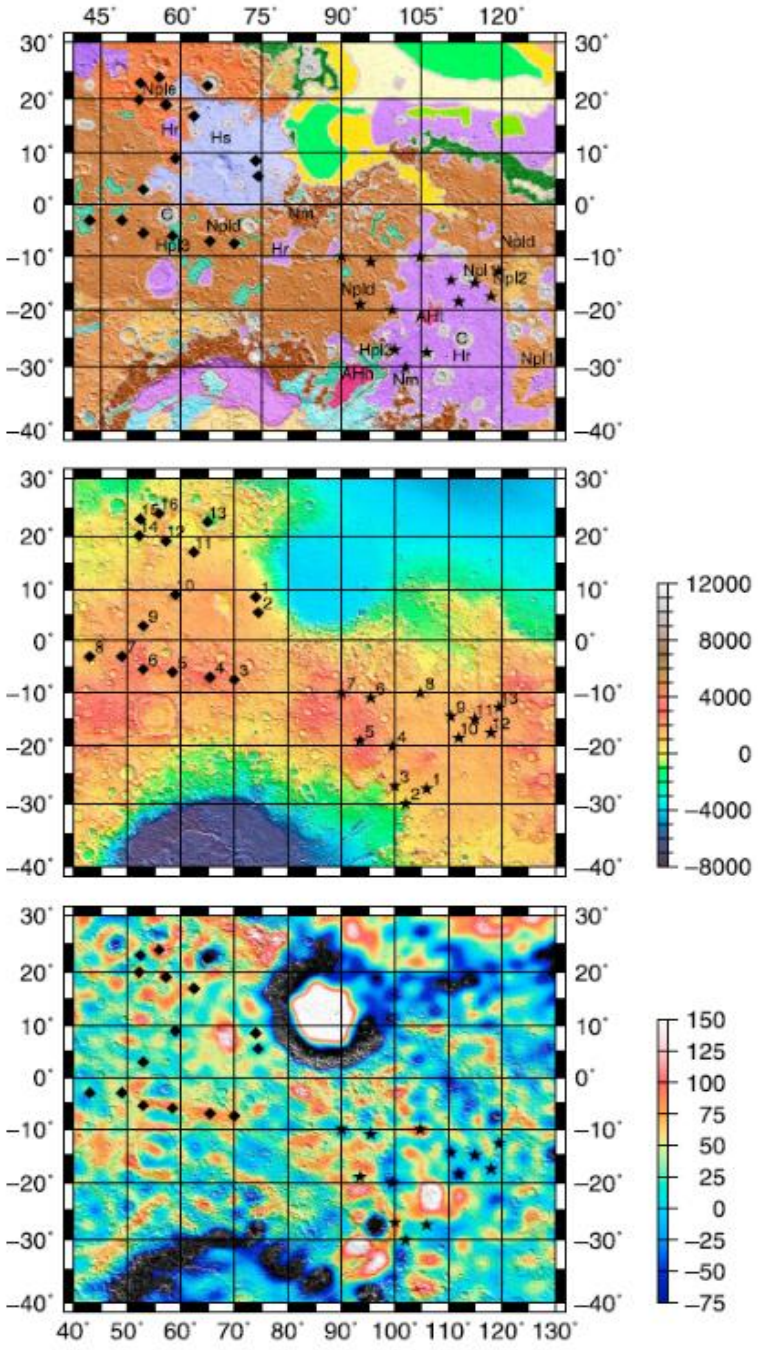

Figure 5.6. Map of magnetic anomalies on geology. Map of geology from Milbury et al. (2012) simplified from Greeley and Guest (1987), MOLA topography (Zuber et al., 2000), and free-air gravity (mGal) (Konopliv et al., 2011). Each map is superimposed of MOLA topography and the numbers represent magnetic sources modeled for Tyrrhenus Mons (stars) and Syrtis Major (diamonds).

Chapter 6. Conclusion and future work

This study determined paleopoles and magnetizations from a new method utilizing segments of magnetic source edges enclosing the central band of magnetic anomaly features on Mars. The methods outlined here have many benefits. If there are edge effects for a region, this method takes into account a larger source area which can be modeled with fewer assumptions regarding the source shape, coalescence of the features or direction of magnetization. Segments 1, 13 and 11 are certainly edges and produce the most reliable paleopoles (15°S, 285°E, 0°, 292.5°E; 15°S, 165°E, 45°S, 180°E; 15°N, 195°E) and effective magnetizations (7.02 A/m; 2.63-3.51A/m; 42.13-94.64A/m) although the upper end of magnetization for window 11 (94.64 A/m) is suspect. The paleopole for segment 2 (75°N, 300°E) does follow the trend to higher latitude poles for Hesperian sources recognized by Milbury et al. (2012) and agrees well with the value determined (58.3°N, 318.9°E) by Frawley and Taylor (2004). The effective magnetization of sources along the edges from this study ranges from 2.5 to 11 A/m for a 40 km thick crust for most edges, but could be as high at 95 A/m in some of the southern highlands (see Table 4.2). These values (Tables 5.1 to 5.6) agree reasonably well with values determined in other studies although the high (94.79 A/m) for the southern highlands (Window 11, Table 5.5) is suspect.

There are several ways in which this research could be updated and improved. In the computer program used to determine TG, the computations of theta and phi derivatives are performed by computing first the Fourier transforms of data on a latitude-longitude grid and then converting these derivatives into the spherical coordinate system. Recent tests have shown that the TG calculated from latitude and longitude location

changes equal to the distance used for obtaining numerical derivatives, yields more stable results from both the z-component and the total field components (personal communication, Ravat, 2015). Calculations of overlap should be re-done with the TG fields which are stable at the poles.

To improve the calculations of chronostratigraphic units showing magnetization, the process should be also be done with the newly published map of Mars (See Figure 5.3; Tanaka et al., 2014). This map is divided into units that cover single epochs or early, middle, and late Noachian (N), Hesperian (H), and Amazonian (A). In addition, the authors have added the units that cover multiple periods AN, HN and AH. This map constitutes a significant improvement in morphological and imaging information including Mars Global Surveyor (MGS) Mars Orbital Laser Altimeter, Mars Odyssey, Thermal Emission Imaging System, and Mars Reconnaissance Orbiter Context Camera data (Tanaka et al., 2014).

These additional data have resulted in much better resolution and work should be done to better target the boundary segment windows (size and location) based not only on TG and the dichotomy boundary, but also on chronostratigraphy from the new map (See Figure 5.3; Tanaka et al., 2014) to make sure the resulting paleopoles better reflect a specific age unit. In retrospect, the windows selected were not optimum for the analysis intended in the study. Figure 5.2 shows that data windows include within them multiple age terrains. For example, the Window 3 edge trending east/west, located south of Tharsis traverses Amazonian, Hesperian and Noachian age units and thus could yield an average paleopole that reflects all those ages. So it is impossible to attribute the resultant inducing pole orientations to a specific age range with certainty for some windows, but this

research does show that there have been multiple orientations of Mars inducing field through time including reversals of that field and may be able to reveal true (or better averaged paleopoles) with better targeted windows. In particular, the region of window 2 needs to be subdivided into 3 sections and remodeled. The north window should contain the Hesperian units, the center should contain Vallis Marineris, and the south should contain the Noachian units. Segment 9 also needs to be subdivided as well to target the Noachian and Hesperian regions shown in Figure 4.14. Then the highly correlated poles will be an average for a shorter time frame and smaller area.

Future calculations of overlap of the TG field and chronostratigraphic units should take into consideration the ambiguity in age of units AN, HN and AH. Efforts should be made to calculate overlap with TG fields multiple times including these areas in each epoch. This change will certainly add TG area to the Noachian and Hesperian since the regions (AN and AH) were originally designated only as Amazonian.

In the future, it would be ideal to conduct tests for statistical significance for the area of Hesperian terrain with TG anomalies to either strengthen or dismiss the case for a dynamo that was active in the early Hesperian. Each cell of overlap could be considered an observation and the TG value associated with each cell could be used to calculate mean and standard deviation based on total number of observations and number of observations for each unit (Hesperian, Amazonian, Noachian). The only other convincing way to demonstrate the dynamo was active in the Hesperian is to examine smaller Hesperian volcanoes or cratered units and TG fields associated with those features similar to Milbury et al. (2012) discussed in Chapter 4.

In addition, as an extension of this research, especially with low altitude magnetic

field data from Mars MAVEN satellite currently in orbit, depth to source techniques including Helbig and Euler analysis (Phillips et al., 2007) and 3D Spherical Coordinate Euler deconvolution (Ravat et al., 2002; Reid et al., 1990) should be assessed from individual anomalies. These anomalies could be targeted to a location where thickness of the upper units (Hesperian or Hesperian and Amazonian) can be constrained by topographical data (i.e., there is surface exposure through these units). This would aid in the understanding of the location of the source (in the stratigraphy) that is causing a weaker magnetic signal with Amazonian and Hesperian surface age terrains and ultimately clarify the results of the comparison of TG overlap with surface age. Gravity anomalies could also be used as an additional geophysical constraint for source characterization and location (Milbury et al., 2012). Milbury et al. (2012) used magnetic anomalies associated with gravity anomalies to help determine the lateral location of those magnetic anomalies. The gravity data could serve as a second check of the TG source location determination.

Appendix 1. ArcGIS Calculations

For comparisons of geology with magnetized regions, first all shapefiles of the geology database (Skinner et al., 2006) were re-projected into a Behrmann projection on the GCS_Mars_2000_Sphere coordinate system that contains the basic projection information on Mars including the radius of the planet. The Behrmann projection maintains area, and this was verified by comparing the ArcGIS calculated shape area with the USGS reported area (AreaSinKm2 value). The total calculated area by cell was 144,840,640.6 km^2 while the USGS reported area was 144,644,001.9 km^2. These values agree to within ~ 0.14%. The TG field rasters at several cutoffs levels at 0.5 degree latitude/longitude spacing were brought into ArcGIS and interpolated using kriging and converted into a shapefile (.shp). The shapefiles of the USGS chronostratigraphic map and the TG fields were then converted to a raster.

Raster calculator was used in ArcGIS to determine the area of overlap (in cells) of the 2 input rasters. The inputs rasters were TG (≥ 10, 15, 25, 50, 100, 200 nT/km) and the Noachian, Hesperian, Amazonian and "ageless" chronostratigraphic units. There are several units (mainly cratered units) that do not have age designations on the USGS map; their unit symbols are b, cb, cs, d, m, s, and v ("ageless units" below).

The total number of cells for the converted USGS chronostratigraphic map is 125,664. The cell count is based on the rows (544) and columns (231) or cell size at conversion (33.95km x 33.95km). This is an arbitrary value and any resolution could be used, as long as the same cell size is used for all overlap calculations. The area can be represented well as cells because it is rectangular and the system assigns optimal cell size to represent the whole map. Overlap/no overlap is designated by a logical variable with

values true (1) or false (0). The overlap of an age unit with the TG data, yields an output number of cells of overlap (represented by value 1 in Figure A1.1).

In addition to cells, there is data from the original USGS chronostratigraphic map that gives the area per polygon. ArcGIS statistics were used to sum all the area for the entire map and total surface area was 144,644,001.9 km^2.

To determine the area of overlap for the first Noachian criteria (TG ≥ 10 nT/km), The number of cells of overlap between the Noachian and TG maps (17628) was divided by the total number of cells (125664) x the total area of the cells (33.95km*33.95km*125664) = 20,318,076.87 km^2. For percent surface area, the calculation was 17628/125664 *100%. The raster was then converted back to a feature and the ArcGIS calculated area (shape_area) was used as a test. This area was 20,318,204.98 km^2. This agrees to within ~ 0.0063%.

Table A1.1 contains the overlap of chronostratigraphic units with TG cutoffs of 10, 15, 25, 50, 100 and 200 nT/km excluding the units Api and Apl. See chapter 3 for the discussion of the reason for the exclusion. Table A1.2 shows the overlap of TG cutoffs (10, 15, 25, 50, 100 and 200 nT/km) with chronostratigraphic units as a percentage of total planet surface area. These calculations include units Api and Apl with the Noachian (see discussion in Chapter 3).

Percent error between cell method and feature method is given by

$$\frac{Total\ Area\ by\ Features - Total\ Area\ by\ Cells}{Total\ Area\ by\ Features} \text{ or } \frac{144{,}940{,}699.4 - 144{,}840{,}640.6}{144{,}940{,}699{,}4} x\ 100\% = 0.07\%$$

The error is caused by approximating rounded edges with square cells. Figure A.1.3 shows the visual representation of this error. In places the area of overlap is overrepresented and in others it is underrepresented. There is no bias in this error.

Table A1.1. Overlap of chronostratigraphic units with TG cutoffs of 10, 15, 25, 50, 100, and 200 nT/km excluding the units Api and Apl.

TG >= 10 nT/km		
Units	Cells of overlap	Percentage
Noachian	17628	60.16%
Hesperian	7071	24.13%
Amazonian	3327	11.35%
Ageless Units	1278	4.36%
TOTAL	29304	100.00%

TG >= 15 nT/km		
Units	Cells of overlap	Percentage
Noachian	12032	63.77%
Hesperian	4131	21.89%
Amazonian	1729	9.16%
Ageless Units	977	5.18%
TOTAL	18869	100.00%

Table A1.1. continued

TG >= 25 nT/km		
Units	Cells of overlap	Percentage
Noachian	6064	66.71%
Hesperian	1889	20.78%
Amazonian	589	6.48%
Ageless Units	548	6.03%
TOTAL	9090	100.00%

TG >= 50 nT/km		
Units	Cells of overlap	Percentage
Noachian	2160	75.39%
Hesperian	545	19.02%
Amazonian	46	1.61%
Ageless Units	114	3.98%
TOTAL	2865	100.00%

Table A1.1. continued

TG >= 100 nT/km		
Units	Cells of overlap	Percentage
Noachian	488	83.42%
Hesperian	78	13.33%
Amazonian	1	0.17%
Ageless Units	18	3.08%
TOTAL	585	100.00%

TG >= 200 nT/km		
Units	Cells of overlap	Percentage
Noachian	15	93.75%
Hesperian	0	0.00%
Amazonian	0	0.00%
Ageless Units	1	6.25%
TOTAL	16	100.00%

Table A1.2. Overlap of TG cutoffs with chronostratigraphic units as a percentage of total planet surface area. The TG cutoffs (10, 15, 25, 50, 100 and 200 nT/km) were used to calculate area of overlap with chronostratigraphic units as a percentage of total planet surface area. Units Api and Apl are included in Noachian.

Noachian	Number of Cells of Overlap	Total Cells of USGS map	Calc. Area of Overlap from Cells (km2)	Percent of Planet Surface Area (%)
≥ 10 nT/km	19281	125664	22,226,866.31	15.35
≥ 15 nT/km	13367	125664	15,409,290.08	10.64
≥ 25 nT/km	6995	125664	8,063,737.87	5.57
≥ 50 nT/km	2747	125664	3,166,703.06	2.19
≥ 100 nT/km	821	125664	946,437.28	0.65
≥ 200 nT/km	65	125664	74,931.09	0.05

Hesperian	Number of Cells of Overlap	Total Cells of USGS map	Calc. Area of Overlap from Cells (km2)	Percent of Planet Surface Area (%)
≥ 10 nT/km	7071	125664	8,156,980.72	5.63
≥ 15 nT/km	4131	125664	4,765,448.64	3.29
≥ 25 nT/km	6995	125664	2,179,117.04	1.50
≥ 50 nT/km	545	125664	628,702.37	0.43
≥ 100 nT/km	78	125664	89,979.42	0.06
≥ 200 nT/km	0	125664	0.00	0.00

Table A1.2. continued

Amazonian	Number of Cells of Overlap	Total Cells of USGS map	Calc. Area of Overlap from Cells (km2)	Percent of Planet Surface Area (%)
≥ 10 nT/km	3327	125664	3,835,318.93	2.65
≥ 15 nT/km	1729	125664	1,993,166.94	1.38
≥ 25 nT/km	589	125664	678,990.94	0.47
≥ 50 nT/km	46	125664	53,028.15	0.04
≥ 100 nT/km	1	125664	1,152.79	0.001
≥ 200 nT/km	0	125664	0.00	0.00

Ageless Units	Number of Cells of Overlap	Total Cells of USGS map	Calc. Area of Overlap from Cells (km2)	Percent of Planet Surface Area (%)
≥ 10 nT/km	1278	125664	1,473,025.99	1.02%
≥ 15 nT/km	977	125664	1,126,092.64	0.77%
≥ 25 nT/km	548	125664	631,626.17	0.44%
≥ 50 nT/km	114	125664	131,396.69	0.09%
≥ 100 nT/km	18	125664	20,746.85	0.01%
≥ 200 nT/km	1	125664	1,152.60	0.00%

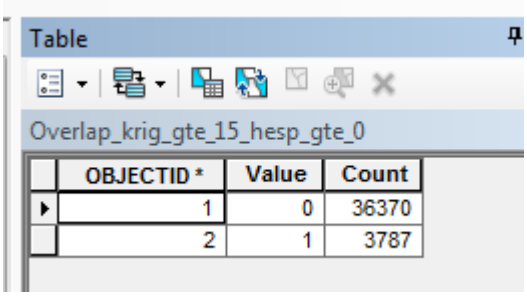

OBJECTID *	Value	Count
1	0	36370
2	1	3787

Figure A1.1. Output number of cells for overlap calculations.

Table

geo_units_oc_dd

FID	Shape *	UnitName	UnitSymb	AreaSinKm2
0	Polygon	polar ice deposits	Api	588743
1	Polygon	polar ice deposits	Api	133.117
2	Polygon	polar ice deposits	Api	451.702
3	Polygon	polar ice deposits	Api	4155.77
4	Polygon	polar ice deposits	Api	142.065
5	Polygon	polar ice deposits	Api	2208.05
6	Polygon	polar ice deposits	Api	221.449
7	Polygon	polar ice deposits	Api	1735.14
8	Polygon	polar ice deposits	Api	471.661

Figure A1.2. Polygon area calculations. The polygon area calculations in ArcGIS used to compare to area calculations based on cell size.

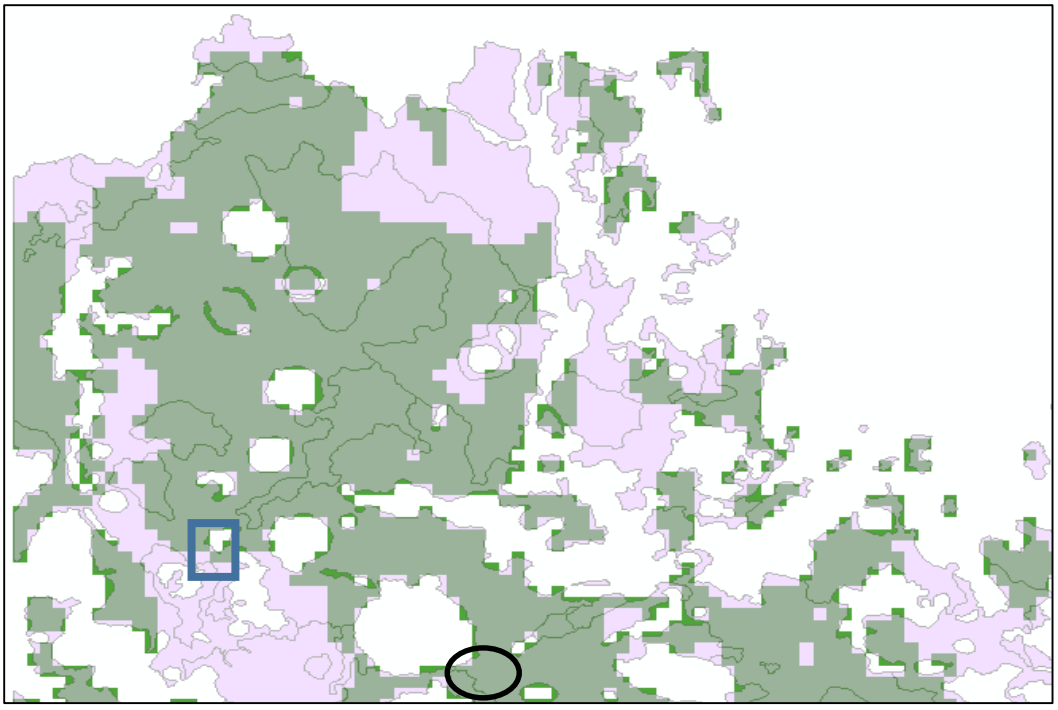

Figure A1.3. Error associated with calculating area by cells. Plot of Noachian terrain (in purple) underneath the area of overlap of the Noachian terrain with the TG greater than or equal to10 nT/km (in green). This figure shows the error associated with calculating area by cells. Both over estimations where the overlapped area exceeds that of the Noachian (see blue rectangle) and underestimations (see black oval) can are present.

Appendix 2. Boundaries tested.

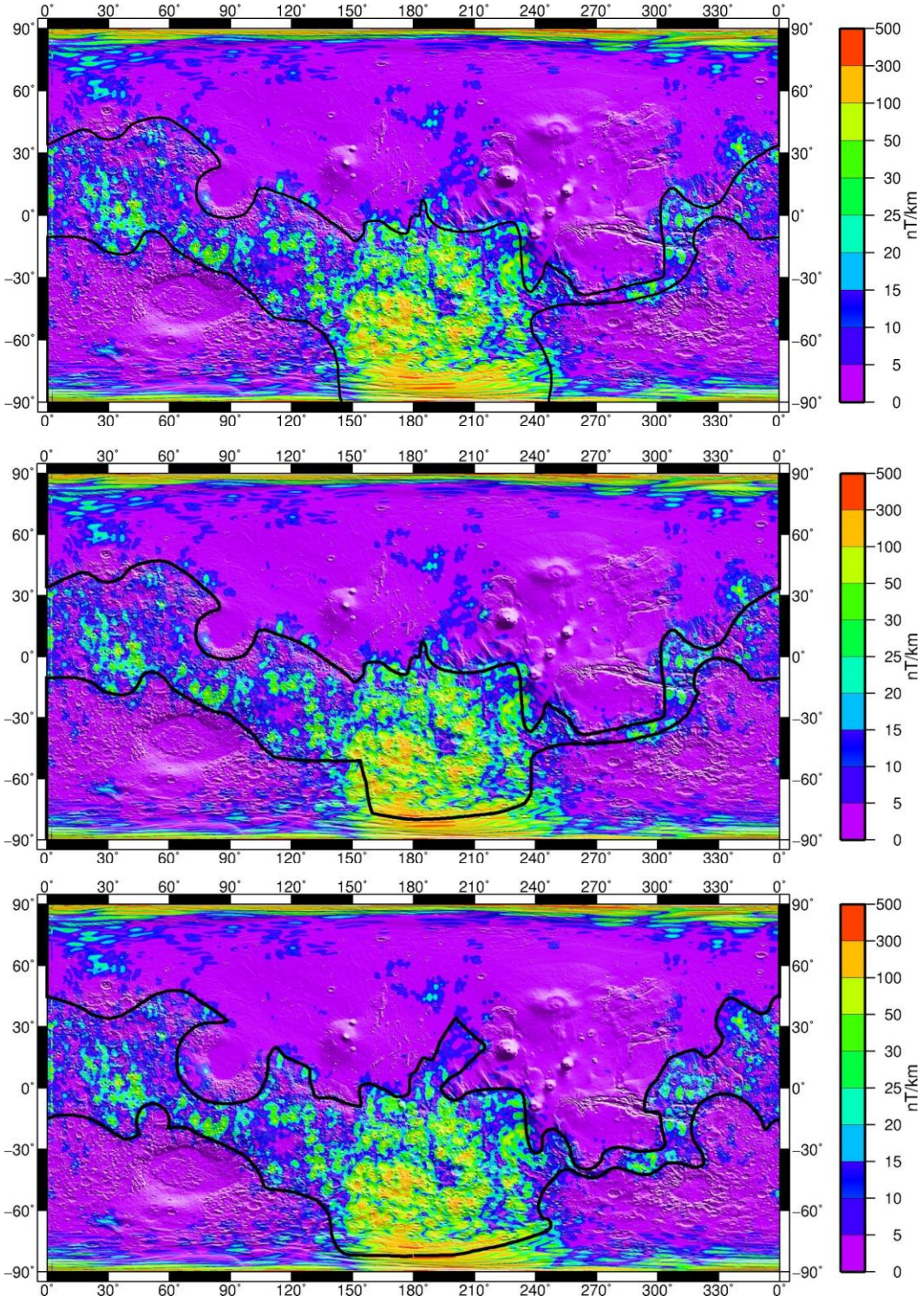

Figure A2.1. Additional test boundaries shown on TG Map (Equidistant cylindrical projection). The black lines represent three different sets of boundaries tested.

References

Acuña, M. H., Connerney, J.E.P., Ness, N.F., Lin, R.P., Mitchell, D., Carlson, C.W., McFadden, J., Anderson, K.A., Rème, H., Mazelle, C., Vignes, D., Wasilewski, P., and Cloutier, P., 1999. Global Distribution of Crustal Magnetization Discovered by the Mars Global Surveyor MAG/ER Experiment. Science 284, 790-793.

Acuña, M.H., Connerney, J.E.P., Wasilewski, P., Lin, R.P., Mitchell, D., Anderson, K.A., Carlson, C.W., McFadden, J., Reme, H., Mazelle, C., Vignes, D., Bauer, S.J., Cloutier, P.A., Ness, N.F., 2001. Magnetic field of Mars: Summary of results from the aerobraking and mapping orbits. *Journal of Geophysical Research* 106, 23, 403-423.

Arkani-Hamed, J., 2001a. A 50-degree spherical harmonic model of the magnetic field of Mars. *Journal of Geophysical Research* 106, 23, 197-208.

Arkani-Hamed, J., 2001b. Paleomagnetic pole positions and pole reversals of Mars. *Geophysical Research Letters* 28, 3409-3412.

Arkani-Hamed, J., Boutin, D., 2004. Paleomagnetic poles of Mars: Revisited. *Journal of Geophysical Research* 109, doi:10.1029/2003JE0029.

Arkani-Hamed, J. (2004), Timing of the Martian core dynamo, *Journal of Geophysical Research* 109, E03006.

Arkani-Hamed, J., 2005. Magnetic crust of Mars. *Journal of Geophysical Research* 110, doi:10.1029/2004JE002397.

Arkani-Hamed, J., 2009. Polar wander of Mars: Evidence from giant impact basins. *Icarus* 204, 489-498.

Arkani-Hamed, J., Olson, P., 2010. Giant Impacts, Core Stratification, and Failure of the Martian Dynamo. *Journal of Geophysical Research* 115, E07012.

Arkani-Hamed, J., Ghods, A., 2011. Could giant impacts cripple core dynamos of small terrestrial planets? *Icarus* 212, 920-934.

Arkani-Hamed, J., 2012. Life of the Martian dynamo. *Physics of the Earth and Planetary Interiors* 196-197, 83–96.

Barlow, N., 2008. *Mars: An Introduction to its Interior, Surface and Atmospshere.* Cambridge University Press, New York, USA.

Bevington, P., Robinson, D. K., 1991. *Data Reduction and Error Analysis for the Physical Sciences*. McGraw-Hill, New York, NY.

Biswas, S., 2005. Non-uniqueness of the modeled magnetization vectors used determining paleopoles on Mars. Department of Geology, M.S. Southern Illinois University Carbondale, 52p.

Blakely, R. J., 1995. *Potential Theory in Gravity and Magnetic Applications.* Cambridge University Press, New York, USA.

Bogard, D. D., Johnson, P., 1983. Martian gases in an Antarctic meteorite? *Science* 221, 651-654.

Boss, A. P., 1990. 3D solar nebula models: implications for Earth origin. In: *Origin of the Earth,* ed. H.E. Newsom and J.H. Jones. Oxford University Press, pp. 3-15

Boutin, D., Arkani-Hamed, J., 2006. Pole wandering of Mars: Evidence from paleomagnetic poles. *Icarus* 181, 13-25.

Chapman, M., 2007. *The Geology of Mars: Evidence from Earth-Based Analogs.* Cambridge University Press, New York, USA.

Connerney, J.E.P., Acuña, M.H., Wasilewski, P.J., Ness, N.F., Reme, H., Mazelle, C., Vignes, D., Lin, R.P., Mitchell, D., Cloutier, P.A., 1999. Magnetic lineations in the ancient crust of Mars. *Geophysical Research Letters* 28, 794-798.

Connerney, J.E.P., Acuña, M.H., Wasilewski, P., Kletetschka, G., Ness, N.F., Reme, H., Lin, R.P., Mitchell, D., 2001. The Global Magnetic Field of Mars and Implications for Crustal Evolution, *Geophysical Research Letters* 28, 4015-4018.

Connerney, J.E.P., Acuna, M.H., Ness, N.F., Spohn, T., Schubert, G., 2004. Mars crustal magnetism. *Space Science Reviews* 111, 1-32.

Craddock, R.A., Greeley, R., 2009. Minimum estimates of the amount and timing of gases released into the martian atmosphere from volcanic eruptions. *Icarus* 204, 512–526.

Ditty, M.L., Ravat, D., 2014. Mars paleopole and magnetization estimates from magnetization edge effects. *45th Lunar and Planetary Science Conference,* Abstract #2075.

Elkins-Tanton, L.T., Hess, P.C., and Parmentier, E.M., 2005. Possible formation of ancient crust on Mars through magma ocean processes. *Journal of Geophysical Research* 110, E12S01.

Esposito, P., Alwar, V., Burkhart, S., Demcak, S., Graat, E., Johnston, M., Portock, B., (1997). Navigating Mars Global surveyor through the martian atmosphere: aerobraking 2. *AAS/AIAA Flight Mechanics Conference*, Austin, TX , AAS 98-112.

Fairen, A.G., Ruiz, J., Anguita, F., 2002. An origin for the linear magnetic anomalies on Mars through accretion of terranes: Implications for dynamo timing. *Icarus* 160, 220-223.

Frawley, J.J., Taylor, P.T., 2004. Paleo-pole positions from Martian magnetic anomaly data. *Icarus* 172, 316-327.

Frey, H.V., 2006. Impact constraints on the age and origin of the lowlands of Mars. *Geophysical Research Letters* 33, L08S02.

Glatzmeier, G.A., Roberts, P.H., 1997. Stimulating the Geodynamo, *Contemporary Physics* 38, 269-288.

Greely, R., Guest, J.E., 1987. Geologic map of the eastern equatorial region of U.S. Geo. Surv. Misc. Invest. Ser., MarsIMAP 1802-B.

Halliday, A.N., Wanke, H., Birck, J.L., Clayton, R.N., 2001. The accretion, composition, and early differentiation of Mars. *Space and Science Reviews*, 96, 197-230.

Hartmann, W. K., Neukum, G. (2001). Cratering chronology and the evolution of Mars. *Space Science Reviews*, 96, 165-194.

Hviid, S.F., Madsen, M.B., Gunnlaugsson, H.P., Goetz, W., Knudsen, J.M., Hargraves, R.B., Smith, P., Britt, D., Dinesen, A.R., Mogensen, C.T., Olsen, M., Pedersen, C.T., Vistisen, L., 1997. Magnetic properties experiments on the Mars Pathfinder lander: Preliminary results, *Science*, 278, 1768-1770.

Hood, L.L., Zakharian, A. 2001. Mapping and modeling of magnetic anomalies in the northern polar region of Mars. *Journal of Geophysical Research* 106, 14601-14619.

Hood, L.L., Richmond, N.C., 2002. Mapping and modeling of major Martian magnetic anomalies, *Proc. Lunar Planet. Sci. Conf. 33rd*, abstract 1128.

Hood, L.L., Richmond, N.C., Pierazzo, E., and Rochette, P., 2003. Distribution of crustal magnetic fields on Mars: shock effects of basin-forming impacts. *Geophysical Research Letters* 30, 1281, doi:10.1029/2002GL016657.

Hood, L.L., Young, C.N., Richmond, N.C., Harrison, K.P., 2005. Modeling of major Martian magnetic anomalies: Further evidence for polar reorientations during the Noachian. *Icarus* 177, 144-0173.

Hood, L.L., Harrison, K.P., Langlais, B., Lillis, R.J., Poulet, F., Williams, D.A., 2010. Magnetic anomalies near Apollinaris Patera and the Medusae Fossae Formation in

Lucus Planum, Mars. *Icarus* 208, 118-131.

Hood, L.L., Richmond, N.C., Pierazzo, E., Rochette, P., 2003. Distribution of crustal magnetic fields on Mars: Shock effects of basin-forming impact. *Geophysical Research Letters* 30, 1281.

Ivanov, B.A., 2001. Mars/moon cratering rate ratio estimates. *Space Science Review* 96, 87–104.

Johnson, C.L., Phillips, R.J., 2005. Evolution of the Tharsis region of Mars: insights from magnetic field observations. *Earth & Planetary Science Letters* 230, 241-254.

Katanforoush, A., Shahshahani, M., 2001. Distributing points on the sphere. *Experimental Mathematics* 12, 199-209.

Kleine, T., Munker, C., Mezger, K., and Palme, H., 2002. Rapid accretion and early core formation on asteroids and the terrestrial planets from Hf-W chronometry. *Nature* 418, 952-955.

Konopliv A.S., Asmar, S.W., Folkner, W.M., Karatekin, O., Nunes, D.C., Smrekar, S. E., Yoder, C.F., Zuber, M.T., 2011. Mars high resolution gravity fields from MRO, Mars seasonal gravity, and other dynamical parameters. *Icarus* 211, 401-428.

Langlais, B., Purucker, M. E., Mandea, M., 2004. Crustal magnetic field of Mars. *Journal of Geophysical Research* 109, E02008, doi:10.1029/2003JE002048.

Langlais, B., Purucker, M., 2007. A polar magnetic paleopole associated with Apollinaris Patera, *Mars Planetary Space Science* 55, 270–279.

Langlais, B., Purucker, M.E., Lillis, R.J., 2010. A new and improved description of the Martian magnetic crustal field using both MGS-MAG and MGS-ER measurements, *American Geophysical Union, Fall Meeting 2010*, Abstract #GP42A-02.

Langel, R.A., Hinze, W.J., 1998. *The Magnetic Field of the Earth's Lithosphere: The Satellite Perspective*. Cambridge University Press.

Merrill, R.T. and McKinney, M.W., 1983. *The Earth's Magnetic Field*. Academic Press, San Diego, CA.

Milbury, C., Schubert, G., Raymond, C.A., Smrekear, S.E., Langlais, B., 2012. The history of Mars' dynamo as revealed by modeling magnetic anomalies near Tyrrhenus Mons and Syrtis Major. *Journal of Geophysical Research* 117, E10007.

Milbury, C., Schubert, G., 2010. Search for the global signature of the martian dynamo. *Journal of Geophysical Research* 115, E10010. doi:10.1029/2010JE003617.

Miller, J., Ravat, D., Taylor, P.T., Frey, H., Zatman, S., Frawley, J.J., 2001. Interpretation of the Martian Southern Highland Magnetic Anomalies using the Euler and Analytic Signal Methods. *Eos Trans. AGU, 82(20), Spring Meet. Suppl.*, S123.

Mohit, P. S., Arkani-Hamed, J., 2004. Impact demagnetization of the martian crust. *Icarus* 168, 305-317.

Morschhauser, A., Lesur, V., Grott, M., 2014. A spherical harmonic model of the lithospheric magnetic field of Mars, *Journal of Geophysical Research* 119, 1162–1188.

Mutch, T., Arvidson, R., Head III, J., Jones, K., Saunders, R., 1976. *The Geology of Mars.* Princeton University Press, Princeton, N.J.

Nabighian, M.N., 1972. The analytic signal of two-dimensional magnetic bodies with polygonal cross-section: its properties and use for automated anomaly interpretation. *Geophysics* 37(3), 507–517.

Nabighian, M.N.,1974. Additional comments on the analytic signal of two dimensional magnetic bodies with polygonal cross-section. *Geophysics* 39(1), 85–92.

Nabighian, M.N., 1984. Toward a three-dimensional automatic interpretation of potential field data via generalized Hilbert transforms: Fundamental relations, *Geophysics* 49(6), 780–786.

Nimmo, F., 2000. Dike intrusion as a possible cause of linear martian magnetic anomalies. *Geology* 28, 391-394.

Nimmo, F., Stevenson, D., 2000. Influence of early plate tectonics on the thermal evolution and magnetic field of Mars'. *Journal of Geophysical Research* 105, 11969-11979.

Neukum, G., Ivanov, B.A., Hartmann, W.K., 2001. Cratering records in the inner solar system in relation to the lunar reference system. *Space Science Review* 96, 55–86.

Nyquist, L.E., D.D. Bogard, C.Y. Greshake, D. Stoffler, Eugster, O., 2001. Ages and geological history of Martian meteorites, *Space Science Review* 96, 105–164.

Phillips, J.D., Nabighian, M.N, Smith, D.V., Li, Y., 2007. Estimating locations and total magnetization vectors of compact magnetic sources from scalar, vector or tensor magnetic measurements through combined Helbig and Euler analysis. *SEG annual meeting*, San Antonio, TX, SEG 770-774.

Plattner, A., Simons, F.J., 2014. Spatiospectral concentration of vector fields on a sphere. *Applied Computational Harmonic Analysis* 36, 1-22.

doi:10.1016/j.acha.2012.12.001

Purucker, M., Ravat, D., Frey, H., Voorhies, C., Sabaka, T., Acuña, M., 2000. An altitude-normalized magnetic map of Mars and its interpretation. *Geophysical Research Letters* 27, 2449-1452.

Quesnel, Y., Langlais, B., Sotin, C., 2007. Local inversion of magnetic anomalies: implications for Mars' crustal evolution. *Planetary and Space Science* 55, 258-269.

Quesnel, Y., Sotin, C., Langlais, B., Costin, S., Mandea, M., Gottchaulk, M., Dyment, J., 2009. Serpentinization of the martian crust during the Noachian. *Earth and Planetary Letters* 277, 184-193.

Ravat, D., Wang, B., Wildermuth, E., Taylor, P. T., 2002. Gradients in the interpretation of satellite-altitude magnetic data: an example from central Africa. *Journal of Geodynamics* 33, 131-142.

Ravat, D., 2003. Can we infer tectonics correctly from satellite altitude magnetic anomalies? Examples from Earth and Mars. *Geophysical Research Abstracts*, European Geophysical Society, vol. 5, Abstract EAE-03-A-04089.

Ravat, D., 2011. Interpretation of Mars southern highlands high amplitude magnetic field with total gradient and fractal source modeling: New insights into the magnetic mystery of Mars. *Icarus* 214, 400-412.

Reid, A. B., Allsop, J. M., Granser, H., Millett, A. J., Sommerton, I. W., 1990. Magnetic interpretation in three dimensions using Euler deconvolution. *Geophysics* 55, 80-91.

Roest, W.R., Verhoef, J., Pilkington, M., 1992. Magnetic interpretation using the 3-D analytic signal, *Geophysics* 57(1), 116–125.

Schubert, G., Russell, C.T., Moore, W.B., 2000. Timing of the Martian dynamo. *Nature* 408, 666-667.

Scott, D. H., Tanaka, K. L., 1986. Geologic map of the western equatorial region of Mars. USGS Map I-1802-A.

Skinner, J.A. Jr., Hare, T.M., Tanaka, K.L., 2006. Digital Renovation of the Atlas of Mars 1:15,000,000-Scale Global Geologic Series Maps. *37th Lunar Planetary Science Conference,* Abstract #2331.

Sprenke, K.F., Baker, L.L., 2000. Magnetization, paleomagnetic poles and polar wander on Mars. *Icarus* 147, 26-34.

Sprenke, K.F., Baker, L.L., Williams, A.F., 2005. Polar wander on Mars: Evidence in the geoid. *Icarus* 174, 486-489.

Spohn, T., Breuer, D., Johnson, T.V., 2014. *Solar System Encyclopedias*. Elsevier, Inc. Oxford, UK.

Tanaka, K.L., Robbins, S.J., Fortezzo, C.M., Skinner, Jr., J.A., Hare, T.M., 2014. The digital global geologic map of Mars: Chronostratigraphic ages, topographic and crater morphologic characteristics, and updated resurfacing history. *Planetary and Space Science* 95, 11-24.

Taylor, J.R., 1996. *An Introduction to Error Analysis: The Study of Uncertainties in Physical Measurements*. University Science Books, Sausaltio, CA.

Wetherill, G.W., 1990. Formation of the Earth. *Annual Reviews of Earth and Planetary Science* 18, 205-256.

Wetherill, G.W., 1994. Provenance of the terrestrial planets. *Geochim Cosmochim Acta*, 58(20), 4513-20.

Williams, J.P., and Nimmo, F., 2004. Thermal evolution of the martian core: implications for an early dynamo. *Geology* 32, 97-100

Zuber, M.T., 2000, Solomon, S.C., Phillips, R.J., Smith, D.E., Tyler, G.L., Aharonson, O., Balmino, G., Barnerdt, W.B., Head, J.W., Johnson, C.L., Lemoine, F.G., McGovern, P.J., Neumann, G.A., Rowland, D.D., Zhong, S., 2000. Internal structure and early thermal evolution of Mars from Mars Global Surveyor topography and gravity. *Science* 287, 1788-1793.

VITA

Melissa Lynn Ditty
Paducah, KY

Educational Institutions:
University of Kentucky: Lexington, KY: B.S., Geology; 2010.

Professional Positions:
Intern: EQT, Pittsburgh, PA: Summer 2012
Graduate Research and Teaching Assistant: University of Kentucky, Lexington, KY; August 2012- Dec 2013

Professional Publications:
Ditty, M.L., Ravat, D., 2014. Mars paleopole and magnetization estimates from magnetization edge effects. 45th Lunar and Planetary Science Conference, Abstract #2075.

Scholastic and Professional Honors:
University of Kentucky Fellowship for Selected Areas
Brown-McFarlan Grant
Pirtle Fellowship
Outstanding Teaching Assistant Award